Master thesis and internship[BR]- Master's thesis : Derivative-less control-based nonlinear vibration testing[BR]- Internship

Auteur : Spits, Alexandre
Promoteur(s) : Kerschen, Gaëtan
Faculté : Faculté des Sciences appliquées
Diplôme : Master en ingénieur civil en aérospatiale, à finalité spécialisée en "aerospace engineering"
Année académique : 2023-2024
URI/URL : http://hdl.handle.net/2268.2/20064

University of Liège - Faculty of Applied Sciences

Derivative-less control-based nonlinear vibration testing

Master's Thesis for the degree of Master of Science in Aerospace Engineering

Author: Alexandre SPITS

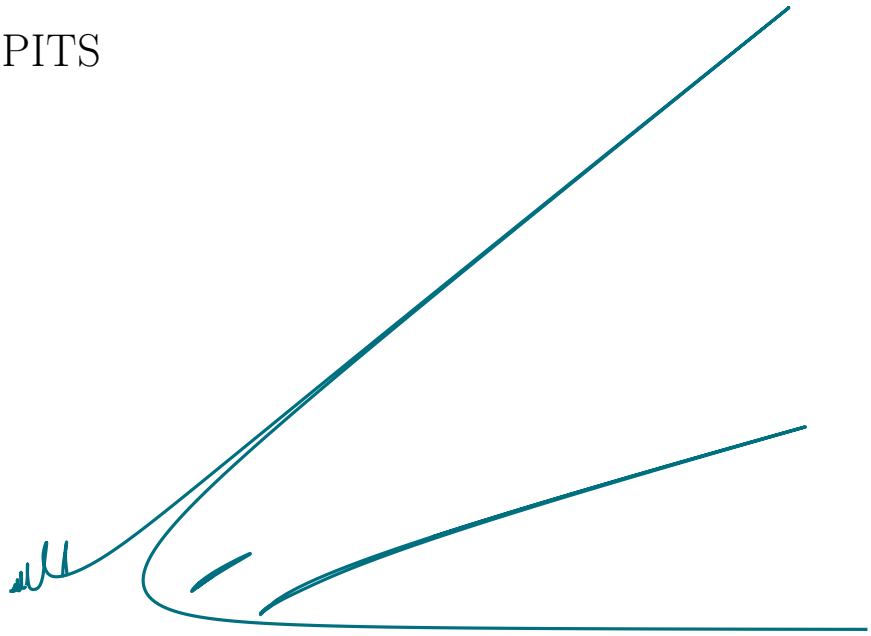

Student ID: S190981
Advisor: Prof. Gaëtan KERSCHEN
Academic Year: 2023-2024

Jury

by alphabetical order

President

Prof. Grigorios DIMITRIADIS

University of Liège

Supervisor

Prof. Gaëtan KERSCHEN

University of Liège

Members

Prof. Olivier BRULS

University of Liège

Dr. Ghislain RAZE

University of Liège

Abstract

Characterizing the vibrational response of structures is essential for ensuring safety and integrity under dynamic loads, or "excitations". Linear systems resonate only at their natural frequencies, known as fundamental resonances, and obey the principle of superposition. Real-world structures exhibit nonlinear behavior and the same excitation frequency can lead to multiple stable or unstable solutions, with possible jumps between solutions. In addition to their fundamental resonance, nonlinear systems can resonate at any multiple or fraction of the excitation frequency, a phenomenon known as superharmonic or subharmonic resonance.

Experimental modal analysis, based on linear assumptions, fails to characterize nonlinear responses. New approaches have been developed for more systematic and reliable testing of nonlinear structures. This thesis investigates a recently introduced derivative-free method for experimental arclength control-based continuation (ACBC). The study focuses on a one-degree-of-freedom system with cubic nonlinearity, known as the Duffing oscillator. Both a numerical Duffing oscillator and an experimental setup involving an electronic circuit simulating the Duffing oscillator's behavior are considered.

The ACBC method is applied to identify the frequency response of both numerical and electronic Duffing oscillators. While their fundamental resonance is fully identified, superharmonic and subharmonic resonances remain challenging to identify completely. To address these limitations, e new double-sweep strategy is introduced into the existing ACBC method. This approach successfully identifies superharmonic and subharmonic resonances, including isolated responses. Furthermore, the double-sweep strategy effectively detects isolated responses experimentally. It opens the door to advancing the study of secondary resonances, enhancing the design of mechanical structures to avoid unexpected failures and ensure long-term reliability.

Keywords: Nonlinear dynamics, Control-based continuation, Superharmonic resonance, Subharmonic resonance, Derivative-free method

Acknowledgements

First of all, I am extremely grateful to my academic supervisor, Prof. Gaëtan Kerschen, for sharing his invaluable expertise with me. His constant availability and support have played a fundamental role in my progress through every step of this work. Through our meetings, he have always steered me in the right direction while providing constructive suggestions to keep improving this manuscript.

I would like to warmly thank Ghislain Raze, for taking so much of his time to share his knowledge of control-based continuation and nonlinear dynamics with me. He was able to answer all my questions and, thanks to him, I always felt welcome and supported at the office.

I would like to take this opportunity to recognize the contribution of all the professors and teachers met along the way.

Enfin, je remercie ma famille et mes amis pour leur amour et leur soutien, et pour l'inspiration qu'ils ont été tout au long de ma vie. En particulier, je dois exprimer ma profonde gratitude à mes parents pour leurs encouragements constants au fil des ans. Je ne les remercierai jamais assez pour leur incroyable soutien.

Contents

List of symbols

Variable	Description
c	Damping coefficient
$c_{x,n}$	Cosine Fourier coefficient of the response's n-th harmonic
e	Synthesis error of adaptive filters / Control error
f	Mass-normalized force amplitude
k	Stiffness coefficient
k_3	Cubic stiffness coefficient
k_d	Differential controller gain
k_i	Integral controller gain
k_p	Proportional gain
$k_{i,\mathrm{nf}}$	Integral gain for double sweep
K	Proportional gain
l	Harmonic number / Superharmonic index
m	Mass coefficient
n	Harmonic number
N	Total number of harmonics considered
p	Amplitude of fundamental excitation
p^*	Targeted amplitude of fundamental excitation
$\mathbf{Q}$	Basis of harmonic signals
$s_{x,n}$	Sine Fourier coefficient of the response's n-th harmonic
t	Time
t_s	Sampling time
T_d	Derivative time
T_i	Integral time
u	Outpout of the controller
$\mathbf{w}$	Weight coefficients
x	Response (displacement) of the nonlinear oscillator
x_0, $\dot{x}_0$	Initial displacement and velocity
x_f	Fundamental component of response
x_nf	Non-fundamental component of response
x_p	Particular solution

Variable	Description
x^*	Reference signal
x^*_{f}	Fundamental component of reference signal
x^*_{nf}	Non-fundamental component of reference signal
X_n	Amplitude of the response's n-th harmonic
X^*_n	Amplitude of the reference's n-th harmonic
y	Process variable
y_{sp}	Setpoint value
$\mathbf{z}$	Fourier coefficients
α	Sweep angle
α_0	Starting sweep angle
α_3	Mass-normalized cubic stiffness coefficient
β	FRC slope angle
γ	Exponent of the cosine distance
δ	Hyper angle
ζ	Modal damping ratio
μ	Step size factor of adaptive filters
ν	Harmonic number / Subharmonic index
σ	Dimensionless displacement
τ	Dimensionless time
ω	Frequency
ω_0	Linear natural frequency
ω_l	Frequency of the l-th harmonic
Ω	Nonlinear motion frequency

1 Introduction

The vibrational analysis of mechanical systems is crucial for both predicting the behavior of a future system and experimentally characterizing an existing structure to understand its response under different conditions. Engineers create mathematical models to anticipate system responses to various excitations, and then perform experimental characterization to validate these models [23].

For a predominantly linear structure, the response to a sum of excitation signals equals the sum of the responses to each individual signal, illustrating the superposition principle. This principle has two main consequences. First, the response to a multi-harmonic excitation can be broken down into responses to each frequency component. Second, the frequency response at any forcing amplitude can be determined from a previously computed frequency response at an arbitrary forcing. The frequency response function can be identified either by testing each frequency individually (stepped or swept sine testing) or by testing all frequencies simultaneously (broadband testing) [27, 59]. This approach, known as experimental modal analysis (EMA), allows for predicting responses to any periodic excitation. EMA is the primary method for assessing structural dynamics, supported by mature software like Simcenter Testlab (Siemens) and BK Connect (Brüel and Kjaer).

Real-world structures exhibit nonlinear behavior from various sources. Common nonlinearities include geometric and inertia nonlinearity, nonlinear material behavior (foams, rubber isolators), and nonlinear damping (dry friction, hysteretic damping). Additionally, boundary conditions (free surfaces in fluids, vibro-impacts from loose joints or contacts with rigid constraints, clearances, imperfectly bonded elastic bodies) and external body forces (e.g., magnetoelastic, electrodynamic or hydrodynamic forces) can introduce nonlinearity [39].

Nonlinearity poses challenges to the EMA testing philosophy. Figure 1.1 shows the harmonically forced response of a Duffing oscillator, a one-degree-of-freedom system with cubic nonlinearity. The figure illustrates multiple stable and unstable solutions resulting from bifurcations, superharmonic resonances, and subharmonic resonances, appearing as isolated branches of solutions.

With traditional swept (or stepped) sine testing approaches, the jump phenomenon [39] occurs between different coexisting solutions along the fundamental resonance. Open-loop EMA methodologies cannot fully characterize nonlinear dynamics, as the same excitation can lead to

different responses (folding), and some responses are unstable. Small perturbations can cause the system to diverge from the unstable response.

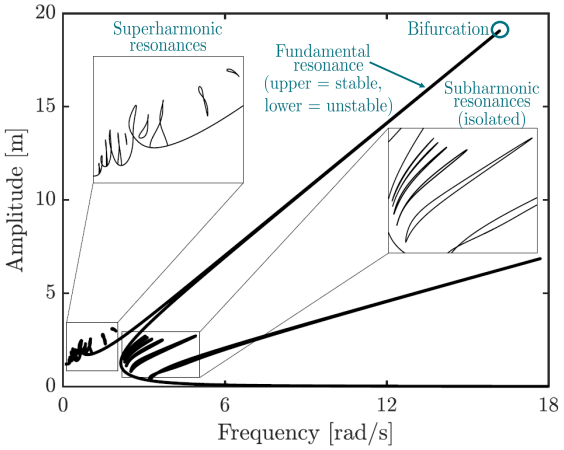

Figure 1.1: Frequency response [77] of a Duffing oscillator $\ddot{x}+0.01\,\dot{x}+x+x^3 = 3\,\sin(\omega\,t)$ calculated using harmonic balance-based numerical continuation [20].

Control-based nonlinear vibration testing (CBNVT) offers a novel approach to testing engineering structures by conducting closed-loop experiments to stabilize all responses. This method uses numerical continuation schemes to explore system dynamics [22, 45, 68]. Sieber and Krauskopf pioneered CBNVT to go around fold bifurcations in numerical examples [70]. The first experimental demonstration tracked periodic orbits through a fold (saddle-node) bifurcation using a parametrically excited pendulum [71]. CBNVT evolved into two main directions: control-based continuation (CBC) [10, 12, 13, 15] and phase-locked loops (PLL) [49, 72].

Identification of fundamental resonances

In PLL, the phase lag between the applied excitation and the system response is controlled. This method was used to find the fundamental resonance or its backbone [1] for various nonlinear structures, including beams and plates with nonlinear stiffness or damping [4, 19, 35, 56, 66]. In these applications, the one-to-one relationship between phase lag and response allows going around fold bifurcations, as shown in Figure 1.2.

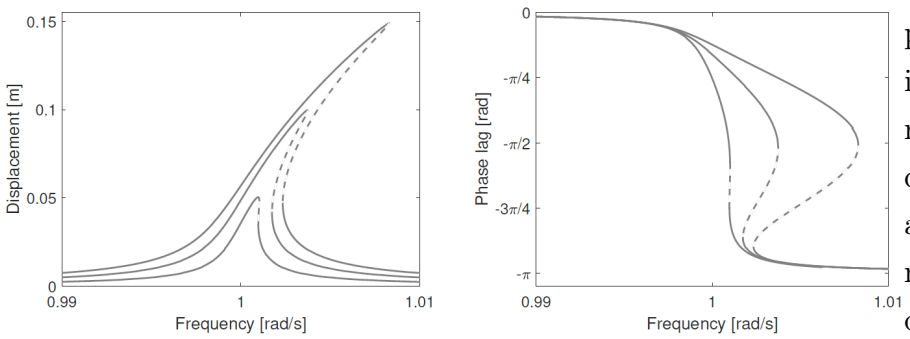

Figure 1.2: Illustration of phase lag monotone behavior around the fundamental resonance of a Duffing oscillator at different forcing amplitudes [83]. Unstable responses are indicated by dashed lines.

CBC controls the structural response x by comparing it to a reference x^* and generating a control action u to stabilize the desired periodic orbit. To maintain non-invasiveness, meaning

[1] The backbone is the collection of amplitude resonance points at different forcing levels.

the stabilized solution matches an open-loop solution, u must be monoharmonic. Typically, non-fundamental harmonics of the reference x^*_{nf} are adjusted using fixed-point iterations. The continuation process moves smoothly from one periodic solution to another by varying x^*. As-

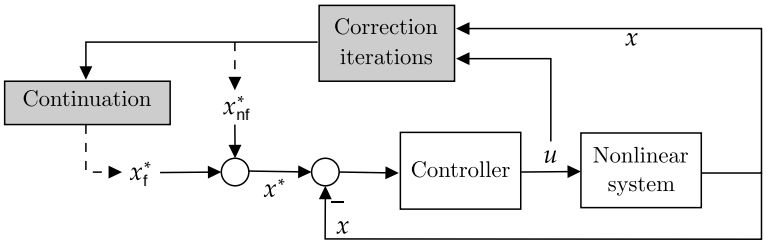

Figure 1.3: Illustration of control-based continuation (CBC) [11]. Grey boxes are performed offline.

suming a derivative controller, its action is $u(t) = k_d \dfrac{\mathrm{d}}{\mathrm{d}t}[x^*(t) - x(t)] = p\,\sin(\omega t)$, where the controlled parameter is either the forcing amplitude p or frequency ω. Both are controlled by the continuation through the reference displacement x^*. In CBC, the choice of the controlled parameter is crucial. Figures 1.4a and 1.4b show three-dimensional plots of displacement amplitude x against both controlled parameters. The manifold (in grey) can be sliced at constant forcing frequency to get FRCs[2] (Figure 1.4a) rather than amplitude to produce S-curves (Figure 1.4b). At the fundamental resonance, forcing frequency shows a non-monotonous increase at constant forcing, requiring advanced continuation schemes. Figure 1.4c highlights that, with high enough controller gains k_d, S-curves feature a monotonous increase in displacement at fixed forcing frequency, allowing simpler continuation schemes. Identifying S-curves provides an indirect but effective method to identify FRCs [11].

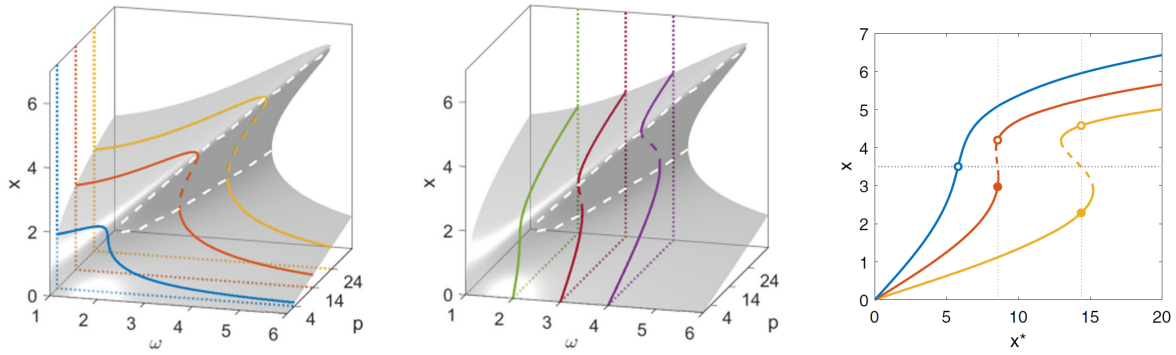

(a) (b) (c)

Figure 1.4: (a-b) Manifold of the Duffing oscillator linking displacement amplitude x, forcing frequency ω and forcing amplitude p with (a) FRC at constant excitation amplitudes and (b) S-curves at constant frequencies. The white dashed line marks the locus of saddle-node bifurcations, representing the boundary between stable and unstable orbits. (c) S-curves for $\omega = 4$ and $k_d = 0.5$ (yellow), 1 (orange), or 2 (blue) with stable (solid line) and unstable (dashed line) orbits. The complete figure is sourced from [3].

This strategy was used to identify features of nonlinear oscillators [4, 61–64] and applied to

[2]FRCs refer to frequency response curves.

frictional systems [42] and biochemical systems [29]. All these studies focused on characterizing the primary resonance of structures.

Abeloos pioneered adaptive filtering for online Fourier decomposition, eliminating the need for offline correction iterations [1, 3]. This simplifies implementation and speeds up experiments. It can be used either for CBC or PLL experiments [83].

Directly identifying folded FRCs would necessitate numerical continuation schemes that involve computing derivatives. Experimentally computing derivatives is challenging due to inevitable noise. Abeloos introduced a novel method for experimental arclength control-based continuation that is both conceptually simple and derivative-free [1, 2]. Figure 1.5 shows preliminary experimental results for a geometrically nonlinear beam. In addition to handling bifurcations and unstable branches, the algorithm identified an isolated branch of periodic solutions with stable and unstable portions. Up to five co-existing solutions are observed for a phase lag around $-\pi/4$.

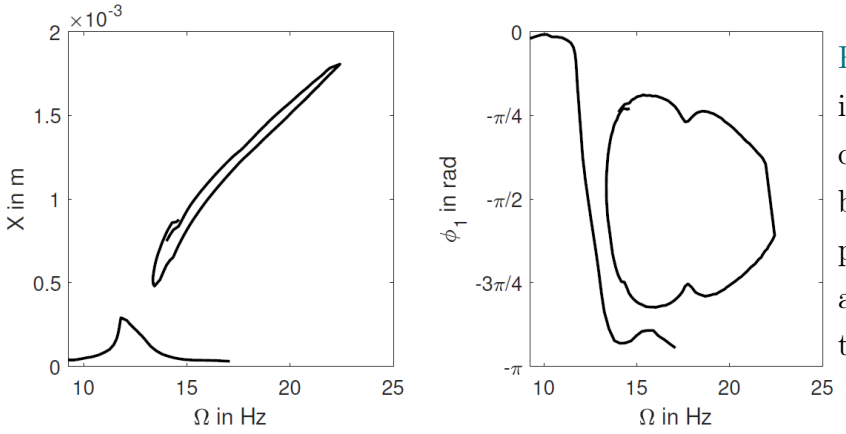

Figure 1.5: Preliminary experimental results of the online, derivative-free arclength control-based continuation method as proposed in [1, 2], applied to a clamped-clamped beam structure.

Identification of secondary resonances

Characterizing superharmonic resonances with the current CBC is not possible because S-curves for these resonances cannot be unfolded [1].

Using phase resonance nonlinear modes [77], Zhou recently investigated PLL to identify the backbones of superharmonic and subharmonic resonances, and the nonlinear FRC near these resonances. A numerical Duffing oscillator and a clamped-clamped experimental system were studied [83]. As shown in Figure 1.6, superharmonic resonances were successfully identified, but subharmonic resonances were not fully captured. For isolated responses, a phase lag does not correspond to a unique response, as illustrated in Figure 1.5.

Abeloos developed a new definition of phase lag in PLL that accounts for multiple harmonics to compute odd superharmonic resonances in systems with modal coupling [1]. When the backbones of two resonances intersect, modal interactions can prevent the PLL from stabilizing

some orbits. CBC can be combined with PLL testing to stabilize these orbits in a clamped-clamped beam structure [1, 28].

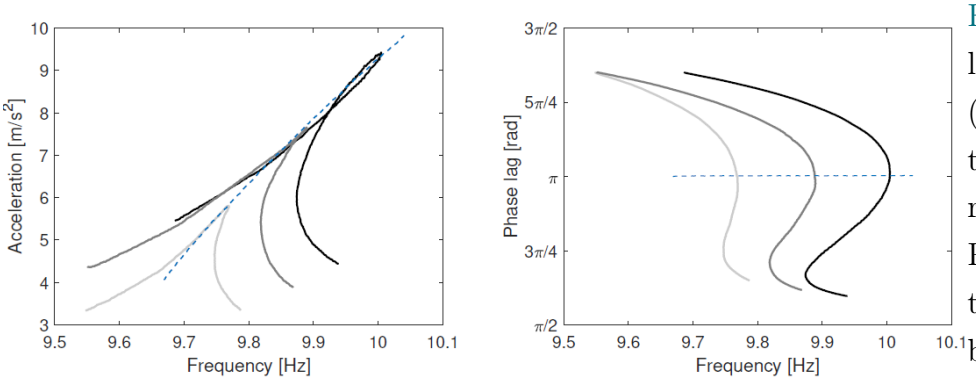

Figure 1.6: FRCs (solid lines) and backbone (blue dashed line) of the 2 : 1 superharmonic resonance identified by PLL testing applied to a clamped-clamped beam structure [83].

Apart from these two studies, the literature rarely addresses the identification of nonlinear frequency response curves for secondary resonances. These studies used PLL for conservative cubic and quadratic nonlinearities and highlighted limitations in detecting isolated responses. No recent attempts have been made to identify secondary resonances with CBC.

1.1. Objectives

This research aims to advance the methodology proposed by Abeloos for online, derivative-less control-based nonlinear vibration testing, termed ACBC. This method is designed to experimentally identify frequency responses of nonlinear systems subjected to harmonic forcing, without relying on predefined mathematical models. The algorithm is implemented in Matlab/Simulink, which can easily be used by a real-time controller such as a MicroLabBox from dSPACE for experimental validation.

This master's thesis attempts to answer two key questions:

a) Is the ACBC algorithm capable of identifying the complete frequency response of a numerical/electronic Duffing oscillator, including secondary resonances with complex topology?

b) How can the step size selection in the ACBC algorithm be automated to ensure accurate frequency response capture?

This work is divided into nine chapters. Chapter 2 examines dimensionless single-degree-of-freedom linear and nonlinear oscillators: how do the resonance behaviors of linear and nonlinear systems differ? Chapter 3 provides a qualitative overview of PID control: what is the role of tuning the proportional, integral, and derivative terms? Chapter 4 presents the traditional CBC and the ACBC method, emphasizing the improvements the latter introduces for the direct identification of FRCs. Chapter 5 identifies the FRC of a numerical Duffing oscillator using the ACBC method: what challenges arise in identifying fundamental and secondary

resonances? Chapter 6 enhances the ACBC algorithm to better identify both attached and isolated secondary resonances by introducing control of a non-fundamental harmonic of the response, called the double sweep strategy. Previous chapters focused on identifying the FRC of a numerical Duffing oscillator. Chapter 7 applies the original ACBC algorithm and the double sweep strategy to an electronic Duffing oscillator, demonstrating the algorithms' performance in an experimental environment. Chapter 8 proposes an adaptive strategy in the ACBC method to adjust the step size based on the local curvature of the FRC. Chapter 9 presents the conclusions and future perspectives.

2 | Resonances of linear and nonlinear systems

The dynamical behavior of linear systems is well-documented, both theoretically and experimentally [31, 36]. Despite the inherently nonlinear nature of most structures, linear analysis remains extensively used. In mechanical engineering, linear assumptions are valid for small displacements. Within this linear regime, systems exhibit nearly mono-harmonic responses to mono-harmonic inputs, with resonances occurring at specific frequencies, independent of the amplitude of the forcing.

Overlooking strong nonlinear effects can cause inconsistencies between numerical models and experimental outcomes. Significant excitations of nonlinear systems result in multi-harmonic responses and cause resonance frequencies to shift with increasing amplitude [54]. These shifts lead to multi-stable regions and the jump phenomenon [50]. Additionally, new resonances may emerge at fractions or multiples of the amplitude-dependent fundamental resonance frequency [53]. This complicates the prediction and identification of the system's frequency response.

This chapter aims to compare the responses of linear and nonlinear systems. It illustrates phenomena in nonlinear structures through the study of a simple academic system. It builds on concepts from the course *Nonlinear Vibrations of Aerospace Structures* taught by Professor Kerschen at the University of Liège [38].

2.1. Dimensionless Duffing oscillator

This work investigates the well-known single-degree-of-freedom Duffing oscillator [43], with linear viscous damping and subjected to harmonic forcing. Only steady-state responses are considered. The Duffing system is characterized by a cubic stiffness and the governing equation of motion is

$$m\,\ddot{x}(t) + c\,\dot{x}(t) + k\,x(t) + k_3\,x^3(t) = p\,\sin(\omega t) \tag{2.1}$$

with the displacement $x(t)$, the mass m, the linear stiffness k, the cubic stiffness k_3, the linear viscous damping c, the excitation amplitude p, and the excitation frequency ω. The dots over variables indicate time derivatives.

The mass-normalized equation of motion is

$$\ddot{x}(t) + 2\,\zeta\,\omega_0\,\dot{x}(t) + \omega_0^2\,x(t) + \alpha_3\,x^3(t) = f\,\sin(\omega t) \tag{2.2}$$

Here, $\omega_0 = \sqrt{k/m}$ denotes the natural frequency, $\zeta = \dfrac{\omega_0\,c}{2\,k}$ the modal damping coefficient, α_3 the mass-normalized cubic stiffness, and f the mass-normalized force amplitude. This equation is a second-order nonlinear differential equation with constant coefficients. Two initial conditions are necessary, i.e. $x(0) = x_0$ and $\dot{x}(0) = \dot{x}_0$.

The next step is to nondimensionalize the system, allowing the results to apply to any Duffing system.

First, applying the change of variable $\tau = \omega_0 t$, , Equation (2.1) becomes

$$\omega_0^2\,m\,x'' + \omega_0\,c\,x' + k\,x + k_3\,x^3 = p\,\sin\left(\frac{\omega}{\omega_0}\,\tau\right). \tag{2.3}$$

Derivatives with respect to τ are denoted by $'$.

Second, by introducing the variables $\bar{x} = x/\sigma$ and $\bar{\omega} = \omega/\omega_0$, and dividing Equation (2.3) by k, it becomes

$$\bar{x}'' + 2\,\zeta\,\bar{x}' + \bar{x} + \sigma^2\,\frac{k_3}{k}\,\bar{x}^3 = \frac{p}{\sigma k}\,\sin(\bar{\omega}\,\tau). \tag{2.4}$$

The dimensionless transformation is completed by setting σ as $\sqrt{k/k_3}$, leading to the final nondimensionalized form of the equation:

$$\bar{x}'' + 2\,\zeta\,\bar{x}'(\tau) + \bar{x} + \bar{x}^3 = \bar{p}\,\sin(\bar{\omega}\,\tau) \tag{2.5}$$

The parameters ζ and $\bar{p}$ remain arbitrary in this dimensionless equation.

Therefore, Equation (2.2) is nondimensionalized by setting ω_0 and α_3 to unity. This is equivalent to setting m, k, and k_3 to unity in Equation (2.1). These unit parameters are adopted throughout this work, as detailed in Table 2.1. The force amplitude will be specified in each case.

m [kg]	c [Ns/m]	k [N/m]	k_3 [N/m^3]	ω_0 [rad/s]	α_3 [N/(m^3 kg)]	ζ [%]
1	0.01	1	1	1	1	0.5

Table 2.1: Set of parameters for the Duffing oscillator.

2.2. Single-degree-of-freedom (SDOF) linear and nonlinear systems

The Duffing system is progressively explored, starting from the basic undamped and unforced scenario and advancing to the damped and forced scenario. At each step, the system is analyzed both with and without nonlinearity.

2.2.1. Undamped and unforced SDOF systems

In the linear case, Equation 2.2 is modified to describe the free motion of the undamped single-degree-of-freedom oscillator:

$$\ddot{x}(t) + \omega_0^2\, x(t) = 0, \qquad x(0) = x_0,\ \dot{x}(0) = \dot{x}_0. \tag{2.6}$$

After some manipulation, detailed in [38], the solution to this equation is formulated as:

$$x(t) = \sqrt{x_0^2 + \frac{\dot{x}_0^2}{\omega_0^2}}\ \sin\left(\omega_0\, t + \tan^{-1}\left(\frac{\omega_0\, x_0}{\dot{x}_0}\right)\right). \tag{2.7}$$

The response of the linear oscillator exhibits harmonic motion with the natural frequency ω_0, which solely relies on the parameters k and m.

In the nonlinear case, the equation describing the free motion of the undamped single-degree-of-freedom oscillator is:

$$\ddot{x}(t) + \omega_0^2\, x(t) + \alpha_3\, x^3(t) = 0, \qquad x(0) = x_0,\ \dot{x}(0) = \dot{x}_0. \tag{2.8}$$

The set of initial conditions, $[x(0),\ \dot{x}(0)] = [x_0,\ 0]$, is used for comparison with the linear case. After some manipulations detailed in [38], the solution to the nonlinear equation is written

$$x(t) = x_0\, \mathrm{cn}(\Omega\, t \,|\, \kappa) \tag{2.9}$$

with the motion frequency $\Omega = \sqrt{\omega_0^2 + \alpha_3\, x_0^2}$ and $\kappa = \alpha_3\, x_0^2 \,/\, 2\,\Omega^2$. The symbol cn denotes the mathematical function called the elliptic cosine [38].

Two key observations can be made from the analytical solution. The response of the nonlinear oscillator does not take the form of a harmonic function. The frequency Ω depends on the linear stiffness k and the mass m, as in the linear case. The frequency also depends on the initial displacement x_0 and the nonlinear coefficient α_3.

Figure 2.1 shows the free responses of both linear and nonlinear undamped oscillators to various initial displacements.

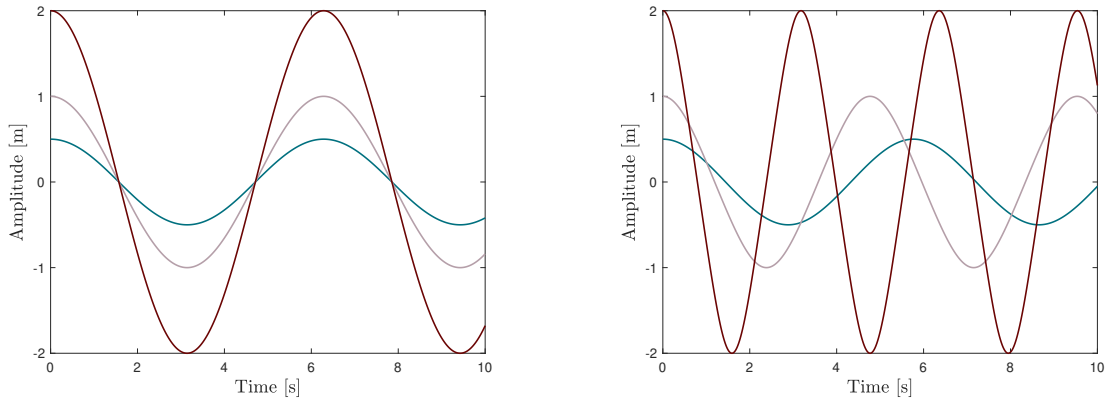

(a) (b)

Figure 2.1: (a) Linear and (b) nonlinear undamped oscillator responses for various initial displacements ($\dot{x}_0 = 0$ m/s): $x_0 = 0.5$ m (—), $x_0 = 1$ m (—), and $x_0 = 2$ m (—).

The principle of superposition stipulates that the response generated by multiple inputs is equivalent to the sum of the responses induced by each input individually. While this principle holds for the linear oscillator, as depicted in Figure 2.1a, it no longer applies to the nonlinear oscillator, as evident in Figure 2.1b. This deviation can be explained by the dependency of the motion frequency Ω on the initial conditions. For the undamped case, there is no energy dissipation, preserving both energy and oscillation amplitude over time.

Although the elliptic cosine closely resembles a pure cosine function, the response of the nonlinear oscillator deviates from harmonic motion. This is clearly highlighted when examining the acceleration in Figure 2.2a.

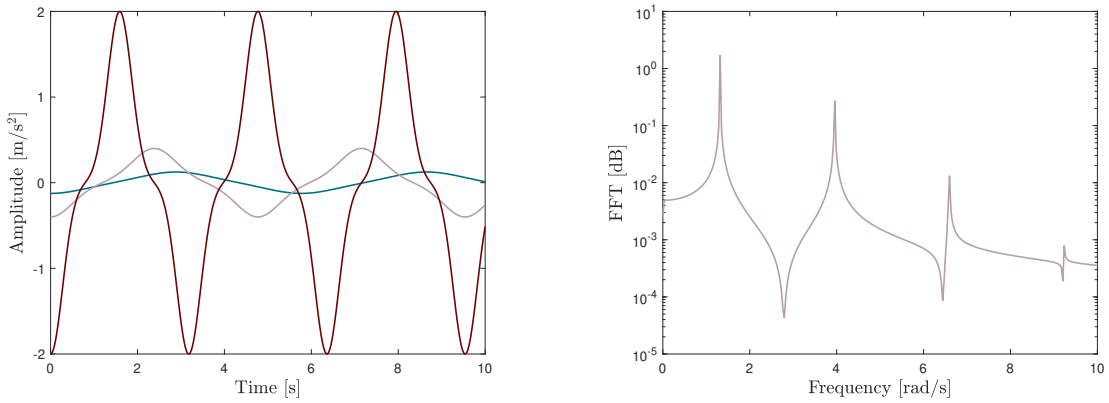

(a) (b)

Figure 2.2: (a) Acceleration response of a nonlinear undamped oscillator for different initial conditions ($\dot{x}_0 = 0$ m/s): $x_0 = 0.5$ m (—), $x_0 = 1$ m (—), and $x_0 = 2$ m (—). (b) Fast Fourier Transform of the acceleration response for the initial conditions $[x_0, \dot{x}_0] = [1, 0]$.

The acceleration profile lacks harmonic behavior, differing significantly from the linear case.

The Fast Fourier Transform of the acceleration response is illustrated in Figure 2.2b. The most prominent peak denotes the fundamental resonance. The amplitude of the first harmonic alone is inadequate for reconstructing the total amplitude. At higher frequencies, three additional peaks are visible, corresponding to the third, fifth, and seventh harmonics, respectively. This observation emphasizes the generation of harmonics by nonlinear systems.

Figure 2.3 illustrates the effects of both the sign and magnitude of the nonlinear coefficient α_3. As mentioned previously, the motion frequency Ω depends on the nonlinear coefficient. Since the nonlinearity arises from the cubic displacement term, the sign of the nonlinear coefficient determines whether the system's stiffness increases or decreases relative to the linear case. A larger positive nonlinear coefficient results in increased stiffness within the system.

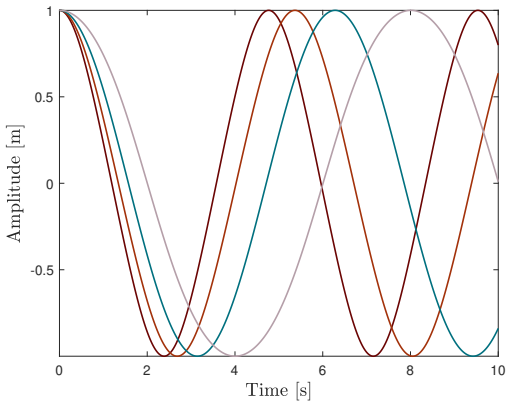

Figure 2.3: Nonlinear undamped oscillator responses for $[x_0, \dot{x}_0] = [1, 0]$ and various nonlinear coefficients: $\alpha_3 = -0.5$ N/m^3/kg (—), $\alpha_3 = 0$ N/m^3/kg (—), $\alpha_3 = 0.5$ N/m^3/kg (—), and $\alpha_3 = 1$ N/m^3/kg (—).

The comparative analysis between undamped linear and nonlinear oscillators reveals distinct behaviors. Nonlinear oscillators deviate from purely harmonic responses, violate the superposition principle, exhibit frequency-amplitude dependency, and generate harmonics.

Jacobi elliptic functions cannot provide an exact analytical solution for the nonlinear damped case, and no closed-form solution exists for forced or unforced systems. In this scenario, the harmonic balance method (HBM) is commonly used, reconstructing the system's response with a combination of sinusoidal functions.

2.2.2. Harmonic Balance Method

The harmonic balance method is widely used in the literature for examining the periodic solutions of nonlinear mechanical systems [20, 44, 58]. This technique is also referred to as the Fourier–Galerkin method because it applies the Galerkin method using Fourier basis and test functions.

The method relies on the assumption that every nonlinear steady-state response of a system, subjected to an excitation frequency ω, can be represented by an infinite Fourier series of harmonics of this frequency. In practice, truncated Fourier series up to the order N represent

the periodic solutions, i.e.

$$x(t) = \frac{c_0}{\sqrt{2}} + \sum_{l=1}^{N} \Big(s_l \, \sin(\omega_l \, t) + c_l \, \cos(\omega_l \, t) \Big) \tag{2.10}$$

where $\omega_l = \dfrac{l\omega}{\nu}$, with ν is an integer. The Fourier coefficients s_l and c_l are the new unknowns of the problem. The fundamental harmonic is defined as the harmonic within the series where $l = \nu$, whereas the secondary harmonics represent all other harmonics where $l \neq \nu$.

The methodology proceeds as follows. First, the approximation is substituted into the equations of motion. Then, the coefficients associated with a specific harmonic ω_l are equated, while higher-order harmonic terms produced by nonlinearities are neglected. This process yields a set of $2N+1$ nonlinear algebraic equations to solve for $2N+2$ unknowns, i.e. ω and the $2N+1$ Fourier coefficients. To close the system, an additional equation is required. Typically, the cosine coefficient of the first harmonic is set to 0. The resulting nonlinear algebraic system can be solved using methods such as Newton-Raphson iterations.

The HBM is advantageous for its accuracy with low-order approximations, especially with smooth nonlinearities. While adding more harmonics can enhance accuracy, typically only the first few with significant amplitudes are retained, particularly in large-scale nonlinear systems where balancing accuracy and computational cost is crucial.

2.2.3. Damped and forced SDOF systems

All physical systems are damped. To better stick to reality, viscous damping is introduced to model dissipation. Additionally, mechanical systems are not left free by the environment. To assess the forced response of the studied system, a periodic signal is often applied to observe the response of the system at a particular frequency or in a frequency range.

Under harmonic forcing, the governing equation of the damped linear SDOF oscillator becomes

$$\ddot{x}(t) + 2\,\zeta\,\omega_0\,\dot{x}(t) + \omega_0^2\,x(t) = f\,\sin(\omega\,t), \qquad x(0) = x_0,\ \dot{x}(0) = \dot{x}_0. \tag{2.11}$$

The solution of this second-order ordinary differential equation can be decomposed into a homogeneous solution (for the unforced system) and a particular solution. For the steady-state response, only the particular solution is relevant. Details on computing the particular solution are provided in [38]. The particular solution x_p is

$$x_p(t) = \frac{f}{\sqrt{(\omega_0 - \omega^2)^2 + (2\zeta\,\omega_0\,\omega)^2}} \sin\left(\omega\,t - \tan^{-1}\left(\frac{2\,\zeta\,\omega_0\,\omega}{\omega_0^2 - \omega^2}\right)\right). \tag{2.12}$$

Figure 2.4 shows the amplitude and phase of the FRF for a damped linear system, varying with different damping coefficients.

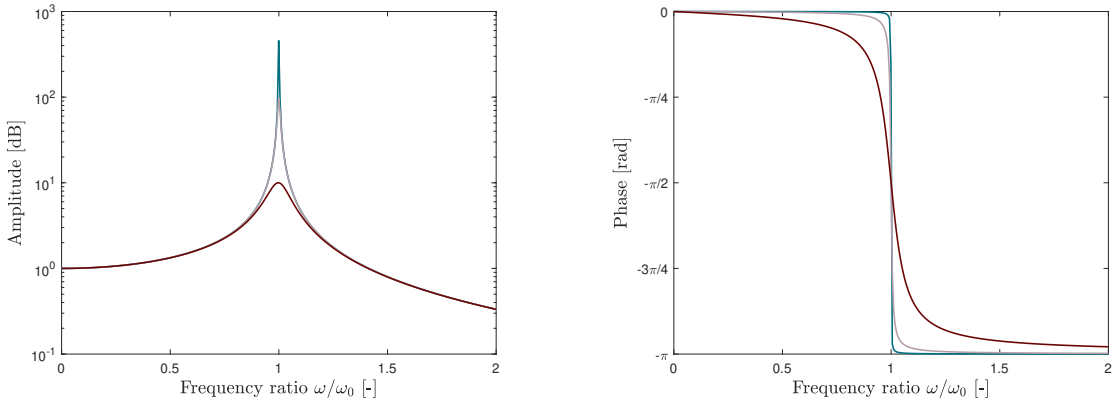

(a) (b)

Figure 2.4: (a) Amplitude and (b) phase Bode plots for the frequency response of a damped linear SDOF system with varying damping levels: $\zeta = 0.05\%$ (—), $\zeta = 0.5\%$ (—), and $\zeta = 5\%$ (—).

In linear theory, the frequency response function (FRF) is commonly used because it remains constant for linear systems and is easily estimated from measured data. It is especially useful for identifying resonance frequencies. The FRF is defined as the ratio of the Fourier transform of the response $x_p(t)$ to the Fourier transform of the excitation $f(t)$.

The scaling of x_p with f illustrates the validity of the principle of superposition. The steady-state response remains independent of the initial conditions. Additionally, as ω approaches ω_0, the amplitude of the steady-state response grows significantly, even with small forcing amplitudes. This phenomenon is known as resonance.

Resonance can be defined in two ways. First, amplitude resonance is intuitively identified as a local maximum in the FRF. Second, phase resonance, introduced by Fraiejs de Veubeke [25], occurs when the motion is in quadrature with the excitation, resulting in a phase lag of $\pi/2$. In lightly damped structures, phase resonance is very close to amplitude resonance.

The forced response of the damped nonlinear SDOF oscillator can also be analyzed. The governing equation is

$$\ddot{x}(t) + 2\,\zeta\,\omega_0\,\dot{x}(t) + \omega_0^2\,x(t) + \alpha_3\,x^3(t) = f\,\sin(\omega\,t), \qquad x(0) = x_0,\ \dot{x}(0) = \dot{x}_0. \tag{2.13}$$

Figure 2.5 shows the frequency response computed using HB continuation. Stability analysis is performed using Hill's method in the HBM formalism [34, 78]. As shown in Figure 2.5a, the nonlinear equivalent of the FRF varies with the forcing amplitude and is no longer a function. It is referred to as the nonlinear frequency response curve (FRC).

Volvert extensively investigated the frequency response of the Duffing oscillator [77]. Each harmonic l of the Fourier series of the response (cf. Equation (2.10)) may resonate if $\omega_l = l\,\omega/\nu$

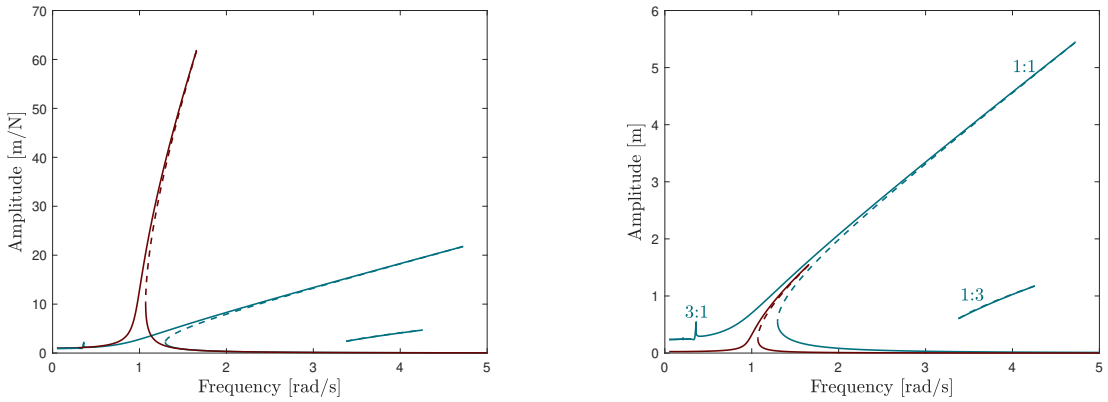

Figure 2.5: (a) Scaled and (b) unscaled nonlinear frequency response of the Duffing oscillator for various forcing levels: $f = 0.025$ N/kg (—), and $f = 0.25$ N/kg (—). Stable branches are shown with solid lines and unstable branches with dotted lines. Results obtained using HB continuation.

aligns with the (amplitude-dependent) frequency of the primary resonance of the system. Stoker [73] categorized resonances into four distinct categories, namely

- $1:1$ primary/fundamental resonance $l = \nu = 1$;
- $l:1$ superharmonic or ultra harmonic resonances;
- $1:\nu$ subharmonic resonances;
- $l:\nu$ ultra-subharmonic resonances.

This work excludes ultra-subharmonic resonances. It focuses on the most significant resonances: the fundamental resonance, and the first super- and sub-resonances.

Figure 2.5b shows that as the forcing level increases, the fundamental resonance peak shifts to higher frequencies. This shift creates regions with multiple solutions at the same frequency, marked by fold bifurcations where the slope of the excitation frequency with respect to amplitude is zero.

Bifurcations give rise to multi-valued responses and alter stability, as shown in Figure 2.6. Before and after the bifurcation points, only one stable solution exists (red or blue line). Between these points, two are stable (red or blue lines) and one is unstable (dashed line). The steady-state response depends on initial conditions, which define the system's basins of attraction and determine the converging solution. Even a minor perturbation will cause the system to deviate from the unstable solution. The jump phenomenon occurs when the system transitions from three solutions to one.

In Figure 2.5, secondary resonances are observed at $f = 0.25$ N/kg when the system is excited away from its natural frequency ω_0. These are the third and one-third harmonic resonances,

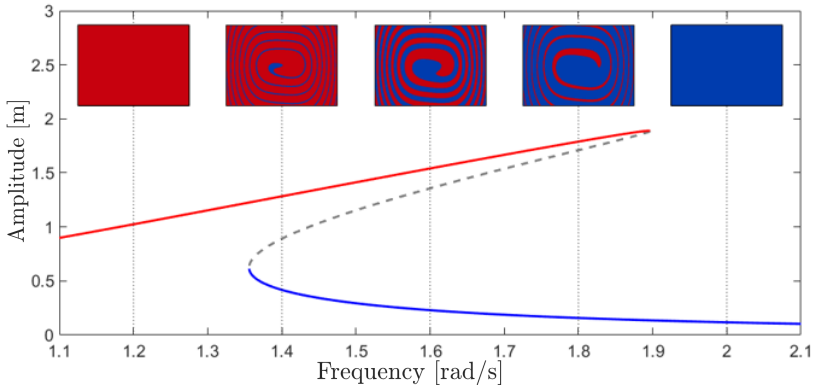

Figure 2.6: FRC of the fundamental resonance, showing stable (colored lines) and unstable (dashed line) solutions. Basins of attraction are indicated in the boxed areas, which represent the attractor toward which the system at given initial conditions $(x_0, \dot{x}_0)$ converges.

located around $\omega_0/3$ and $3\,\omega_0$, respectively. As shown in Figure 2.7 or Figure 2.8, the amplitude of the third, and one-third harmonics reaches a local maximum and dominates in these frequency regions.

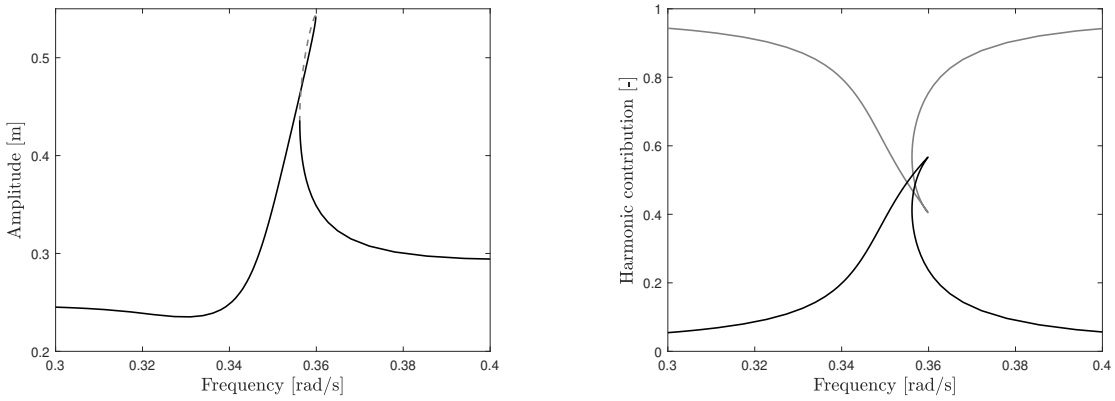

(a) (b)

Figure 2.7: (a) FRC around the 3 : 1 superharmonic resonance ($f = 0.25$ N/kg) with stable branches (black) and unstable branches (grey). (b) Amplitude contribution of the third harmonic (black) and first harmonic (grey). Results obtained using HB continuation.

Secondary resonances can be attached or detached from the main branch, depending on system characteristics and forcing level. Like primary resonances, secondary resonances can exhibit unstable and multi-stable solutions between fold bifurcations. In Figure 2.5, secondary resonances are absent at lower forcing level due to insufficient excitation.

For the 1 : 3 subharmonic resonance, there are three potential solutions, each with the same maximum amplitude and a phase lag shifted by $2\,\pi/3$. This phase shift from t to $t + \frac{2\,\pi}{3\,\omega}$ does not affect the fundamental harmonic, as $3\,\omega\,(t + 2\,\pi/(3\,\omega)) = 3\,\omega\,t + 2\,\pi = 3\,\omega\,t \bmod (2\,\pi)$. In general, for subharmonic resonances, ν solutions exist with the same maximum amplitude and

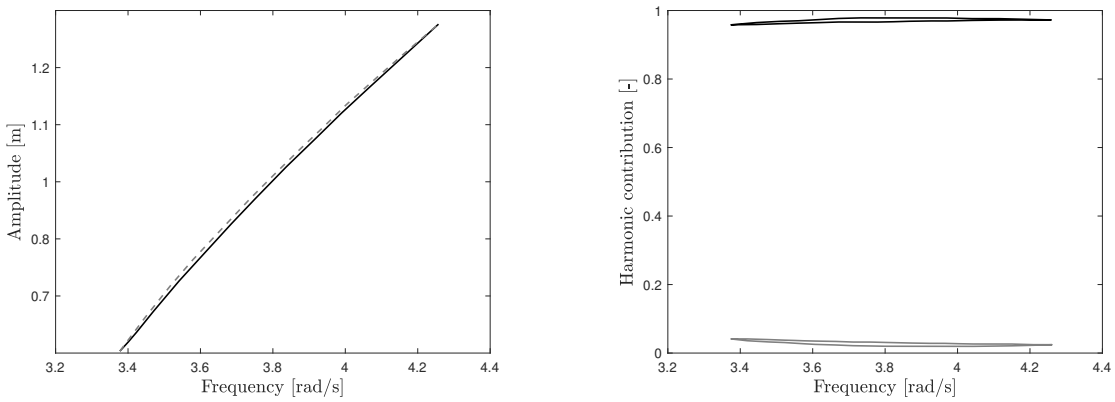

(a) (b)

Figure 2.8: (a) FRC around the $1:3$ superharmonic resonance ($f = 0.25$ N/kg) with stable branches (black) and unstable branches (grey). (b) Amplitude contribution of the one-third harmonic (black) and first harmonic (grey). Results obtained using HB continuation.

a phase lag shifted by $2\pi/\nu$. Volvert discussed this in [77].

Melnikov-type analyses, which use perturbations of solutions, have established criteria necessary for the occurrence of subharmonic and superharmonic resonances [16, 30]. These analytical methods apply to strong nonlinearities but are limited to weak forcing and damping.

2.3. Reference case

In the following chapters, the goal is to determine the frequency response of the Duffing system under a harmonic forcing of $f = 1$ N/kg. Figure 2.9 presents the FRC obtained using HB continuation. Besides the $3:1$ and $1:3$ resonances, additional secondary resonances appear both below and above the primary resonance. As the forcing increases, each secondary resonance becomes prominent.

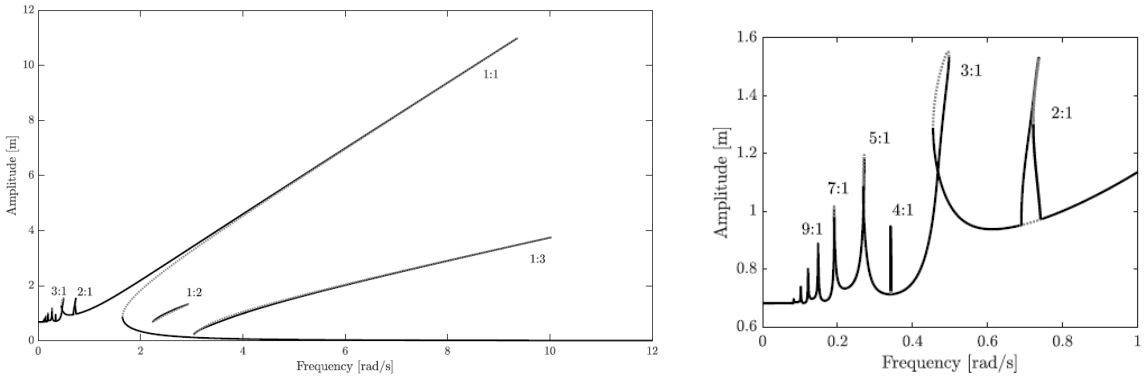

(a) (b)

Figure 2.9: (a) FRC of the Duffing oscillator ($f = 1$ N/kg), with stable branches (black) and unstable branches (grey). (b) Zoomed version. Results obtained using HB continuation from Volvert's thesis [76].

In Figure 2.9b, superharmonic resonances of the form $l:1$, where l is odd, extend along the continuation of the main branch. Resonances such as $3:1$, $5:1$, $7:1$, $9:1$, and so forth are observed. At constant forcing amplitude, odd $l:1$ resonances are more pronounced for lower l values. Their shape depends on the forcing level. Initially, they appear as peaks devoid of folding (e.g. $9:1$), subsequently forming a loop with fold bifurcations (e.g. $3:1$).

Even $l:1$ resonances, such as the $2:1$ resonance shown in Figure 2.9b, bifurcate from the main branch. The $2:1$ and $4:1$ resonances result from symmetry-breaking bifurcations. Initially, the response of the perfectly symmetric Duffing system has only odd harmonics. Between two symmetry-breaking bifurcations, both odd and even harmonics are present. At the bifurcation point, the system transitions from the stable main branch with odd harmonics to an unstable branch, while a new stable branch with both odd and even harmonics forms. This new resonance branch also exhibits fold bifurcations at its top.

The newly-created $1:2$ subharmonic resonance is observed at around $2\,\omega_0$.

The phase evolution is not discussed here because it is not used in the methods developed in the next chapters. In nonlinear systems, the phase quadrature of resonances is not always $\pi/2$, unlike the linear case. Volvert examines the phase quadrature evolution for the Duffing oscillator in [77].

2.4. Conclusions

This chapter demonstrated the main differences between the resonance behavior of linear and nonlinear systems using a Duffing oscillator characterized by cubic stiffness. Starting with undamped and unforced cases, complexity was added by incorporating damping and external harmonic forcing.

Analytical solutions were found for linear cases, while for nonlinear cases, analytical solutions only exist for the undamped and unforced single-degree-of-freedom Duffing system. A numerical approximation of the response is possible using the harmonic balance method.

The resonant behavior of nonlinear systems is more complex than that of linear systems. The fundamental resonance peak shifts to higher frequencies, and fold bifurcations create regions with both stable and unstable solutions. The jump phenomenon, where the system transitions from multiple solutions to one, can cause rapid amplitude changes over a short frequency range, potentially damaging the structure [41, 84]. Another major difference from linear systems is the presence of multiple harmonics in the response. Each harmonic can resonate if $\omega_l = l\,\omega/\nu$ matches the amplitude-dependent frequency of the fundamental resonance. Odd $l:1$ superharmonic resonances extend from the main branch and can be calculated using classical HB continuation. In contrast, even $l:1$ superharmonic resonances bifurcate from the main branch and require advanced bifurcation analysis [20, 21, 81]. The $1:\nu$ subharmonic resonances

appear as isolated branches, needing a minimum forcing amplitude and basin of attraction calculations for identification.

3 Basics of control theory

Feedback control is an interdisciplinary field applied across all areas of engineering. The core idea is to measure a system's output and use it to adjust a controller, ensuring a system variable aligns with a specific reference value. This approach ensures dynamic systems perform optimally, maintain stability, and adapt to changing conditions and disturbances, even with imperfect design models or varying system dynamics.

PID control is one of the earliest feedback control strategies and is widely used in practical engineering applications [46, 69, 82]. Developed through extensive experience and trial and error, it evolved from simple proportional feedback (P) to include integral control (PI) for eliminating steady-state offset. Later, an anticipatory derivative term was added, resulting in the PID controller to improve dynamic response. Its simple structure, reliable operation, and ease of adjustment have made it a mature method in industrial control. PID control is especially useful when the system's structure and parameters are not well understood or when an accurate mathematical model is hard to obtain. They are thus particularly well suited for a model-less approach such as CBC.

The main objective of this chapter is to provide a qualitative understanding of tuning the proportional, integral, and derivative terms of PID control. It begins with a brief review of open-loop and closed-loop control systems, followed by an explanation of how to analyze the step response for control design. Finally, the chapter covers PID control by examining its three components. The discussion draws on concepts from [26, 85].

3.1. Control system structures

The two main control structures are the open- and closed-loop control systems. Figure 3.1 illustrates block diagrams for both control systems.

Each system includes two key components: the process and the controller, depicted as boxes with arrows indicating the causal relationship between inputs and outputs. The process has an input, known as the control variable u, and an output, known as the process variable y. A sensor measures the output, and an actuator provides the input. The desired value of the process variable is referred to as the setpoint or reference value y_{sp}. The control error $e = y_{sp} - y$ is determined by comparing this setpoint to the actual output. The controller's input varies

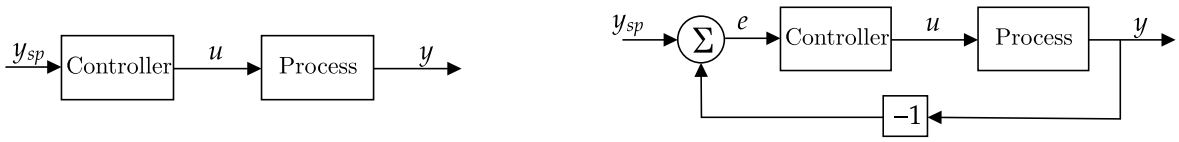

(a) (b)

Figure 3.1: (a) Block diagram of an open-loop system. (b) Block diagram of a closed-loop system.

depending on whether open-loop or closed-loop control is used. The purpose of both control systems is to keep the process variable close to the desired value.

The process can be any dynamical system whose dynamics need to be controlled. To illustrate the variables, a simple example can be considered. An aircraft's autopilot system consists of ensuring the aircraft follows the desired flight path and maintains stable flight conditions. The process variable y can be the aircraft's altitude, heading, or airspeed, measured by onboard sensors. The control variables u are the adjustments made to the control surfaces (such as ailerons, elevators, and rudder) and engine thrust. The desired flight parameters, set by the pilot or the autopilot system, represent the setpoint y_{sp}.

3.1.1. Open-loop control

Open-loop control is a system where the output does not affect the input control action. As illustrated in Figure 3.1a, the controller action modifies the reference variable before it is applied to the process.

The performance of open-loop control, determined by the control error, depends on the user's expertise and system knowledge. Applying the example of an aircraft autopilot with open-loop control, it would adjust its parameters based on the desired altitude or speed, without using feedback from the aircraft's actual motion.

3.1.2. Closed-loop control

Closed-loop control is a system in which the process output is fed back to adjust the controlled input of the process. The closed feedback loop connecting the process and the controller is depicted in Figure 3.1b.

The goal of the feedback loop is to keep the process variable y close to the desired value y_{sp} despite disturbances and variations of the process characteristics. Feedback is a simple yet powerful concept. To illustrate, consider a system in equilibrium that experiences a disturbance, causing the process variable y to exceed the setpoint y_{sp}. This results in a negative error e, causing the controller to reduce the controlled variable u which then decreases the process output y. This mechanism is known as negative feedback because the controlled variable u

moves in the opposite direction to the process variable y. In the block diagram, the sign-reversing block indicates the negative feedback.

In general, closed-loop systems have better performance than open-loop systems. The lack of feedback can lead to decreased precision and responsiveness to system or environmental changes, especially if the process is not perfectly known by the designer. Proper control design is essential to ensure good performance.

3.2. Control design

The design of controllers is often based on their step response. The step response is the response of the system when subjected to an abrupt change of one parameter, typically from zero to a constant value, at a specified time. The step response reveals how the system transitions from its initial state to a new steady state in response to this sudden change.

Figure 3.2 shows the time-domain specifications for this step response.

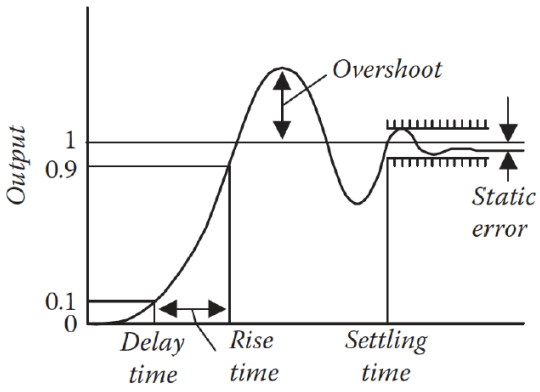

Figure 3.2: Time-domain specifications defined for the step response.

Some specifications correspond the the amplitude of the response. The static or steady-state error is the difference between the final steady-state output and the desired output value (1 here). The overshoot is the amount by which the system output exceeds its final steady-state value, expressed as a percentage of that value.

Other specifications relate to the time axis. The settling time is the time required for the response to reach the steady state and stay within the specified tolerance bands around the final value. In general, the tolerance bands are 2% or 5%. The response up to the settling time is known as the transient response and the response after the settling time is known as the steady-state response. The rise time is the time required for the response to rise from 10% to 90% of its final value. The delay time is the time required for the response to reach 10% of its final value from the zero instant.

To ensure good control design, the effects of load disturbances, measurement noise, and model uncertainties must also be assessed. This can be done using frequency-domain specifications,

which are linked to time-domain specifications. Comprehensive control design is beyond this study's scope. For details, see [26, 85].

3.3. PID control

The most common feedback control strategy used in practice is the PID control. Mathematically, the law governing the PID control variable u is a sum of three terms based on the control error e:

$$u(t) = K\, e(t) + \frac{1}{T_i} \int_0^t e(t)\, dt + T_d \frac{d}{dt} e(t). \tag{3.1}$$

The first term is proportional to the error, the second term to the integral of the error, and the third term to the derivative of the error. The controller parameters are the proportional gain K, the integral time T_i, and the derivative time T_d.

In the literature, another formulation of the controlled parameters is often encountered with $k_p = K$ the proportional gain, $k_i = 1/T_i$ the integral gain, and $k_d = T_d$ the derivative gain.

The choice of controller parameters influences the controlled input of the process, and consequently, the process output.

3.3.1. Proportional action

Initially, the idea of solely proportional control was proposed to adapt the control action proportionally to the current error. The control action is reduced if the error decreases, and increases as the error increases. The control law of Equation (3.1) becomes

$$u(t) = K\, e(t). \tag{3.2}$$

Figure 3.3 shows the controller output u and the process output y after a step change in the setpoint y_{sp} for different values of proportional gain K.

A proportional controller alone cannot ensure zero steady-state error. As the proportional gain K increases, the system exhibits more oscillations and greater overshoot, bringing the steady-state process output y closer to the setpoint y_{sp}. Larger proportional gains allow for a reduction of the rise time. Excessively high loop gains can destabilize the closed-loop system.

3.3.2. Integral action

The introduction of the integral term aims to eliminate the steady-state error. The integral action guarantees an increasing (respectively decreasing) control action no matter how small the positive (respectively negative) control error is. A simple way to visualize this is to assume a system in a steady state with a constant control signal u_0 and constant error e_0. For this PI

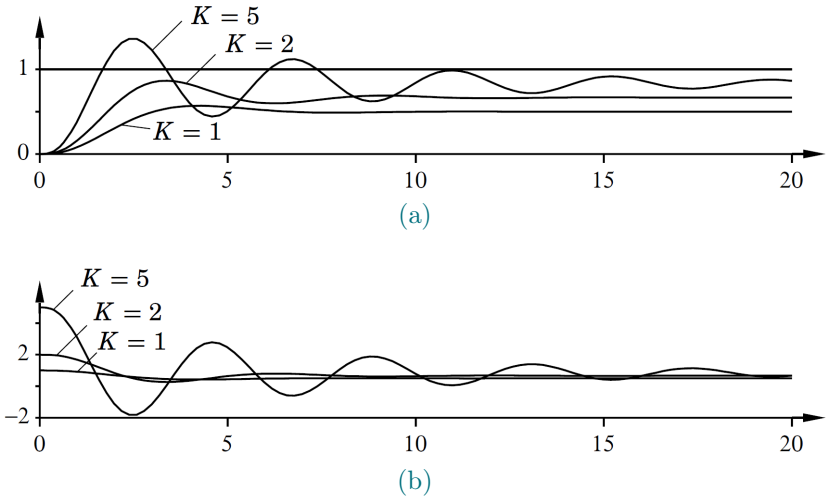

Figure 3.3: Step response of a closed-loop system with proportional control for different proportional gains $K = k_d$. (a) Time evolution of the process output y with a setpoint $y_{sp} = 1$. (b) Time evolution of the control action u. The illustration is sourced from [85].

control, Equation 3.1 becomes

$$u_0 = K\left(e_0 + \frac{e_0}{T_i}\,t\right). \tag{3.3}$$

This proves that as long as $e_0 \neq 0$, the control action u_0 cannot be constant.

Figure 3.4 shows the controller output u and the process output y after a step change in the setpoint y_{sp} for different values of integral time $T_i = 1/k_i$. The proportional gain K is set to unity.

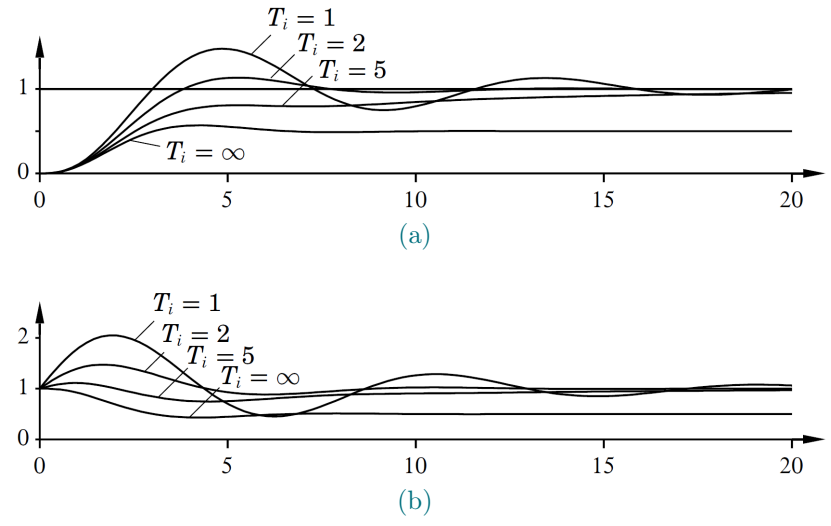

Figure 3.4: Step response of a closed-loop system with PI control for different integral times $T_i = 1/k_i$. (a) Time evolution of the process output y with a setpoint $y_{sp} = 1$. (b) Time evolution of the control action u. The illustration is sourced from [85].

Distinct values of T_i can be compared with the pure proportional controller, i.e., $T_i = \infty$. For finite values of T_i, the steady-state error vanishes. For larger values of T_i, the response slowly

approaches the setpoint. A faster approach and larger oscillations are observed for lower values of T_i.

3.3.3. Derivative action

If a PI control causes excessive oscillations, adding a derivative term, often called an anticipatory term, can help. The derivative action reduces oscillations, stabilizing the closed loop. This instability arises from the delay between changes in the control variable and their effect on the process output.

A simplification is to interpret the action of a controller with proportional and derivative action as making the control proportional to the predicted process output. For a PD control, Equation 3.1 becomes

$$u(t) = K\left(e(t) + T_d \frac{d\,e(t)}{d\,t}\right). \tag{3.4}$$

The control error is proportional to a Taylor series expansion of $e(t + T_d)$. The control error is thus proportional to a linear prediction of the control error at time T_d ahead, as illustrated in Figure 3.5.

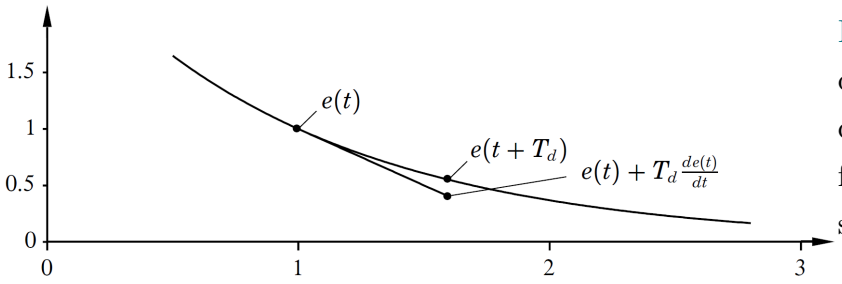

Figure 3.5: Interpretation of derivative action as predictive control using linear extrapolation for prediction. The illustration is sourced from [85].

Figure 3.3 shows the controller output u and the process output y after a step change in the setpoint y_{sp} for different values of derivative time $T_d = k_d$.

Distinct values of T_d can be compared with the pure PI control, i.e., $T_d = 0$. Initially, increasing T_d reduces oscillations, but excessive T_d increases them again. The derivative action improves the transient response by reducing the overshoot and reduces the settling time.

Derivative action is often not used. Many industrial controllers only implement PI control.

3.4. Conclusions

This chapter introduced the two main control system structures: open-loop and closed-loop control. In open-loop control, the system's output is not measured, and the actuating signal is not corrected to match the output with the reference signal. In contrast, closed-loop control incorporates a sensor to measure the output and uses feedback to modify the control variable.

Time-domain specifications were introduced to characterize the step response in the control

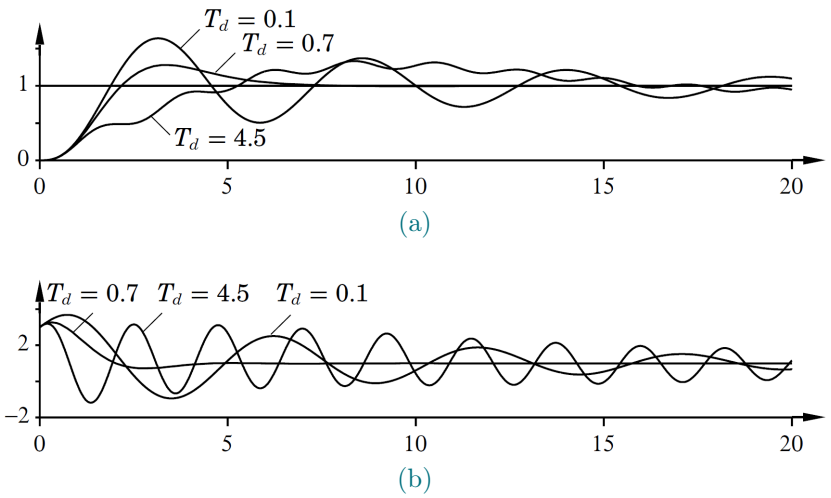

Figure 3.6: Step response of a closed-loop system with PID control for different derivative times $T_d = k_d$. (a) Time evolution of the process output y with a setpoint $y_{sp} = 1$. (b) Time evolution of the control action u. The illustration is sourced from [85].

design. The chapter concluded with a discussion on the Proportional-Integral-Derivative (PID) control and the effect of each term. The proportional term reduces rise time, the integral term eliminates steady-state error, and the derivative term improves transient response.

Although methods for automatically tuning PID gains exist, the complexity of the systems considered in the following sections makes these methods inapplicable. Therefore, the controller gains will be set by trial and error, based on the qualitative understanding provided in this chapter.

4 | Description of the ACBC method

Time-invariant nonlinear systems exhibit complex behaviors, including multiple branches of orbits interconnected by bifurcations (see Chapter 2). These systems are typically characterized theoretically using advanced numerical continuation techniques [22, 37, 67]. For nonlinear mechanical systems vibrating under external force, numerical continuation computes steady-state behavior through frequency response curves (FRCs) [50].

Identifying FRCs for nonlinear mechanical systems experimentally is challenging with traditional excitation signals like swept or stepped sines. The same excitation signal can yield different responses based on the initial state (folding), and perturbations can cause the system to jump between periodic orbits. Near bifurcations, the shrinking basin of attraction may cause jumps before reaching resonance, leaving resonances unidentified. Additionally, periodic orbits can be unstable, making them unobservable in practice. [3]

New approaches have been developed to test nonlinear structures more systematically and reliably. Control-based nonlinear vibration testing (CBNVT) extends numerical continuation to feedback-controlled experiments.

There are two traditional control-based continuations (CBC): derivative-based and mapping-based. Derivative-based continuation involves experimentally calculating derivatives, which is highly inaccurate with noise and requires stopping the experiment. Mapping-based continuation explores a large portion of the response surface, though typically only a segment is needed. Mapping-based methods can be performed online or offline, depending on the continuation procedure.

This chapter introduces a new method for experimental arclength CBC: the online, derivative-less control-based nonlinear vibration testing (ACBC), developed by Gaëtan Abeloos [1, 2]. The chapter begins by illustrating the folding phenomenon in open-loop experiments and explaining the principle of control-based experiments. The classical offline CBC [11] is introduced for unfolding and stabilizing open-loop experiments. The ACBC method, which enhances this approach with adaptive filters and arclength continuation, is also presented.

4.1. Open-loop and control-based experiments

In open-loop testing, the input parameters are excitation amplitude p and frequency ω. The objective is to characterize the response amplitude by varying one parameter while keeping the other constant. S-curves are obtained by keeping ω constant, while FRCs are obtained by keeping p constant.

Figure 4.1 shows the FRC and S-curve for an open-loop experiment. The fundamental amplitude of the system response X_1 cannot be directly imposed as it is a measured, not an input parameter. No matter which curve the experimenter aims to identify, ω and p are not the

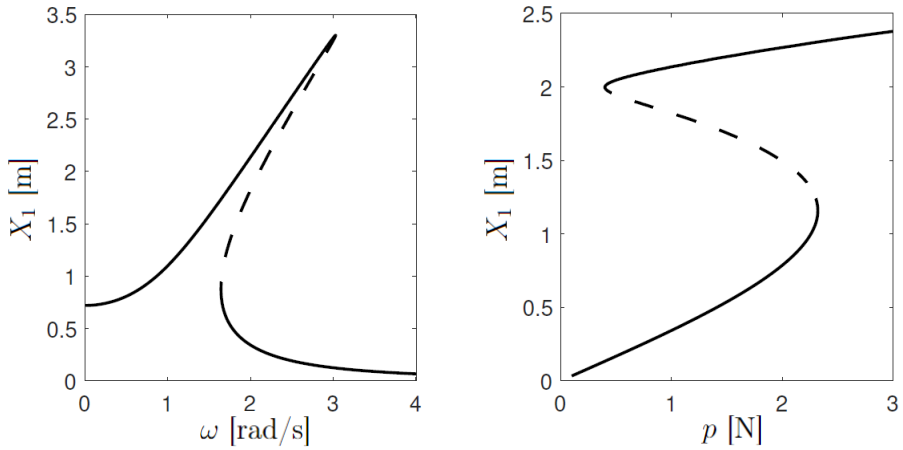

Figure 4.1: (a) FRC at $p = 1$ N and (b) S-curve at $\omega = 2$ rad/s for the Duffing oscillator with $\zeta = 5$ % and other parameters as in Table 2.1. Stable solutions (solid line) and unstable solutions (dashed line) are depicted. The illustrations are sourced from [1].

best parameters for the experiment. Both the FRC and S-curve appear folded. Additionally, unstable solutions cannot be observed in open-loop experiments because any perturbation will cause the system to deviate.

The identification of FRCs of mechanical systems can be done using CBC. It extends the numerical continuation principle to a feedback-controlled experiment. The two parts are explained here below.

Figure 4.2 represents the control-based experiment, which ensures the stabilization of any orbit. A feedback loop is used to indirectly impose X_1 by defining a new input parameter, the amplitude of a reference displacement x^*. In the considered version of CBC [11], the controller provides the excitation of the structure. Unlike traditional feedback control, the control-based experiment does not aim to make the response x converge to the reference x^*. Instead, it adjusts the reference signal until a specific controller output is achieved, exciting the structure as desired. The control action is defined as $u = g(x^* - x)$ where $g(\cdot)$ describes the controller's

dynamics.

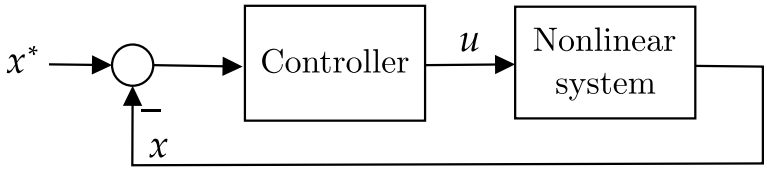

Figure 4.2: Block diagram of control-based experiment.

The stabilized orbit corresponds to the sought orbit if the controller is non-invasive, i.e. if its output u corresponds to monoharmonic forcing when the system lies on the orbit. In a linear system with initially monoharmonic control action, the response is monoharmonic at the excitation frequency. Imposing a monoharmonic reference ensures the control action continues to be monoharmonic.

Because a nonlinear system responds at different frequencies under monoharmonic forcing, its displacement can be decomposed into fundamental and non-fundamental harmonic components, i.e. $x(t) = x_{\mathrm{f}}(t) + x_{\mathrm{nf}}(t)$. The reference displacement x^* can also be decomposed into fundamental and non-fundamental harmonic components, i.e. $x^*(t) = x^*_{\mathrm{f}}(t) + x^*_{\mathrm{nf}}(t)$. These two multi-harmonic displacements are fed in the controller which synthetizes $u(t) = u_{\mathrm{f}}(t) + u_{\mathrm{nf}}(t)$. Non-invasiveness is achieved when $u_{\mathrm{nf}}(t) = 0$, i.e. the control output $u(t) = u_{\mathrm{f}}(t)$ is a harmonic excitation applied to the system.

Once the desired orbit is identified, the continuation process smoothly transitions from one orbit to another. The reference is adjusted, and the control-based experiment stabilizes a new periodic orbit in the open-loop experiment.

4.2. Offline control-based continuation

This section uses the traditional implementation of CBC [11], applied in several studies [42, 61, 62, 64]. It assumes that different solutions rarely share the same fundamental amplitude X_1 at a specific excitation frequency. Imposing X_1 would lead to a unique response, provided X_1 increases monotonously for a fixed forcing frequency. This means fundamental S-curves are monotonous and fundamental FRCs do not intersect. Based on this key assumption about S-curves, X_1 can be sequentially increased to identify S-curves, and FRCs can be indirectly approximated. X_1 is imposed through a control-based experiment.

This CBC is termed offline CBC because it cancels invasiveness and performs continuation by stopping the experiment for offline iterations.

The excitation of the structure can be generated by a derivative controller whose input is the

difference between the reference displacement x^* and the measured displacement x:

$$u(t) = k_d \frac{\mathrm{d}}{\mathrm{d}t}\big(x^*(t) - x(t)\big) \tag{4.1}$$

CBC can use any control law. The user-defined gain determines the experiment's dynamics, modifying the system's response to perturbations and stabilizing unstable orbits (see [13] and [1]).

At steady state, the system displacement x, the displacement reference x^*, and the control action u can be approximated with truncated Fourier series of N harmonics:

$$\begin{aligned} x(t) &= \sum_{n=1}^{N} s_{x,n} \sin(n\,\omega\,t) + c_{x,n} \cos(n\,\omega\,t) \\ x^*(t) &= \sum_{n=1}^{N} s_{x^*,n} \sin(n\,\omega\,t) + c_{x^*,n} \cos(n\,\omega\,t) \\ u(t) &= \sum_{n=1}^{N} s_{u,n} \sin(n\,\omega\,t) + c_{u,n} \cos(n\,\omega\,t) \end{aligned} \tag{4.2}$$

The fundamental and non-fundamental component for each signal respectively corresponds to $n = 1$ and $n \in [2; N]$.

The controller is invasive if the excitation of the structure is multi-harmonic. The system follows a periodic orbit that is not the result of classical open-loop tests. Monoharmonic forcing is achieved by adjusting the reference x^*_{nf} until it is matches to x_{nf}, i.e. by setting the non-fundamental Fourier coefficients of x^*_{nf} equal to those of x_{nf}

$$(s_{x^*,n}, c_{x^*,n})_{n=2}^{N} = (s_{x,n}, c_{x,n})_{n=2}^{N}. \tag{4.3}$$

Fixed-point iterations can correct the Fourier coefficients of the reference signal. The update can be performed offline using derivative-free Picard iterations, as detailed below. Once non-invasiveness is achieved, the fundamental components of the system displacement x_{f} and reference displacement x^*_{f} generate the fundamental excitation applied to the system.

Using Picard iterations in the control-based experiment, one point on the S-curves can be stabilized. This procedure is illustrated in Figure 4.3.

The fundamental phase of the reference x^*_{f} does not affect the response, as a time-invariant oscillator allows any phase difference to be removed by a time shift. The fundamental component of the reference is chosen as $x^*_{\mathrm{f}} = X^*_1 \sin(\omega\,t)$. The controlled experiment has only two input parameters: the reference frequency ω and amplitude $X^*_1 = \sqrt{(s_{x^*,1})^2 + (c_{x^*,1})^2}$. The amplitude of the force p is replaced by the fundamental amplitude of the reference X^*_1.

To identify one S-curve point, the excitation frequency ω and fundamental amplitude of the

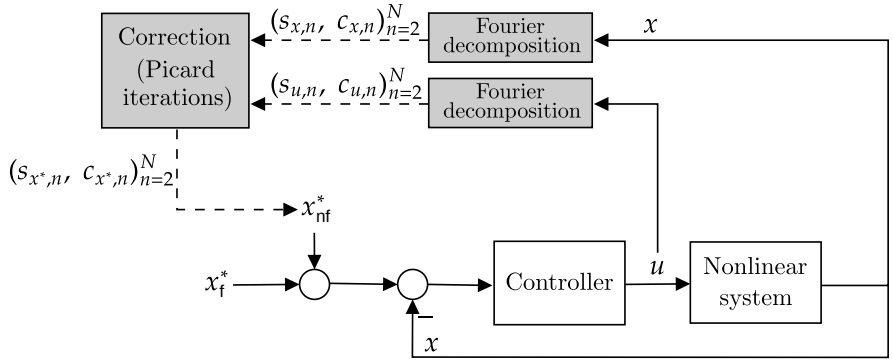

Figure 4.3: Control-based algorithm for one S-curve point identification. The grey boxes represent offline steps.

reference displacement X_1^* are set to a constant. The continuation procedure determines the fundamental amplitude.

The feedback loop must run continuously to maintain system stability. The correction step for non-invasiveness, performed at steady state, is done offline.

The corrective iterations involve the following steps. Once the controlled system reaches a steady state, the time series of x and u are recorded over one period. Fourier decomposition of u and x is then performed using the direct Fourier transform. The non-fundamental Fourier coefficients of x are copied into the corresponding coefficients of x^*. These steps are repeated until the non-fundamental Fourier coefficients of the control action u fall below a specified tolerance, i.e., $\max_n\left((|s_{u,n}|, |c_{u,n}|)_{n=2}^{N}\right) < \mathrm{tol}$. The corrective iterations do not modify the fundamental Fourier coefficients of the reference $s_{x^*,1}$ and $c_{x^*,1}$.

The continuation process moves smoothly from the previously found periodic orbit to another. Figure 4.4 represents the complete block diagram of the offline CBC.

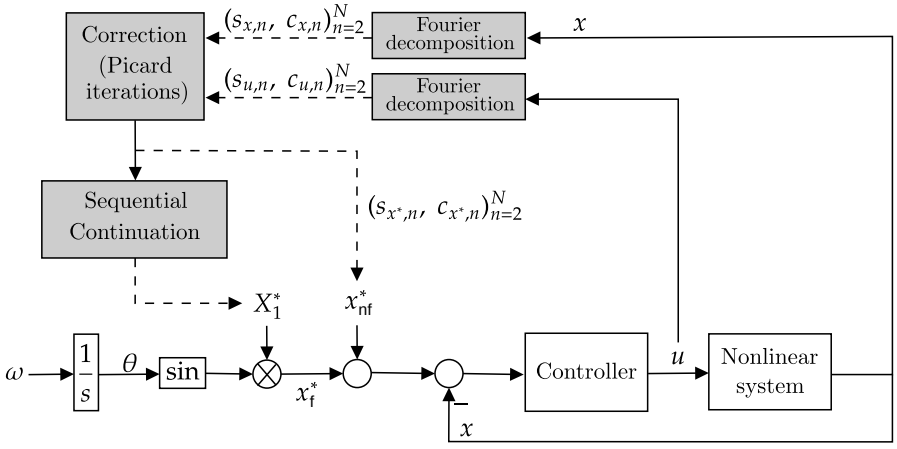

Figure 4.4: Offline CBC algorithm for S-curve identification. The grey boxes represent the offline steps.

With sufficiently high derivative gain, the S-curves are unfolded, allowing the use of a simple sequential continuation scheme, as illustrated in Figure 4.5. To find a new periodic solution on the S-curve, the fundamental amplitude X_1^* is incremented by a step h, i.e., $X_1^* \leftarrow X_1^* + h$. This step continuation is performed offline.

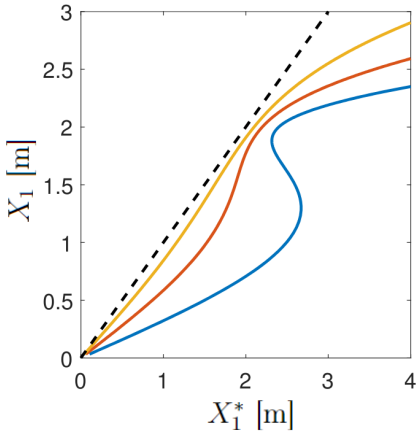

Figure 4.5: S-curves at $\omega = 2$ rad/s with $\zeta = 5$ % and other parameters as in Table 2.1, $k_d = 0.5$ (blue), 1 (orange), and 2 (yellow). The illustration is sourced from [1].

Once the continuation identifies a complete S-curve for a specific frequency, it is repeated for different frequencies. Each continuation process begins by initializing the Fourier coefficients of x^* to create a monoharmonic signal with a small amplitude and constant frequency. The collection of S-curves forms the dynamic response surface, and the FRC can be approximated by slicing at a constant forcing amplitude. This CBC is a mapping-based continuation.

The main drawbacks of this method are offline computations and the assumption that S-curves can always be unfolded with high derivative gain. This is not always true, especially with superharmonic resonances of the Duffing oscillator [1]. Additionally, it identifies a large portion of the response surface when only a segment is needed for FRC identification.

4.3. Adaptive filters

Fourier decomposition can be performed using discrete Fourier transform (DFT), synchronous demodulation, and adaptive filters. Offline methods, such as DFT, compute coefficients after collecting data over several periods and operate in parallel to the experiment. Online methods, including synchronous demodulation and adaptive filters, update coefficients at each sample time, matching the controller's frequency. Reference [1] highlighted the advantages of adaptive filtering over conventional synchronous demodulation with low-pass filters.

The key idea of this section is to impose non-invasiveness (Equation 4.3) online. Figure 4.6 presents the updated block diagram of the CBC.

The offline estimation and correction of the Fourier coefficients of x_{nf}^* is removed. Instead, x_{nf}^* is synthesized by online estimation of Fourier coefficients of x using adaptive notch filters. This

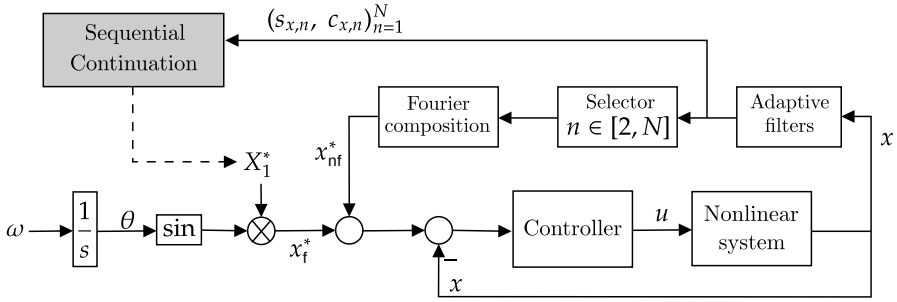

Figure 4.6: CBC algorithm with adaptive filters for S-curve identification. Only the sequential continuation is performed offline.

makes control-based experiments simpler and faster.

Identifying a periodic solution on the S-curve can continously run through time. The continuation over the S-curve is still performed offline. An online continuation of the S-curve was proposed in [3].

Adaptive notch filters isolate or remove specific frequency components from the input signal $x(t)$. In the CBC, instead of using the usual filter outputs, the Fourier coefficients of the targeted component are directly accessed.

The truncated Fourier expansion of $x(t)$ with N harmonics is given by

$$\begin{aligned} x(t) &= \frac{c_0}{\sqrt{2}} + \sum_{n=1}^{N} s_n \sin(n\,\omega\,t) + c_n \cos(n\,\omega\,t) \\ &= \mathbf{Q}(t)\,\mathbf{z}^T \end{aligned} \tag{4.4}$$

where $\mathbf{Q}$(t) is a basis composed of harmonic signals

$$\mathbf{Q}(t) = \left[\frac{1}{\sqrt{2}}\ \sin(\omega\,t)\ \cos(\omega\,t)\ \cdots\ \sin(N\,\omega\,t)\ \cos(N\,\omega\,t)\right], \tag{4.5}$$

and $\mathbf{z}$ contains the Fourier coefficients of $x(t)$

$$\mathbf{z} = \left[c_0\ s_1\ c_1\ \cdots\ s_N\ c_N.\right] \tag{4.6}$$

An adaptive filter synthesizes the signal $\hat{x}$ by applying a time-varying linear combination of the basis $\mathbf{Q}$. The approximation of the measured signal $x(t)$ is

$$\hat{x}(t) = \mathbf{Q}(t)\,\mathbf{w}^T(t) \approx x(t) \tag{4.7}$$

where the weight coefficients are

$$\mathbf{w} = \Big[w_0(t)\ w_{1,s}(t)\ w_{1,c}(t)\ \cdots\ w_{N,s}(t)\ w_{N,c}(t).\Big] \tag{4.8}$$

The weights are updated online using the least mean squares (LMS) algorithm, which is simple and cost-effective [3]. The synthesis error, $e(t) = x(t) - \hat{x}(t) = x(t) - \mathbf{Q}(t)\,\mathbf{w}^T(t)$, is the difference between the measured signal and its approximation. The weights are updated after each time step t_s based on the gradient of the mean squared error:

$$\mathbf{w}(t + t_s) = \mathbf{w}(t) + \mu\,\mathbf{Q}(t)\,e(t), \tag{4.9}$$

where μ is the step size factor. A small μ ensures smooth, slow convergence, while a large μ leads to fast convergence with large oscillations, similar to PID control behavior (see Chapter 3). An illustration is provided in Appendix B of [1]. For more information on adaptive filters, readers can refer to [32].

When the synthesis error e is nearly zero and the weights $\mathbf{w}$ are almost constant, Equation 4.7 becomes similar to a Fourier decomposition of x. In this situation, the elements of $\mathbf{w}$, can be viewed as an approximation of the Fourier coefficients, $\mathbf{w} \approx \mathbf{z}$.

4.4. Arclength continuation

This section presents the experimental arclength continuation method proposed by Abeloos [1]. Figure 4.7 shows the block diagram combining arclength continuation with the control-based experiment and adaptive filters. The input for the continuation is the fundamental force amplitude, denoted as $p = \sqrt{(s_{p,1})^2 + (c_{p,1})^2}$ in the following. The method is performed online and does not require derivatives.

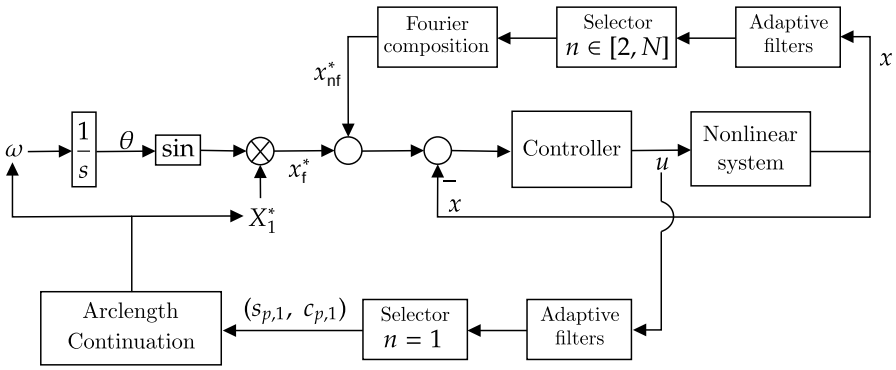

Figure 4.7: Arclength CBC algorithm with adaptive filters for FRC identification (ACBC method), with all steps performed online.

The algorithm is conceptually simple. Figure 4.8 illustrates the basic idea of the arclength continuation, which aims to continue the FRC curve even when it folds.

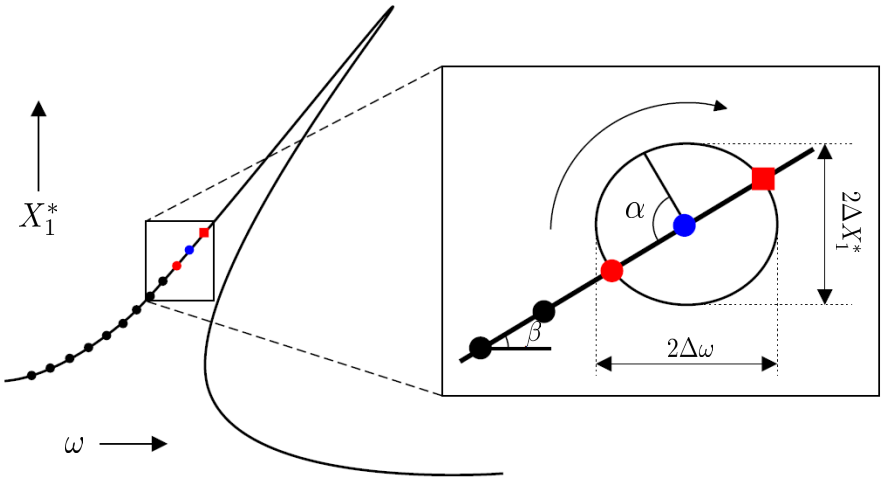

Figure 4.8: Illustration of the arclength continuation method proposed in [1, 2]. Circles represent previously identified responses, the square indicates the next response, the blue point marks the center of the ellipse, and red points highlight responses intersecting the ellipse along the arc.

Distinct solutions rarely exhibit identical fundamental amplitudes at a specific excitation frequency. The sought FRC (in black) is essentially one-dimensional in the fundamental amplitude X_1 versus excitation frequency ω plane. By knowing two solutions of the FRC (red and blue circles), a small ellipse can be drawn around the last identified periodic solution (blue circle). The ellipse intersects the FRC twice: the first intersection (red circle) is the previously identified point, while the second intersection (red square) is the next response to be identified on the branch. This latter solution can be found by sweeping along the ellipse, incrementing the arc angle α until the excitation amplitude p enforced by the controller matches the desired excitation amplitude p^*. The newly identified point then serves as the center for the next ellipse, allowing the identification of the subsequent point on the FRC.

The continuation procedure is outlined in Algorithm 4.1. Two previous solutions of the FRC are needed to determine the next one. The current response, $(\omega_c,\, X^*_{1,c})$, is the center of the ellipse, while the previous solution, $(\omega_p,\, X^*_{1,p})$, lies on the ellipse. The slope of the FRC is approximated by the angle β derived from these responses. The ellipse is defined by its semi-major axes $\Delta\omega$ and ΔX_1^*. Sweeping along the ellipse involves incrementing the angle α, adjusting the input of the CBC experiment $(\omega,\, X_1^*)$. The sweep continues until the next solution is found, i.e., when α reaches a point where p converges to p^* within a specified tolerance tol_p. The sweep must start from an initial arc angle, α_0, to ensure adequate separation from previously identified responses and to prevent identifying an already known point.

The continuation is performed online using adaptive filters and relies on transient responses. By sweeping slowly, it is assumed that the transient response approximates the steady-state response. Transients result from sudden changes in CBC's input parameters. To dampen these

Algorithm 4.1 Arclength continuation for CBC experiment [1].

1: $(\omega_p, X^*_{1,p})$ and $(\omega_c, X^*_{1,c})$ defined by user
2: **loop**
3: $\alpha \leftarrow \alpha_0$
4: $\beta \leftarrow \text{atan2}(X^*_{1,c} - X^*_{1,p}, \omega_c - \omega_p)$
5: $(\omega, X^*_1) = (\omega_c + \Delta\omega \cos(\beta + \pi - \alpha), X^*_{1,c} + \Delta X^*_1 \sin(\beta + \pi - \alpha))$
6: Wait duration t_{cooldown} for steady-state
7: **while** $|p - p^*| > \text{tol}_p$ **do**
8: Modify α with chosen sweeping strategy while maintaining the equality in step 5 continuously
9: **end while**
10: $(\omega_p, X^*_{1,p}) \leftarrow (\omega_c, X^*_{1,c})$
11: $(\omega_c, X^*_{1,c}) \leftarrow (\omega_1, X^*_1)$
12: **end loop**

transients, a cooldown period t_{cooldown} is recommended before starting the sweep. Transients most significantly affect accuracy in resonance regions.

This arclength continuation identifies the responses at the desired harmonic forcing while excluding the continuation arcs from the exported data. This method is similar to the mapping-based continuation approach, particularly the one used in [64], which creates a local map of the response surface near branches of interest.

4.4.1. Arclength strategies

Three strategies are proposed in [1] for the sweep of the arc angle along the ellipse.

Figure 4.9 illustrates the time evolution of the arc angle α and the force amplitude p for the first sweeping strategy. This strategy involves sweeping at a constant angle rate $\dot{\alpha} = \eta_\alpha$ until the targeted excitation amplitude p^* is reached within a specified tolerance. The sweep concludes once this tolerance criterion is met. At the end of the sweep, the system is not in a steady state due to transients in both the system response and adaptive filters.

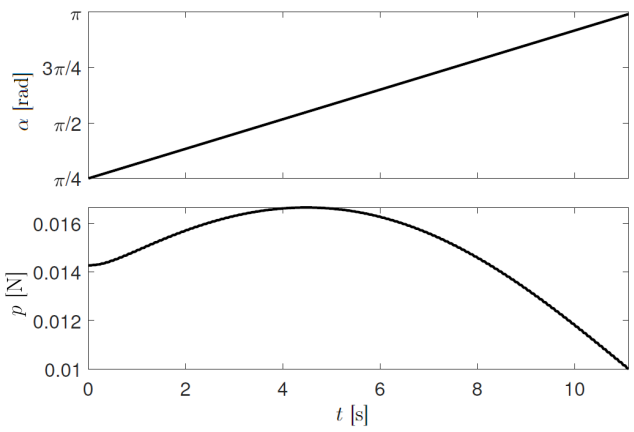

Figure 4.9: Time evolution of the arc angle α and the force amplitude p during the first sweeping strategy of the arclength continuation, as proposed in [1].

Figure 4.10 illustrates the time evolution of the arc angle α and the force amplitude p for the

second sweeping strategy.

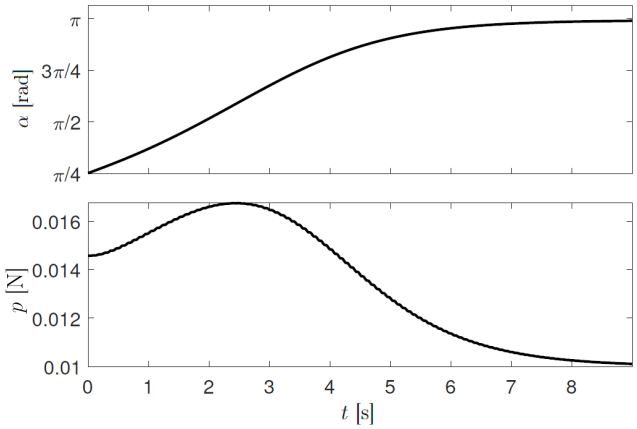

Figure 4.10: Time evolution of the arc angle α and the force amplitude p during the second sweeping strategy of the arclength continuation, as proposed in [1].

This strategy uses an integral controller for sweeping the arc angle. The integral control law is expressed as $\dot{\alpha} = k_i(p - p^*)$ using the force amplitude error as input. Integral gain is chosen to eliminate steady-state error (see Chapter 3). While differential or proportional controllers could adjust overshoot or settling time, no controller is optimal across the entire frequency spectrum. Only integral control is used for simplicity, focusing on tuning a single parameter. The control ensures smooth convergence of the arc angle to its target, reducing transient effects before the stop criterion is met.

Figure 4.11 illustrates the time evolution of the arc angle α and the force amplitude f for the third sweeping strategy.

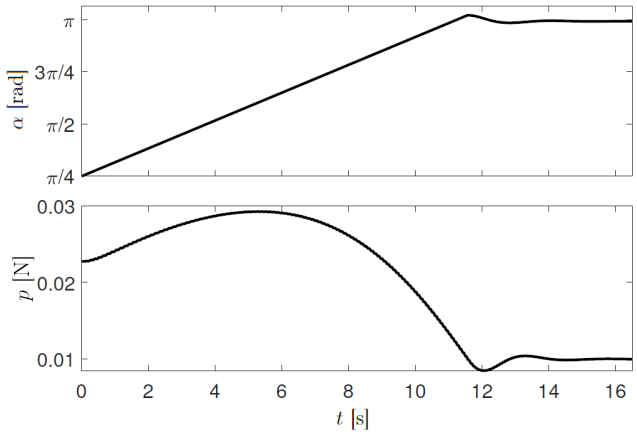

Figure 4.11: Time evolution of the arc angle α and the force amplitude p during the third sweeping strategy of the arclength continuation, as proposed in [1].

This third strategy combines elements of the previous two. It starts by sweeping at a constant arc angle rate until reaching the target excitation amplitude p^*. Then, it switches to the integral controller for gradual convergence to p^* over a predefined time t_{conv}. This method introduces three parameters ($\dot{\alpha}$, k_i, t_{conv}), whereas the previous methods each introduced only one parameter (either $\dot{\alpha}$ or k_i).

4.5. Conclusions

Challenges arise when applying classical swept or stepped sine methods to identify the complete frequency response of nonlinear systems under harmonic forcing, including both stable and unstable branches. Control-based continuation (CBC) provides a more systematic and reliable approach for identifying nonlinear frequency responses.

This chapter first introduced the traditional CBC [11], which assumes that S-curves can be unfolded with sufficient control gain. The method uses fixed-point iterations for non-invasiveness cancellation and sequential continuation to identify S-curves. FRCs are approximated indirectly from a collection of S-curves.

Next, the ACBC method was introduced as a novel approach for control-based nonlinear vibration testing. It builds on traditional CBC but performs online non-invasiveness cancellation using adaptive filters, and uses derivative-free arclength continuation to directly identify FRCs. Since the FRC is one-dimensional in the response amplitude/excitation frequency plane, an ellipse can be drawn from two previously identified points to find the next point on the FRC. The three strategies proposed in [1] were illustrated, highlighting the algorithm's conceptual simplicity.

5 | Application of the ACBC method

The arclength control-based continuation (ACBC) was used by Abeloos in [1] to identify the fundamental resonance in various numerical nonlinear systems. These systems included a hardening Duffing oscillator, a softening-hardening Duffing oscillator, a piecewise linear one-degree-of-freedom oscillator, and a three-degree-of-freedom oscillator with cubic nonlinearity. Abeloos also tested the method on an experimental setup with a clamped-clamped thin beam. The method identified an isolated response branch, due to modal coupling, on top of the fundamental resonance.

The chapter begins with an analysis of the impacts of various parameters. Then, the ACBC method is used to identify the complete frequency response, including fundamental, super-, and subharmonic resonances, of the Duffing oscillator from Chapter 2. Challenges in identifying these resonances are highlighted.

Only the sweep strategy using PID control is considered. Unlike the constant sweep rate strategy, the PID strategy provides a smooth approach to the next FRC intersection. Abeloos' third strategy introduces three parameters to be tuned, two more than the PID strategy. To achieve better performance, a proportional-integral control could be considered. For simplicity, only integral control is used in the sweep strategy, i.e., $\dot{\alpha} = k_i(p - p^*)$.

The ACBC method is implemented in Matlab/Simulink (see Appendix A.1). The control-based experiment utilizes a derivative controller for displacement. It works with velocity signals to avoid the need for computing derivatives. The arc sweep is conducted in the plane defined by the fundamental amplitude of velocity, $\dot{X}_1^* = \omega X_1^*$, versus the excitation frequency, ω.

Stability assessment in CBC is a challenge in experimental research [10, 15]. This work aims to identify both stable and unstable open-loop responses. The following figures will not differentiate between stable and unstable solutions.

5.1. Parameter analysis

A forcing amplitude of 0.01 N is used to illustrate parameter influence, considering: the starting sweep angle α_0, ellipse semi-major axes ($\Delta\omega$, $\Delta\dot{X}_1^*$), the integral gain k_i of the sweep rate control law, and adaptive filters' step size factor μ. The estimated force amplitude during the sweep, referring to the estimation of the first harmonic amplitude of the force, will be discussed

based on these parameters. The force is assumed to be made non-invasive by the control-based continuation.

Figure 5.1 shows the FRC at 0.01 N identified using the ACBC method. Figure 5.1b illustrates the path followed in the input parameter space, i.e., the first amplitude/excitation frequency plane where the ellipses are drawn. This plane is referred to as the sweeping plane in the following discussion. The parameters used are summarized in Table 5.1. The identification process starts at low frequencies and sweeps towards higher frequencies.

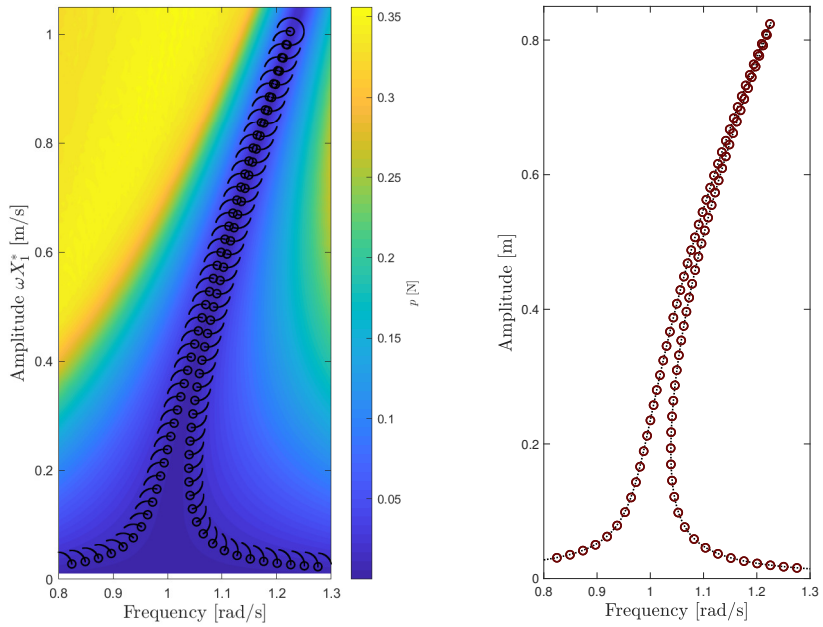

(a) (b)

Figure 5.1: ACBC method applied to the Duffing oscillator's fundamental resonance. (a) Sweeping plane. Arcs indicate the path followed during the sweep, black circles denote accepted points. The contour is obtained with HB continuation. (b) FRC amplitude at $p = 0.01$ N. Red circles denote accepted points. The dotted curve represents the results of the HB continuation.

$\Delta\dot{X}_1^*$ [m/s]	$\Delta\omega$ [rad/s]	k_i [rad/(s N)]	k_d [kg/s]	μ [-]	α_0 [rad]
0.025	0.025	0.5	1	0.5 t_s	$\pi/2$

Table 5.1: ACBC simulation parameters for the fundamental resonance of the Duffing oscillator ($p = 0.01$ N).

5.1.1. Initial sweep angle

The initial sweep angle is set to ensure the sweep starts far enough from the previous point, preventing the re-identification of the previous point instead of the next one.

Figure 5.2 illustrates the continuation for two distinct values of starting sweep angles ($\alpha_0 = \pi/2$ and $\alpha_0 = \pi$). The choice of the starting sweep angle can accelerate computation. The most appropriate value is $\alpha_0 = \pi$, as it begins the search along the secant of the two previously identified solutions. As the ellipse size is reduced, the next point is likely to be close to $\alpha = \pi$. This is illustrated in Figure 5.2b, where only a very small arc of each ellipse is swept because

the first estimate is close to the next solution, except at the resonance peak. In the following, the initial sweep angle is set to π.

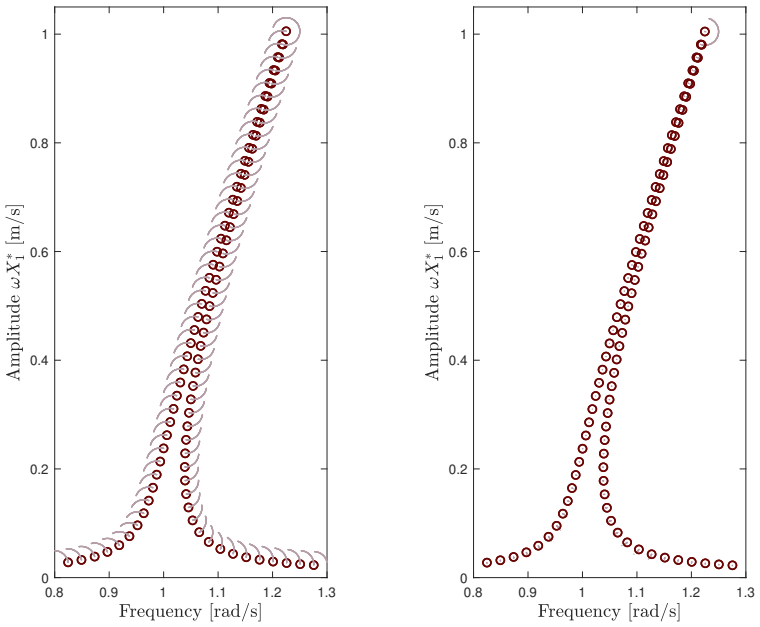

(a) (b)

Figure 5.2: Sweeping plane for the ACBC method with distinct starting sweep angles: (a) $\alpha_0 = \pi/2$ and (b) $\alpha_0 = \pi$. Purple arcs indicate the sweep and red circles denote accepted points.

The initial sweep angle determines if the sweep occurs inside or outside the FRC. As illustrated in Figure 5.1a, sweeping outside the FRC explores higher forcing levels, while sweeping inside explores lower levels, making it better for experiments. Starting the sweep outside the FRC ensures the identification continues on the same branch.

5.1.2. Sweep rate

The integral controller regulates the arc angle, which is associated with the force level of the intersected FRC. Ideally, the sweep should wait for a steady state after each arc angle change to ensure the force meets the desired tolerance accurately. This is highly computationally expensive. Instead, the sweep angle is continuously changed at a slow rate to keep transients small and the estimated force close to steady state. The FRC accuracy depends on the transients' amplitude in the system response and adaptive filters. The sweep rate is influenced by both the integral gain and ellipse size.

Figure 5.3 shows the impact of varying the integral gain and semi-major axes on accuracy.

In the integral control law, the sweep rate $\dot{\alpha}$ is proportional to the integral gain k_i. As illustrated in Figure 5.3a, decreasing the integral gain reduces transients and increases accuracy, though it extends the testing time. If the sweep is too fast, transients degrade the accuracy of the identified FRC, and can prevent the estimated force amplitude from reaching the target p^*. In the latter case, the continuation procedure will loop indefinitely and fail to identify the next point.

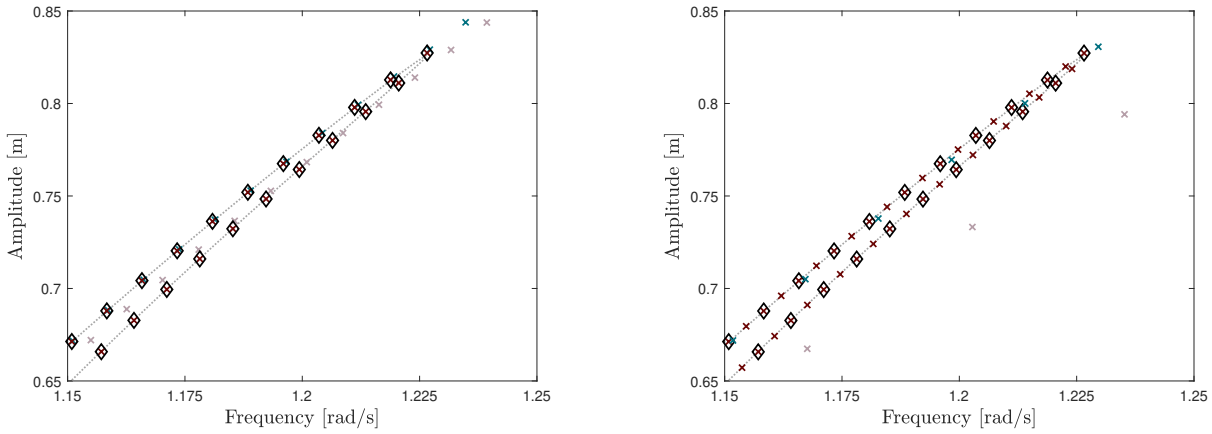

Figure 5.3: Parametric study varying (a) the integral gain $k_i = 0.25$ (×), $k_i = 0.5$ (◊), $k_i = 1$ (×), $k_i = 2$ (×) or (b) the semi-major axes $\Delta\dot{X}_1^* = \Delta\omega = 0.0125$ (×), $\Delta\dot{X}_1^* = \Delta\omega = 0.025$ (◊), $\Delta\dot{X}_1^* = \Delta\omega = 0.05$ (×), $\Delta\dot{X}_1^* = \Delta\omega = 0.1$ (×). The grey dotted curve is the solution obtained with HB continuation.

The same effects observed for a reduced integral gain can be observed for a reduced size of the ellipse, see Figure 5.3b. Reducing the ellipse size allows for the identification of more points and also decreases the magnitude of transients. It also causes the experiment to last much longer.

In Figure 5.3, for integral gains $k_i = 1$ and 2 or step sizes $\Delta\omega = \Delta\dot{X}_1^* = 0.5$ and 0.1, accuracy decreases near the resonance peak. The parameter influence on the sweep rate also depends on the ellipse's location.

The effects of step size, integral gain, and ellipse location are further investigated by observing transients in the estimated force amplitude during the sweep.

Ellipse size

Figure 5.4 shows the evolution of the estimated force amplitude along an ellipse for different ellipse sizes ($\Delta\omega$, $\Delta\dot{X}_1^*$) with a constant sweep rate. The arc angle, denoted as α in Figure 4.8, starts on the upper branch of the fundamental resonance.

Smaller ellipses intersect only the upper branch, as shown in Figure 5.4a for $\Delta\dot{X}_1^* = \Delta\omega = 0.025$ or 0.0125. Starting from a zero arc angle in Figure 5.4b, the sweep is initially outside the targeted fundamental resonance. The ellipse intersects FRCs at higher forcing levels than the targeted 0.01 N, as shown in Figure 5.1a. Around $\alpha = \pi$, the ellipse intersects the targeted FRC, then continues inside the fundamental resonance, intersecting FRCs at lower forcing levels, until returning to the starting point at an arc angle $\alpha = 2\pi$.

Larger ellipses, such as $\Delta\dot{X}_1^* = \Delta\omega = 0.05$, intersect both the upper and lower branches. After

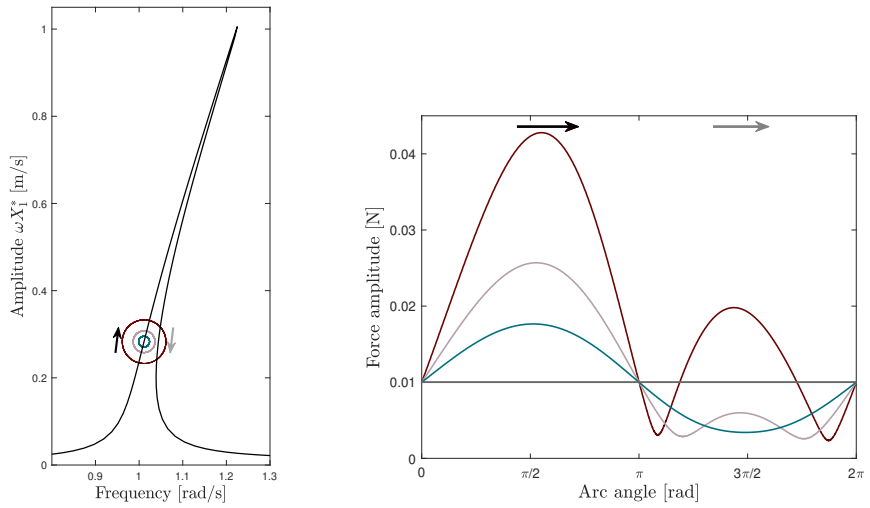

(a) (b)

Figure 5.4: (a) Sweeping plane for the fundamental resonance of the Duffing oscillator ($p = 0.01$ N). (b) Variation in force amplitude along an ellipse for various ellipse size: $\Delta\dot{X}_1^* = \Delta\omega = 0.0125$ (—), $\Delta\dot{X}_1^* = \Delta\omega = 0.025$ (—), $\Delta\dot{X}_1^* = \Delta\omega = 0.05$ (—).

intersecting the targeted FRC around $\alpha = \pi$, the ellipse encounters varying force levels due to intersecting two FRC solutions on the unstable branch. Following $\alpha = \pi$, the sweep starts inside the targeted FRC, reaches the first unstable branch intersection, continues outside to the second intersection, and then finishes inside the targeted FRC, returning to the starting angle $\alpha = 0$.

In Figure 5.4b, larger ellipses intersect FRCs at higher forcing amplitudes, resulting in a steeper slope of the estimated force versus arc angle at the desired FRC intersections. This requires a slower sweep rate or lower integral gain.

Increasing the ellipse size can be unfeasible in practice due to high forcing levels during the sweep, which could exceed shaker limitations or compromise structural integrity.

Integral gain

The sweep rate is proportional to the integral gain in the sweeping strategy.

Figure 5.5 illustrates the evolution of the force amplitude along an ellipse for different values of constant sweep rate $\dot{\alpha}$.

At sufficiently slow sweep rates, the estimated force amplitude at a given arc angle converges, as shown with $\dot{\alpha} = \pi/1250$ or $\pi/6250$ rad/s in Figure 5.5a. If the ellipse is swept too fast, transients degrade the estimated force amplitude, as shown with $\dot{\alpha} = \pi/50$ or $\pi/250$ rad/s in Figure 5.5a. An inappropriate sweep rate results in very inaccurate outcomes or unmet tolerance criteria, causing repeated sweeps.

Proximity to resonance

Figure 5.6 illustrates the evolution of the estimated force amplitude along the same ellipse at distinct locations of the fundamental resonance.

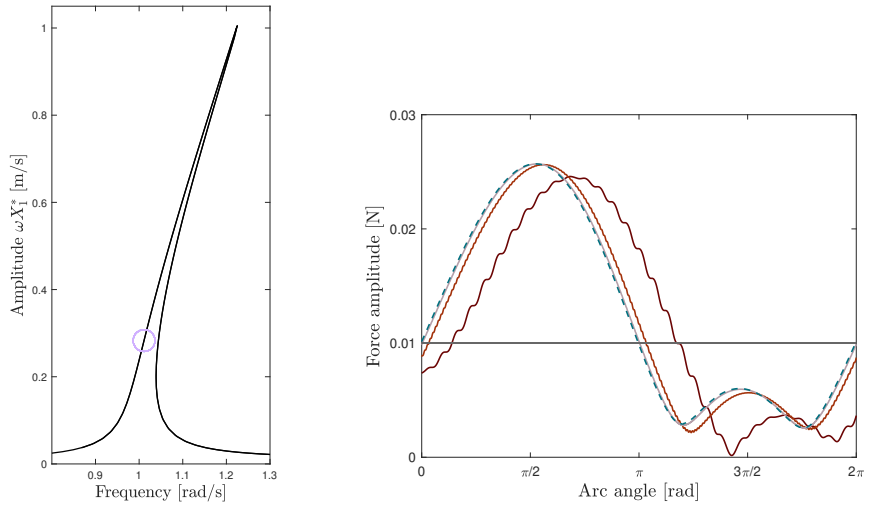

(a) (b)

Figure 5.5: (a) Sweeping plane for the fundamental resonance of the Duffing oscillator ($p = 0.01$ N). (b) Variation in force amplitude along an ellipse for distinct values of sweep rate: $\dot{\alpha} = \pi/50$ rad/s (—), $\dot{\alpha} = \pi/250$ rad/s (—), $\dot{\alpha} = \pi/1250$ rad/s (—), $\dot{\alpha} = \pi/6250$ rad/s (- -).

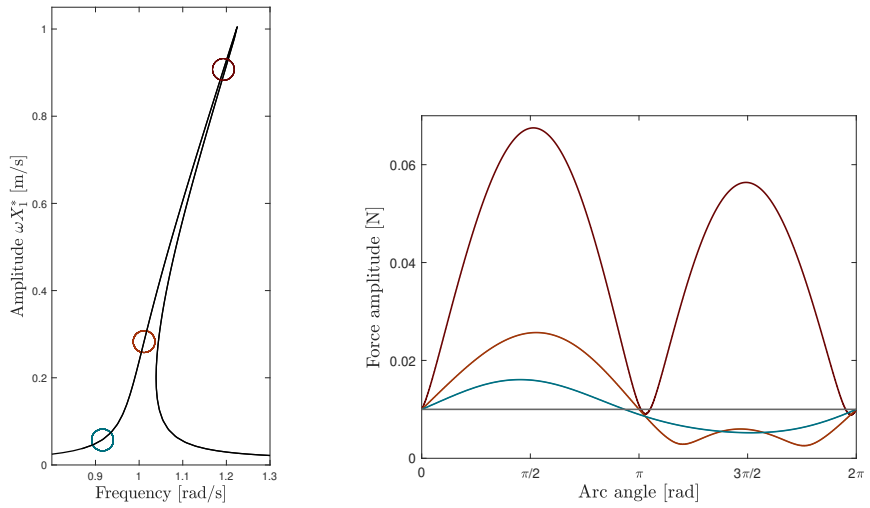

(a) (b)

Figure 5.6: (a) Sweeping plane for the fundamental resonance of the Duffing oscillator ($p = 0.01$ N). (b) Variation in force amplitude with arc angle for three ellipses located at different distances from the peak of the fundamental resonance.

When drawn closer to the fundamental resonance, the ellipse intersects FRCs at higher forcing levels. As shown in Figure 5.1a, FRCs for different forcing levels converge near resonance.

The slope of the force amplitude relative to the arc angle is steeper near the resonance. Since the integral control of the sweep rate is proportional to the estimated force amplitude p, a lower gain is needed near resonance. A sweep rate providing good accuracy far from resonance can introduce errors close to it. No integral gain is optimal for the entire frequency range.

In practice, the same ellipse could not be used both far from and close to resonance if the forcing levels increase significantly during the sweep and become too large for the experiment.

5.1.3. Tolerance criterion

The tolerance criterion immediately stops the sweep when the absolute error between the targeted force p^* and the estimated force p falls below a specified tolerance. This section illustrates the effects of prematurely stopping the integral controller due to this criterion.

Figure 5.7 shows the time evolution of the estimated force during the sweep of two ellipses at different locations. In Figures 5.7b and 5.7c, blue and red indicate the ellipse's location, either far from or close to resonance (see Figure 5.7a).

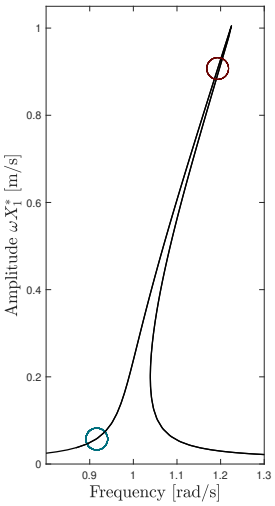

(a)

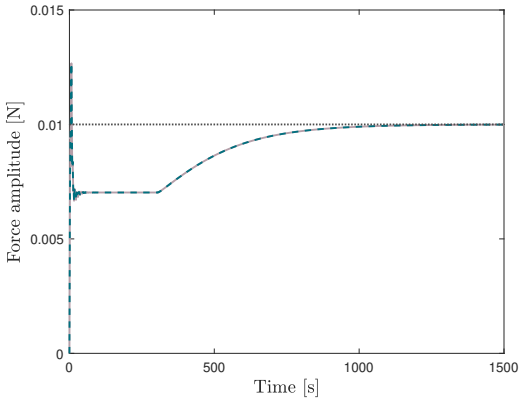

(b)

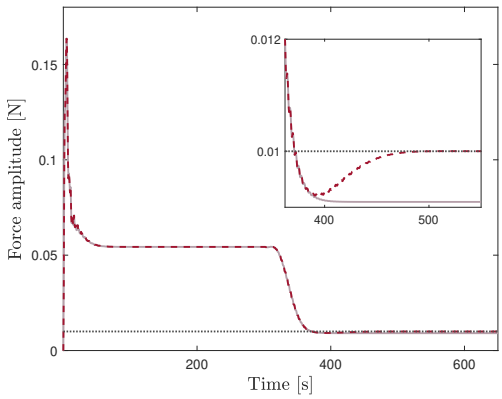

(c)

Figure 5.7: (a) Sweeping plane for the fundamental resonance of the Duffing oscillator ($p = 0.01$ N). (b and c) Time evolution of the estimated force during the sweep with (—) and without (- - or - -) triggering the tolerance criterion. The black dotted line represents the targeted forcing, i.e. 0.01 N. The same parameters are used in both cases.

The purple solid curve shows the time evolution of the estimated force when the sweep stops upon reaching the tolerance criterion. The dotted red and blue curves show the time evolution of the estimated force if the sweep continues, ignoring the tolerance criterion.

When the ellipse is drawn far from the resonance peak (Figure 5.7b), smooth convergence occurs before the tolerance criterion is triggered. Closer to the resonance (Figure 5.7c), the tolerance criterion is met before the integral controller fully converges. If the controller is not stopped, it overshoots and then converges to the targeted force. Premature stopping by the tolerance criterion introduces an error. In the presence of oscillations, the estimated force can reach its target multiple times before reaching a steady state.

Fine-tuning the integral controller is necessary to prevent overshoots and oscillations, which are unsuitable due to the tolerance criterion. This involves using a lower gain, which increases computational time but ensures sufficient accuracy (see Chapter 3).

The presented example had two key points. It proved that the tolerance criterion is applicable for the integral control without overshoot and highlighted that a given integral gain causes overshoot near resonance but not far from it. This aligns with the previous observations about the need for a slower sweep rate close to resonance.

5.1.4. Adaptive filters' step size factor

In the ACBC method, adaptive filters estimate the system response and force (see Chapter 4). The dynamics of adaptive filters depend on the step size factor μ.

Figure 5.8 shows the time evolution of the estimated force amplitude during cooldown. Introduced in Chapter 4, cooldown time dampens transients from sudden changes in CBC input parameters and is applied before each sweep.

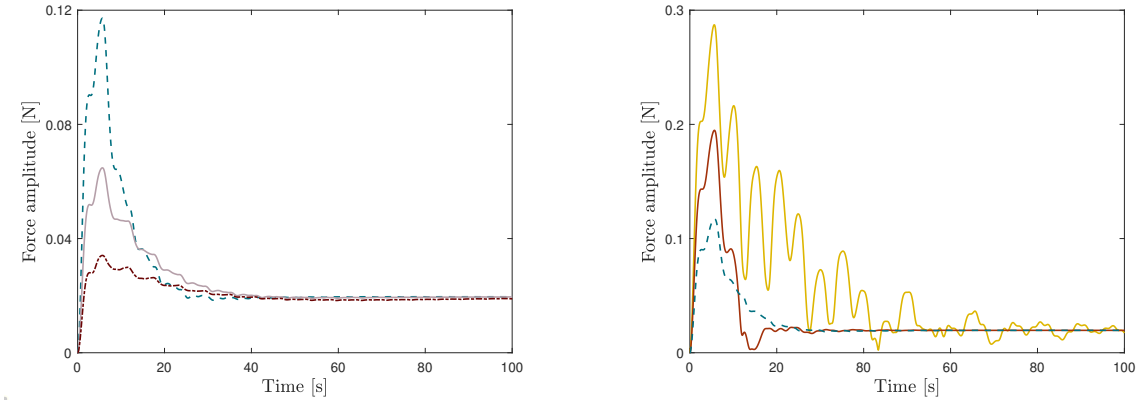

Figure 5.8: Time evolution of the estimated force amplitude during cooldown for different step size factors: (a) $\mu = 0.0625\,t_s$ (—), $\mu = 0.125\,t_s$ (· –), $\mu = 0.25\,t_s$ (– –), and (b) $\mu = 0.25\,t_s$ (– –), $\mu = 0.5\,t_s$ (—), $\mu = 1\,t_s$ (—).

The step size factor dictates the convergence of the adaptive filters' approximation to the signal. Given sufficient time, filters with different step size factors converge to the same estimate. The effect of the step size factor is similar to that of a PID control (see Chapter 3). A smaller μ allows smoother, slower convergence, while a larger μ results in a faster response with greater overshoot and more oscillations. If μ is too large (e.g., $\mu = 1\,t_s$), the oscillations are larger and take longer to dampen. The cooldown needs to be set appropriately for a particular μ.

Figure 5.9a illustrates the influence of the step size factor and cooldown on the accuracy of the identified FRC. Figures 5.9c, 5.9b, and 5.9d compare the time evolution of the force and its amplitude estimation. Vertical dotted lines indicate when the tolerance criterion is met. The sweep always starts after a cooldown.

The solution is accurate for $\mu = 0.5\,t_s$. For $\mu = 1\,t_s$, a too-short cooldown (100 s) is inadequate as the estimation has not converged. The tolerance criterion is triggered immediately after

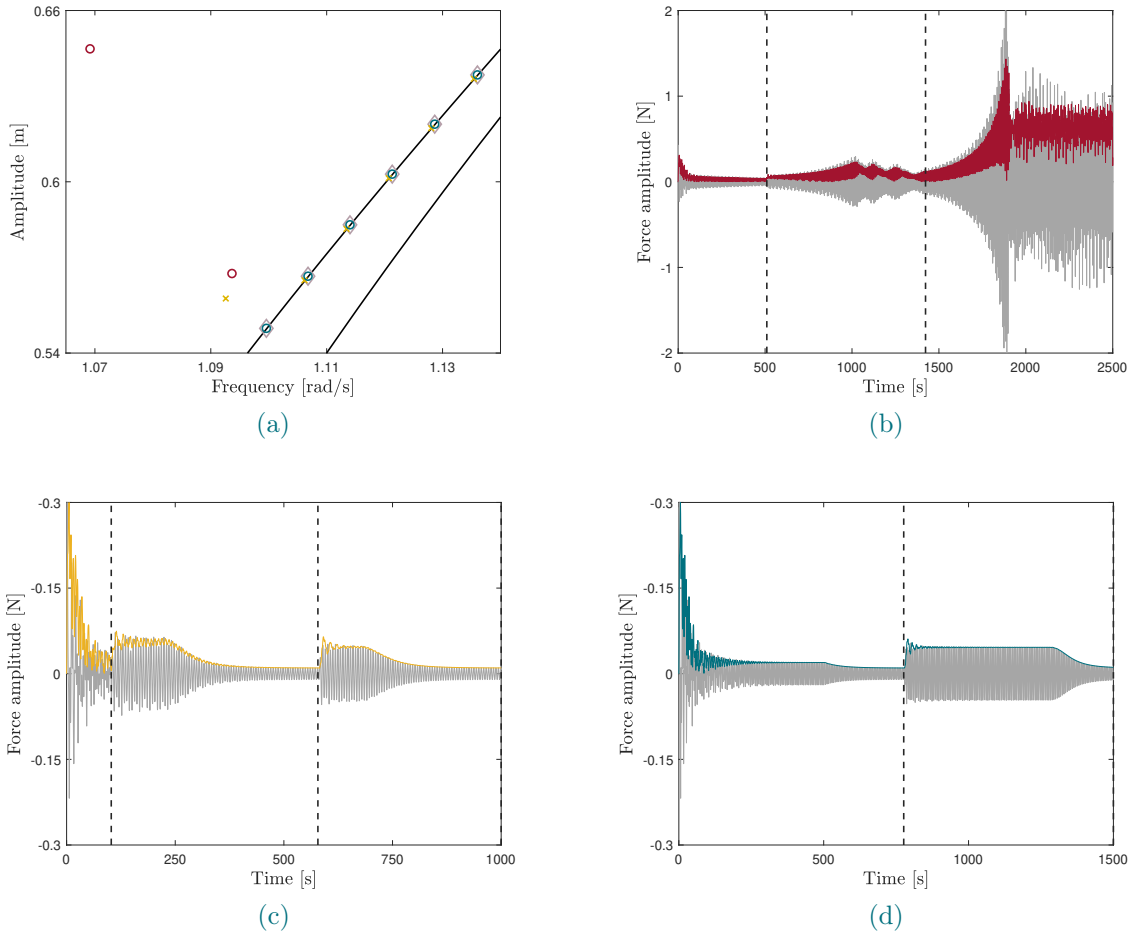

Figure 5.9: (a) Parametric study varying the step size factor and the cooldown duration: $\mu = 0.5\,t_s$ with $t_{\text{cooldown}} = 100$ s (◊), $\mu = 1.1\,t_s$ with $t_{\text{cooldown}} = 100$ s (×), $\mu = 1.1\,t_s$ with $t_{\text{cooldown}} = 500$ s (***o***), $\mu = 1.2\,t_s$ with $t_{\text{cooldown}} = 500$ s (***o***). The black line is identified using HB continuation. (b, c, d) Time evolution of the force (in gray) and its estimated amplitude for three of the cases represented in (a), with colors matching those in (a). Vertical dotted lines indicate when the tolerance criterion is met.

the first cooldown, but the solution is inaccurate due to transients in the filter estimation (see Figures 5.9 and 5.9c). This issue mainly occurs during the first cooldown. For subsequent cooldowns, the ACBC method accurately identifies the next FRC point. Figure 5.9d shows that allowing more time for the first cooldown enables the filters to converge, resulting in better accuracy of the identified FRC solution for the first point. In the example considered, $\mu = 1.1\,t_s$ is already too large as it creates large oscillations and requires a longer cooldown, although the solution can still be identified.

In Figure 5.9b, the step size factor is too large, causing the adaptive filters to poorly approximate the force. The filters destabilize the control-based continuation, preventing the force from becoming non-invasive.

5.1.5. Summary of parameter analysis

To ensure reliable results, all parts of the ACBC method must work effectively. The sweep rate of the arclength continuation should be small enough to avoid introducing large transients. The ellipse size and integral gain influence the sweep rate, and their effects depend on the ellipse's position on the FRC. The step size factor and cooldown time must be set appropriately to ensure the adaptive filters converge.

Generally, a set of constant parameters can be found to work in the frequency region of interest. For better performance, parameters could be adapted based on the ellipse's location.

Several parameters require tuning before applying the ACBC method. Further research could establish practical guidelines applicable in any situation. One potential approach involves using linear modal parameters. Although linear theory is inadequate for nonlinear systems, it can quickly provide rough estimates. For example, the ellipse size could be estimated based on the linear resonance bandwidth.
Additionally, determining a criterion for an optimal sweep rate, considering the combined integral gain and ellipse size parameters, would be advantageous.

5.2. Identification of the fundamental resonance

This section applies the ACBC method to identify the fundamental resonance in the reference case from Chapter 2 and discusses the encountered challenges.

Figure 5.10 shows the identification of the fundamental resonance for the Duffing oscillator at 1N using the ACBC method and HB continuation. The parameters used are listed in Table 5.2.

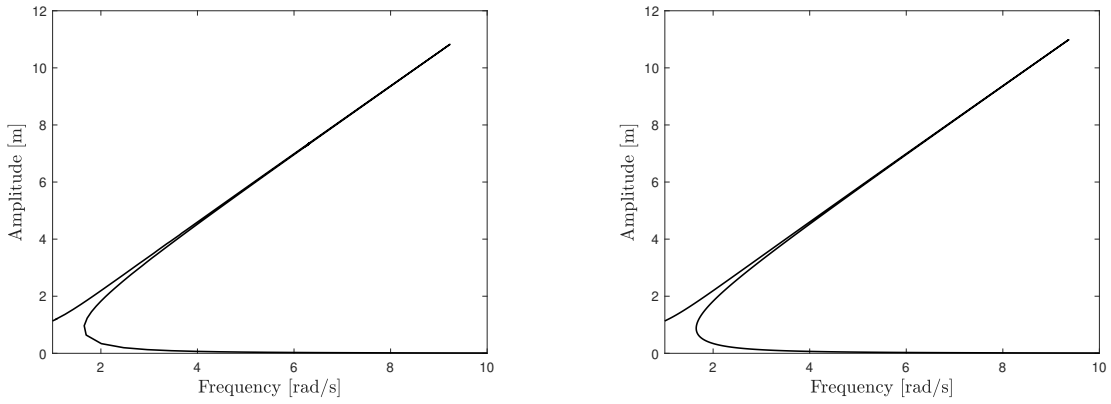

(a) (b)

Figure 5.10: FRC around the fundamental resonance of the Duffing oscillator ($p = 1$ N). (a) ACBC method, (b) Harmonic balance continuation.

$\Delta\dot{X}_1^*$ [m/s]	$\Delta\omega$ [rad/s]	k_i [rad/(s N)]	k_d [kg/s]	μ [-]
0.5	0.5	0.01 (start)	5	0.2 t_s

Table 5.2: ACBC simulation parameters for the fundamental resonance of the Duffing oscillator ($p = 1$ N).

The ACBC method accurately identifies the fundamental resonance, although the resonance reveals an exceptionally narrow peak extending far from the natural frequency. This extreme scenario results from the system's light damping ($\zeta = 0.5\%$) and large forcing amplitude. Identifying the resonance peak posed several challenges, detailed below.

The integral gain, starting at 0.01 as shown in Table 5.2, was kept constant until the sweep became too fast and overlooked the next FRC solution. When this occurred, the integral gain was reduced and kept constant until it became unsuitable again.

Challenges encountered

Maintaining a proper sweep rate with constant ellipse size and integral gain over the large frequency shift of fundamental resonance is challenging. Furthermore, curvature constraints on the ellipse size require sufficient discretization for accurate FRC representation.

Figure 5.11 shows the fundamental resonance in the sweeping plane, illustrating three ellipses in different regions of the resonance curve. The three ellipses are drawn during the identification of the upper branch of the fundamental resonance.

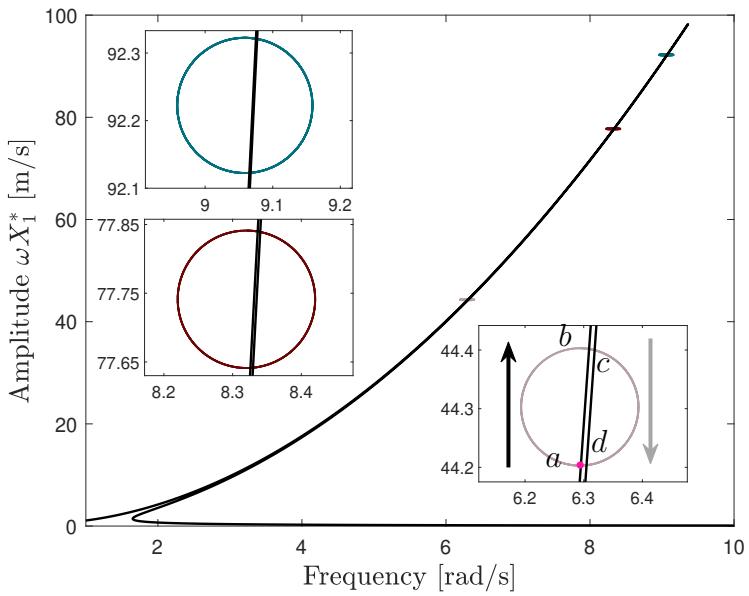

Figure 5.11: Sweeping plane for the fundamental resonance of the Duffing oscillator ($p = 1$ N). Three constant-sized ellipses ($\Delta\dot{X}_1^* = \Delta\omega = 0.1$) are shown on the upper branch of the resonance. The starting point for the purple ellipse is marked in pink. Arrows indicate the sweep direction. The main figure axes are not scaled, while the zoomed-in sections have equally scaled axes.

The resonance is narrow where the ellipses are drawn, intersecting both the upper (stable) and lower (unstable) branches of the fundamental resonance. Near the resonance peak, these

branches converge. Consider the purple ellipse: the sweep starts from a known solution (a) on the upper branch, marked by the pink point in Figure 5.11, and proceeds clockwise. The next intersection with the FRC identifies the next point (b) on the upper branch. Continuing the sweep, the ellipse intersects two points on the lower branch (points c and d).

Figure 5.12 shows the estimated force amplitude along the three ellipses for a constant sweep rate and ellipse size. The desired amplitude of 1N is indicated by a horizontal line.

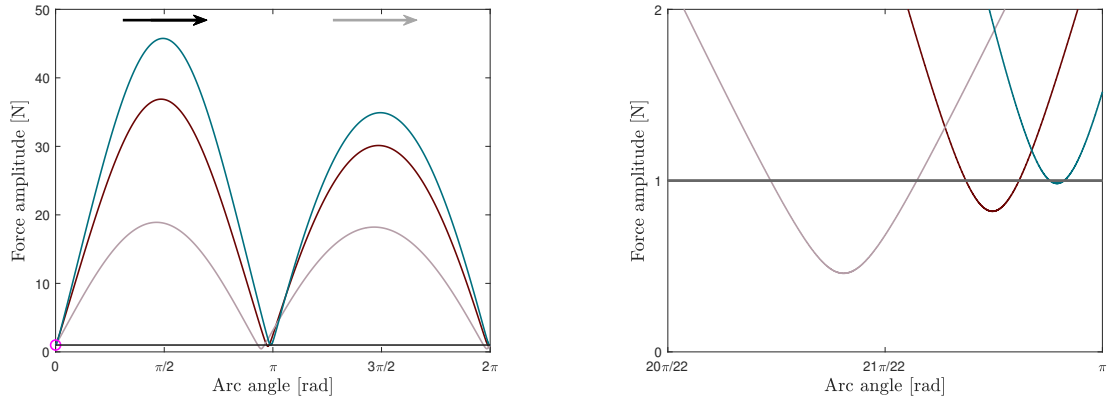

Figure 5.12: (a) Force amplitude variation with arc angle swept at $\pi/10000$ rad/s for three ellipses ($\Delta\dot{X}_1^* = \Delta\omega = 0.1$) at different distances from the fundamental resonance peak. (b) Zoomed view. Curve colors correspond to the ellipse locations in Figure 5.11. The pink circle marks the starting point.

The sweep starts at the pink point (a) at zero arc angle. The ellipse is swept to the next intersection (b), encountering FRCs with increasing forcing levels compared to the 1N reference, as it is outside the fundamental resonance. Further sweeping identifies a third intersection (c), encountering FRCs with lower forcing levels between the branches. Sweeping outside the resonance branches identifies the fourth intersection (d) with higher forcing levels encountered during the sweep. Finally, the ellipse returns to the starting point (a), passing through the resonance and encountering lower forcing levels.

The amplitudes of the estimated forces along the sweep can be compared for the three distinct ellipses. The forcing levels of the intersected FRCs reach magnitudes dozens of times the targeted amplitude, even for the small ellipse considered ($\Delta\omega = 0.1$ while the identification is over 8-9 rad/s), which may be impractical in experiments. Additionally, as one approaches resonance, the spacing between solutions (b to c and d to a) decreases. These observations result in steep force amplitude gradients with respect to the arc angle, complicating the maintenance of small transient magnitudes during the sweep. Near resonance, strong transients require a very small sweep rate or integral gain, while a larger integral gain could be used far from resonance. A too-fast integral gain causes significant transients and potential overshoot in the estimated force, which is unsuitable for the tolerance criterion.

Figure 5.13 shows the variation in force amplitude estimation with different constant sweep rates for the ellipse near resonance in Figure 5.11. A faster sweep rate increases transients and overlooks the solution. The ellipse misses the desired FRC at points (b) and (c). A constant integral gain across this frequency range is impractical for the presented case.

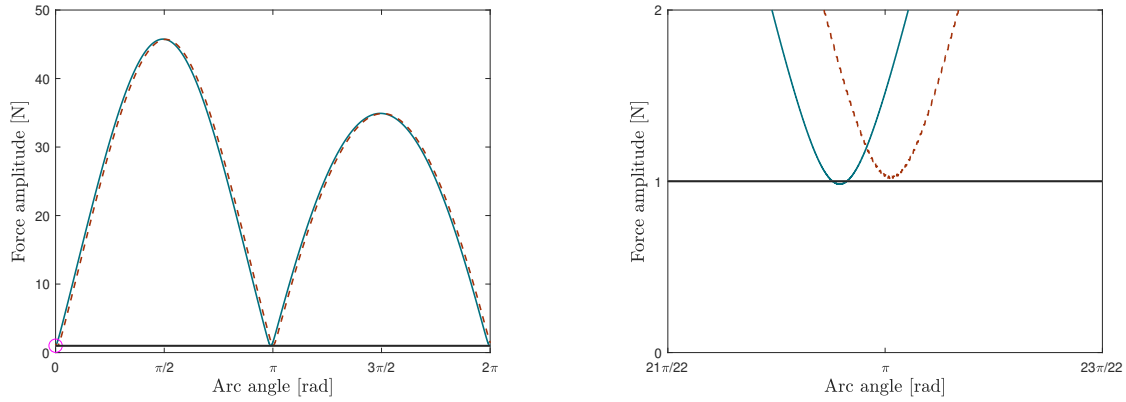

(a) (b)

Figure 5.13: (a) Force amplitude variation with arc angle for the ellipse closer to the resonance peak in Figure 5.11 ($\Delta\dot{X}_1^* = \Delta\omega = 0.1$). (b) Zoomed view. The solid blue line is obtained with $\dot{\alpha} = \pi/10000$ rad/s and the dotted orange line with $\dot{\alpha} = \pi/1000$ rad/s. The pink circle marks the starting point.

The size of the ellipse drives the rate of the sweep and the accurate discretization of FRC. Both necessitate a small ellipse. As the ellipse size is constant for the complete frequency range, a small ellipse requires a lot of computational time. The computational time could be reduced by adjusting the ellipse size based on the curvature, using a larger ellipse size in straighter regions and a smaller size in more curved regions. This solves the problem but it requires adapting the integral gain in consequence. In experiments, the ellipse size could also be limited by the maximum forcing level the shaker can provide or the structure can withstand.

The final comment emphasizes the need for a high sampling frequency. At low forcing levels, non-fundamental harmonics have minimal impact, except near the peak. With high forcing and light damping, nonlinearity amplifies these harmonics, causing a frequency shift from 1 rad/s to 9 rad/s. Thus, a sampling frequency chosen at one point of the curve can be inaccurate near the peak. Low sampling frequency can miss solutions, similar to a rapid sweep. Proper sampling requires slowing computation.

In conclusion, the problems encountered are similar to those noted previously, primarily due to the large frequency shift caused by significant excitation in the lightly damped structure. This extreme case complicates maintaining constant integral gain and ellipse size across the frequency range. For typical fundamental resonance cases, changing the integral gain is unnecessary,

though it becomes not optimal near resonance.

5.3. Identification of secondary resonances

This section applies the ACBC method to identify the super-and subharmonic resonances in the reference case from Chapter 2 and discusses the encountered challenges.

5.3.1. Identification of odd-superharmonic resonances

Figure 5.14 shows the 3 : 1 superharmonic resonance identified using the ACBC algorithm and HB continuation. The parameters for the ACBC algorithm are detailed in Table 5.3. Two continuation runs are performed for the ACBC method. The first, shown in blue in Figure 5.14a, starts from a frequency lower than the 3 : 1 resonance. The second, shown in purple, starts from a frequency higher than the 3 : 1 resonance.

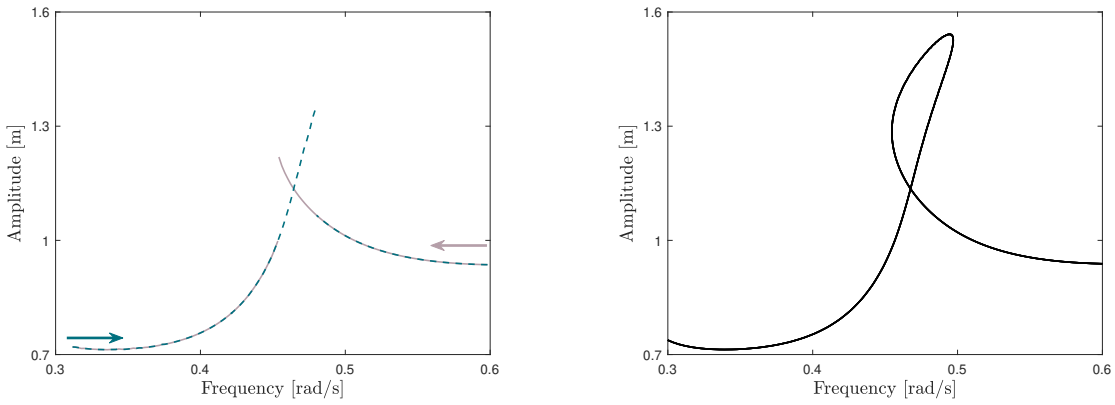

Figure 5.14: FRC around the 3 : 1 resonance of the Duffing oscillator ($p = 1$ N). (a) ACBC method. Two continuation runs are performed (—) and (- - -). (b) Harmonic balance continuation.

$\Delta\dot{X}_1^*$ [m/s]	$\Delta\omega$ [rad/s]	k_i [rad/(s N)]	k_d [kg/s]	μ [-]
0.1	0.002	0.5	0.5	0.1 t_s

Table 5.3: ACBC simulation parameters for the 3 : 1 resonance of the Duffing oscillator ($p = 1$ N).

The 3 : 1 superharmonic is not fully identified by the ACBC method, as the upper part of the loop is undetected. For the first run, the algorithm cannot turn around the loop and finds the lower branch solution instead. The second run shows similar results. Turning around the fold bifurcation is impossible with any set of parameters considered. Further investigation is needed to understand why the top of the loop is difficult to identify.

Figure 5.15 illustrates the FRC of the 3 : 1 resonance at different forcing levels.

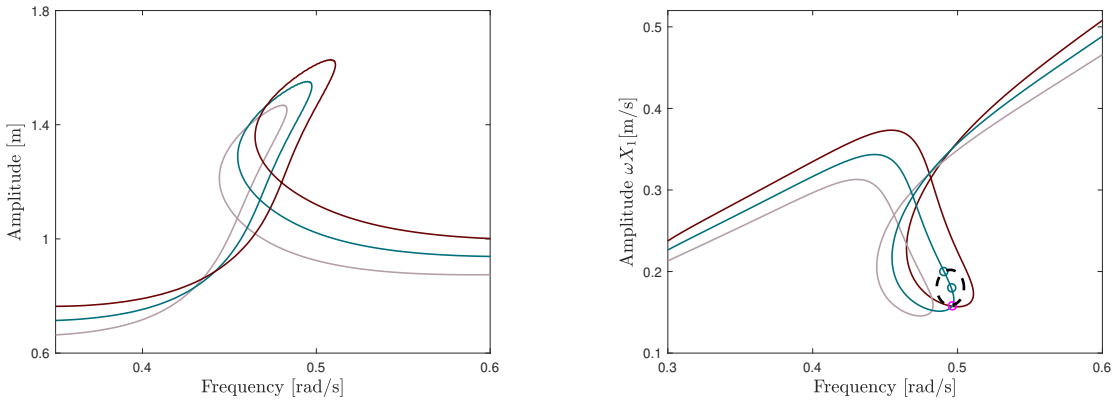

(a) (b)

Figure 5.15: Comparison of FRC around the 3 : 1 resonance for distinct forcing levels: $p = 0.9$ N (—), $p = 1$ N (—), $p = 1.1$ N (—). (a) Total amplitude, and (b) Sweeping plane. The dash-dotted line represents an ellipse, with intersections marked by two previously identified FRC solutions at 1N in blue and the next solution to identify in pink.

As the force increases, the FRC of the 3 : 1 resonance shifts along the frequency axis and amplifies. The ACBC method assumes that two FRC responses do not share the same fundamental amplitude at a particular frequency. This assumption is verified outside the superharmonic resonance region but not within it.

In the sweeping plane, the 3 : 1 FRCs at different forcing levels intersect. The pink circle in Figure 5.15b highlights two solutions of distinct FRCs (1 N and 1.1 N) with the same first harmonic amplitude at a given frequency. These solutions have different non-fundamental harmonics as they correspond to different FRCs.

Intersections in the sweeping plane are problematic. Consider the sweep of the ellipse represented in Figure 5.15b. Blue points correspond to previously identified solutions, while the pink point is the next FRC solution to be identified. Since only the fundamental harmonic is controlled during the sweep, it is uncertain which FRC will be identified at the pink point. Two situations can arise: ideally, the point corresponds to the FRC at the desired forcing 1N, satisfying the tolerance criterion, and the sweep continues to the next FRC solution. Alternatively, if the algorithm encounters the solution at 1.1N, the tolerance criterion is not satisfied, the point is rejected, and the sweep misses the solution point.

The same issue occurs with other odd superharmonics that have a loop at the top, such as 5 : 1 and 7 : 1. Figure 5.16 illustrates the identification of the 9 : 1, 11 : 1, and 13 : 1 superharmonic resonances, which do not have a loop at the top. The ACBC method can identify these superharmonics. In systems with increased damping, more odd superharmonic resonances do not exhibit a loop at the peak of the resonance curve.

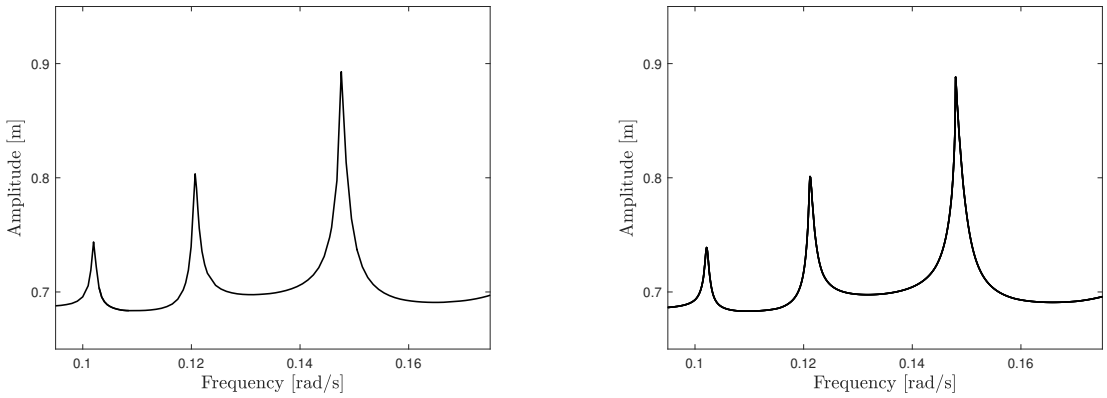

Figure 5.16: FRC around the 9 : 1, 11 : 1, and 13 : 1 resonances of the Duffing oscillator ($p = 1$N). (a) ACBC method, (b) Harmonic balance continuation.

Maintaining non-invasive forcing within the superharmonic resonance regions posed a challenge. For the l : 1 resonance, an additional tolerance criterion was introduced concerning the amplitude of the l-th harmonic in the controlled force. Further details will be provided in the next chapter.

5.3.2. Identification of even-superharmonic resonances

Figure 5.17 illustrates the identification of the 2 : 1 superharmonic resonance with the ACBC method and with HB continuation. The parameters for the simulation are presented in Table 5.4. Two continuation runs are performed for the ACBC method. The first, shown in blue in Figure 5.17a, starts from a frequency lower than the 2 : 1 resonance. The second, shown in purple, starts from a frequency higher than the 2 : 1 resonance.

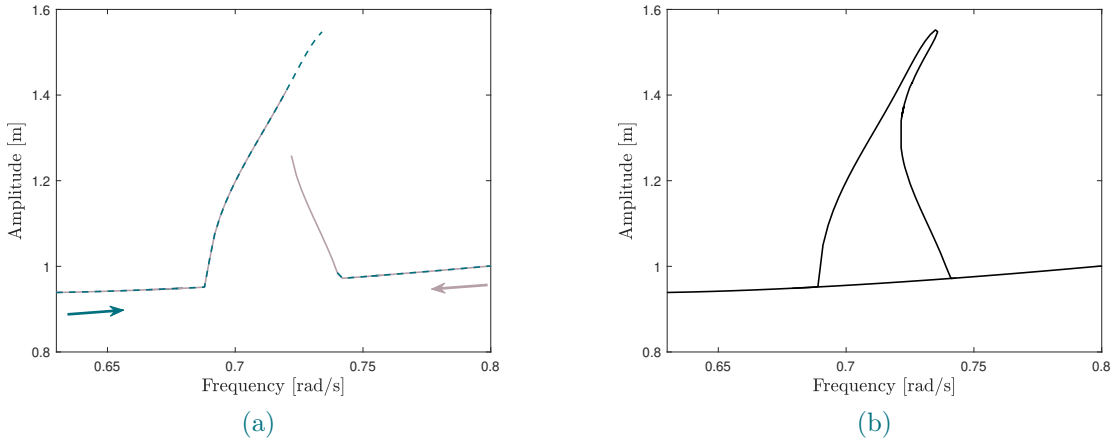

Figure 5.17: FRC around the 2 : 1 resonance of the Duffing oscillator ($p = 1$N). (a) ACBC method. Two continuation runs are performed (—) and (- -). (b) Harmonic balance continuation.

$\Delta\dot{X}_1^*$ [m/s]	$\Delta\omega$ [rad/s]	k_i [rad/(s N)]	k_d [kg/s]	μ [-]
0.1	0.002	0.5	0.1	0.1 t_s

Table 5.4: ACBC simulation parameters for the 2 : 1 resonance of the Duffing oscillator ($p = 1$ N).

The ACBC method does not identify all branches in the 2 : 1 superharmonic resonance region, missing the two unstable branches. In the first run, the stable 2 : 1 branch is identified after the symmetry-breaking bifurcation point. It reaches the fold bifurcation at the top of the 2 : 1 resonance but cannot turn around, falling to the lower part of the 2 : 1 resonance. In the second run, the stable 2 : 1 branch is followed up to the bifurcation point, where it again cannot turn around and jumps to another stable 2 : 1 branch. The unstable branches and part of the stable branch at the top of the 2 : 1 resonance are not identified. Performing the two runs for any set of parameters does not allow the identification of the unstable branches.

Identifying the 2 : 1 resonance presents a challenge similar to that of odd superharmonic resonances. In the superharmonic resonance region, multiple FRCs at different forcings share the same fundamental amplitude at a given frequency. During the sweep, it is difficult to determine which branch to follow since only the first harmonic of the response is controlled. Evaluating the non-fundamental harmonic components is necessary to differentiate these intersecting FRCs. This explains why the ACBC method jumps from one stable 2 : 1 branch to another without turning around bifurcation points.

Figure 5.18 illustrates the superharmonic resonances for different forcing levels, 1N and 3N, obtained with HB continuation [76]. For 1N, the 4 : 1 superharmonic has a sharp profile and

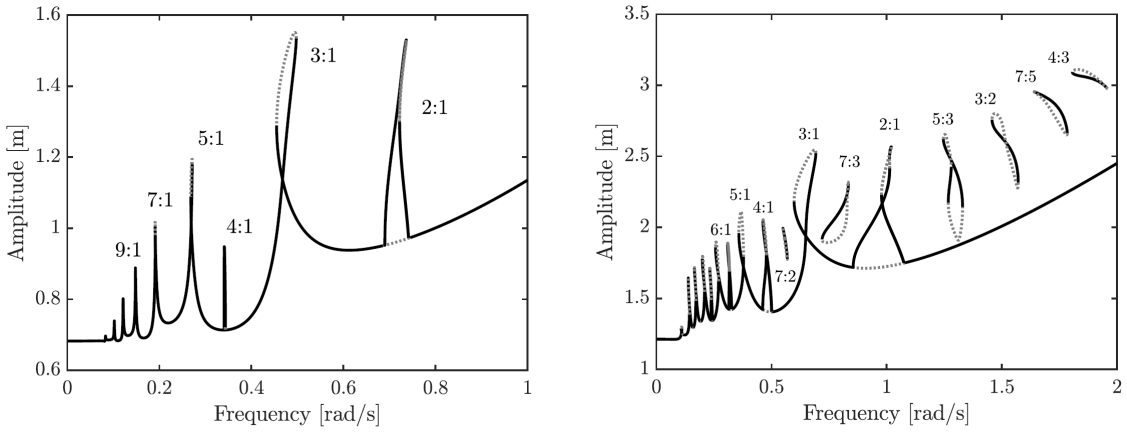

(a) (b)

Figure 5.18: FRC around the superharmonic resonances of the Duffing oscillator at distinct forcing amplitudes: (a) $p = 1$N, and (b) $p = 3$N. These results are obtained with HB continuation. The illustration is sourced from [76].

bifurcates over a narrow frequency range, making identification challenging. At 3N, its shape

resembles the 2 : 1 resonance observed at 1N. The ACBC method faces similar issues identifying the 4 : 1 superharmonic resonance as it does with the 2 : 1 superharmonic resonance.

5.3.3. Identification of subharmonic resonances

In Chapter 2, the 1 : 2 and 1 : 3 subharmonic resonances appeared detached from the main branch. Proper initialization is required to find a solution. Ideally, at a frequency within the subharmonic resonance range, one could start from the main branch and draw a large enough ellipse to intersect with the subharmonic's first harmonic component. The ACBC algorithm cannot identify the subharmonic resonance branches, even when starting from a known point on the isolated branch, instead identifying the low main branch solution.

Figure 5.19 illustrates the 1 : 3 subharmonic resonance at 1 N and the main branch FRCs for different forcing levels.

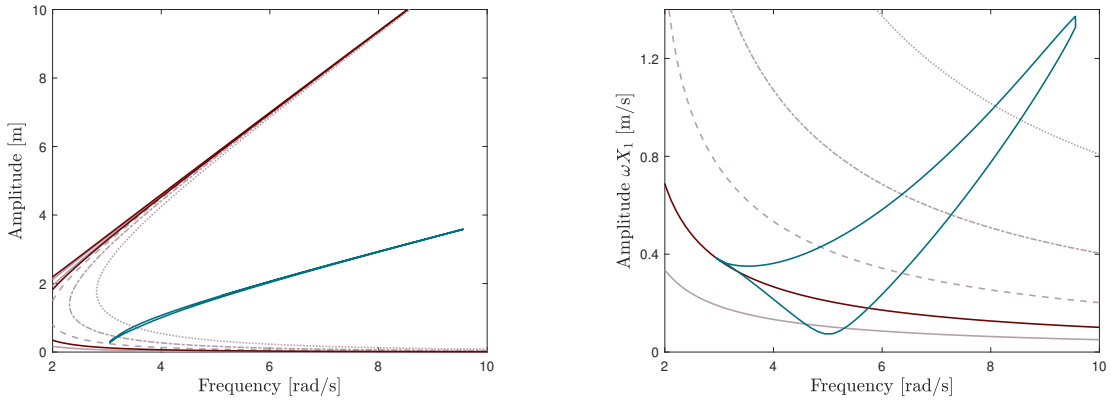

(a) (b)

Figure 5.19: FRC around the 1 : 3 subharmonic resonances of the Duffing oscillator ($p = 1$ N). The main branch FRCs are represented for distinct forcing levels, i.e. $p = 0.5$ N (—), $p = 1$ N (—), $p = 2$ N (– –), $p = 4$ N (· –), $p = 8$ N (· · ·). (a) Total amplitude. (b) Sweeping plane.

Figure 5.19b represents the sweeping plane, where several main branches of FRCs at different forcing levels intersect with the 1 : 3 subharmonic resonance at 1 N. At these intersections, the solutions share the same fundamental amplitude at a given frequency but have different non-fundamental components (see Chapter 2). Since the sweep relies solely on the first harmonic amplitude, it cannot distinguish between the two solutions. To identify the isolated FRC, non-fundamental harmonics must be controlled. The ACBC method controls only the first harmonic component during the sweep but can reject the solution point if the forcing is incorrect.

The same issue arises for the 1 : 2 subharmonic resonance.

5.4. Conclusions

This chapter began with a parametric study on the initial sweep angle, ellipse size, integral gain of the sweep rate control law, and the adaptive filters' step size factor. A fast sweep leads to inaccurate results due to transients in the adaptive filters and system response. A slower sweep rate is needed near resonance, and the tolerance criterion can introduce errors if the integral control overshoots. Adaptive filters converge if the step size factor is small enough. Several parameters require tuning in the ACBC method. Although this process is generally straightforward, further research could potentially improve user experience by identifying practical rules for various situations.

The chapter also explored the ACBC method for mapping the frequency responses of nonlinear systems, focusing on the numerical Duffing oscillator from Chapter 2.

The ACBC method successfully identified the fundamental resonance in the 1N reference case, though maintaining consistent parameters across a broad frequency spectrum proved difficult. Adapting the ellipse size is crucial for enhancing accuracy along the FRC, especially to capture curvatures or expedite computations along straighter sections.

In the 1N reference case, the method struggled to capture superharmonic behaviors accurately. The assumption that the first amplitude component at a given frequency leads to a unique solution holds for fundamental resonances but not for secondary resonances. Multiple solutions with distinct non-fundamental components may coexist at different forcing levels. Although the ACBC method is assumed to stabilize all solutions, this may not hold in superharmonic resonance regions. Additionally, isolated subharmonic resonances were beyond the method's current detection capabilities.

These observations underscore the need for further refinement of the ACBC method.

6 | Double sweep strategy

In linear systems, steady-state vibrations occur only at excitation frequencies. Nonlinearities can cause superharmonic and subharmonic responses at integer multiples or fractions of the excitation frequency. Secondary resonance often produce harmonics with amplitudes exceeding the fundamental harmonic. While superharmonic resonances are mostly attached, subharmonic resonances can be connected or separated from the main branch. Accurately characterizing these resonances is crucial for engineering designs.

Experimental characterization of secondary resonances is rarely addressed in the state of the art. Traditional offline CBC, discussed in Chapter 4, cannot characterize superharmonic resonance as it relies on S-curve unfolding, which does not apply to superharmonic resonances [1]. Combining phase-lock loop (PLL) and CBC for superharmonic resonances was proposed in [1, 28]. Experimental characterization of superharmonic and subharmonic resonances using PLL was proposed in [83]. PLL has difficulty identifying completely isolated subharmonic resonances as one phase lag no longer corresponds to a unique response (see Chapter 1).

This chapter proposes enhancements to the ACBC algorithm to address secondary resonances. It presents the motivation and principle of the double-sweep strategy, which is then applied to the secondary resonances of the numerical Duffing oscillator. The ACBC method with the double sweep strategy is implemented in Matlab/Simulink (see Appendix A.2).

6.1. Motivation

Chapter 5 showed that the ACBC method only partially identified superharmonic resonances and failed to identify subharmonic resonances. Figure 6.1a illustrates the $3:1$ superharmonic resonance in the sweeping plane.

In secondary resonance regions, one point of the sweeping plane may correspond to multiple system responses at different forcing levels. While the multiple responses share the same first harmonic component at a certain frequency, their non-fundamental components differ because they correspond to distinct forcing-level FRC solutions.

Figure 6.1b shows the $3:1$ superharmonic in a 3D plot by adding the third harmonic amplitude. Distinct FRC points with the same fundamental component at a specific frequency are distinguished by introducing the third harmonic, which significantly contributes to the response

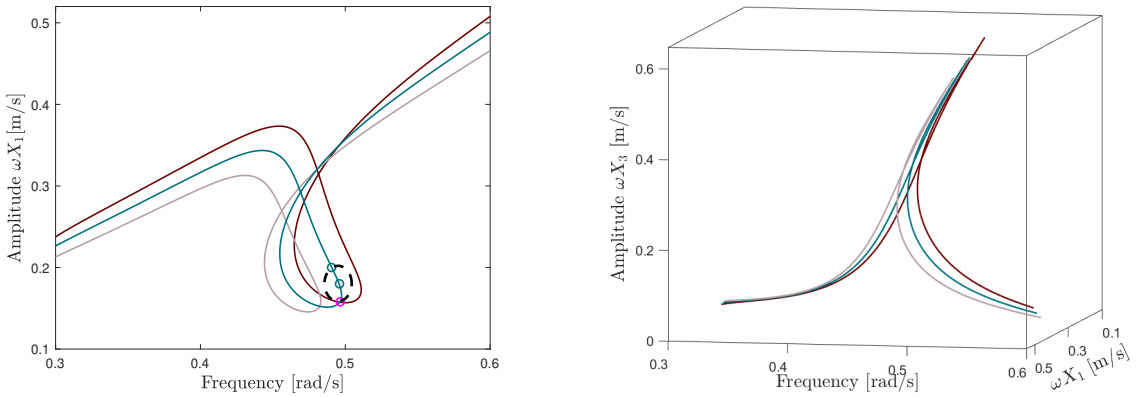

(a) (b)

Figure 6.1: Comparison of FRC around the 3 : 1 resonance for distinct forcing levels: $p = 0.9$ N (—), $p = 1$ N (—), $p = 1.1$ N (—). (a) Sweeping plane. The dash-dotted line represents an ellipse, with intersections marked by two previously identified FRC solutions at 1N in blue and the next solution to identify in pink. (b) 3D plot incorporating the third harmonic amplitude to the sweeping plane. A larger version of the 3D plot is in Appendix B.1.

in the 3 : 1 resonance region.

6.2. Double sweep strategy

The key idea is to perform a simultaneous second sweep on a non-fundamental harmonic, termed non-fundamental sweep, alongside the arclength continuation's fundamental sweep. Controlling the resonant harmonic allows for the discrimination of the different responses, and eventually for tracing out a complete FRC around a non-primary resonance.

Considering the 3 : 1 resonance example in Figure 6.2, each solution in the region with three solutions is characterized by a unique pair of Fourier coefficients $(s_{\dot{x},3}, c_{\dot{x},3})$. The illustration uses an ellipse with a null frequency semi-major axis, forming a vertical line to simplify the following explanations.

Consider fixing one of the third harmonic Fourier coefficients of the reference velocity to a constant, e.g., $s_{\dot{x}^*,3} = b$, in the ACBC method. The other non-fundamental Fourier coefficients of the system velocity are still copied into those of the reference velocity. Non-invasiveness is no longer guaranteed during the sweep because $s_{\dot{x}^*,3} \neq s_{\dot{x},3}$:

$$\begin{aligned} u(t) &= k_d \left(\dot{x}^*(t) - \dot{x}(t)\right) \\ &= k_d\, s_{u,1}\, \sin(\omega\, t) + k_d\, c_{u,1}\, \cos(\omega\, t) + k_d\, s_{u,3}\, \sin(3\,\omega\, t), \end{aligned} \tag{6.1}$$

where $s_{u,n} = (s_{\dot{x}^*,n} - s_{\dot{x},n})$ and $c_{u,n} = (c_{\dot{x}^*,n} - c_{\dot{x},n})$. The goal of the second sweeping procedure is to make the control-based experiment converge to $s_{\dot{x}^*,3} = s_{\dot{x},3} = b$, achieving non-invasiveness

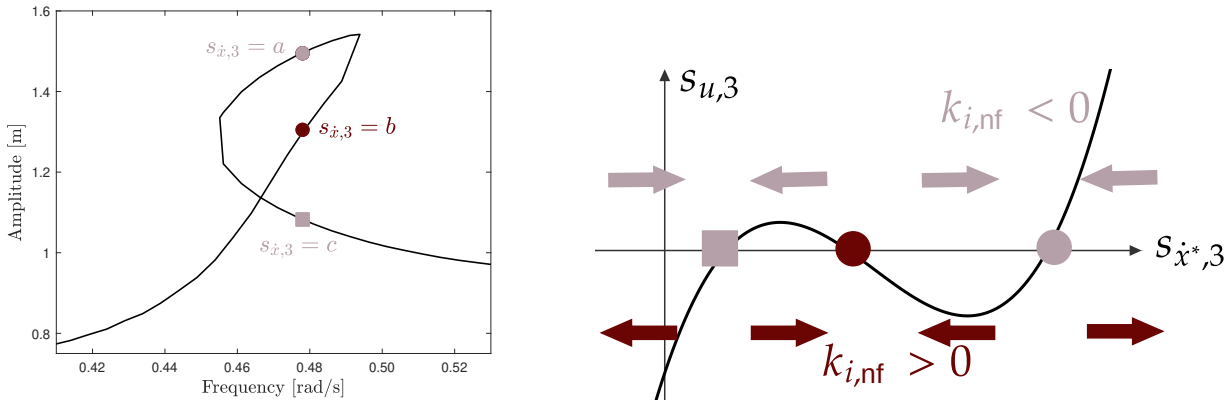

(a) (b)

Figure 6.2: (a) FRC around the 3 : 1 resonance of the Duffing oscillator ($p = 1$ N) obtained with the double sweep strategy. Colored points indicate solutions on distinct branches of the 3 : 1 resonance. (b) Evolution of one of the third harmonic Fourier coefficients of the control action $s_{u,3}$ with respect to the controlled third harmonic Fourier coefficient of reference velocity $s_{\dot{x}^*,3}$. An ellipse with a null frequency semi-major axis is used to simplify the explanations.

and identifying the middle branch solution of the 3 : 1 resonance.

Controlling this Fourier coefficient $s_{\dot{x}^*,3}$ allows convergence towards the desired solution of the 3 : 1 resonance. This control can be applied similarly to the sweep along the ellipse, either by sweeping at a constant rate on $s_{\dot{x}^*,3}$ or using an integral control law $\dot{s}_{\dot{x}^*,3} = k_{i,\mathrm{nf}}\, s_{u,3} = k_{i,\mathrm{nf}}\,(s_{\dot{x},3} - s_{\dot{x},3})$. The two sweeps are performed simultaneously. The fundamental sweep is assumed faster than the non-fundamental sweep to keep the non-fundamental reference approximately constant during the fundamental sweep. Integral control is preferred over a constant sweep rate as it ensures smooth convergence without needing the non-fundamental sweep to be much slower than the fundamental sweep.

Figure 6.2b shows the evolution of the control invasiveness $s_{u,3}$ with respect to the controlled Fourier coefficient $s_{\dot{x}^*,3}$. This is achieved by fixing $s_{\dot{x}^*,3}$ to a constant value while sweeping across the first harmonic and observing the converged value of $s_{u,3}$. It visualizes the plane where the non-fundamental sweep is performed. The sign of the controller and the initialization of the coefficient $s_{\dot{x}^*,3}$ determine which solution the control-based experiment converges towards. In Figure 6.2b, the FRC solutions with the same color are identified using the same control gain sign $k_{i,\mathrm{nf}}$ but distinct initialization.

Figure 6.3 illustrates the combination of the ACBC method with the double sweep strategy for identifying the resonance associated with the k-th harmonic. For $l : 1$ superharmonic (or $1 : \nu$ subharmonic) resonances, the non-fundamental sweep controls a Fourier coefficient of the l-th harmonic (or $1/\nu$-th harmonic) of the reference velocity.

The desired non-fundamental Fourier coefficient, such as $s_{\dot{x}^*,k}$, is controlled using an integral

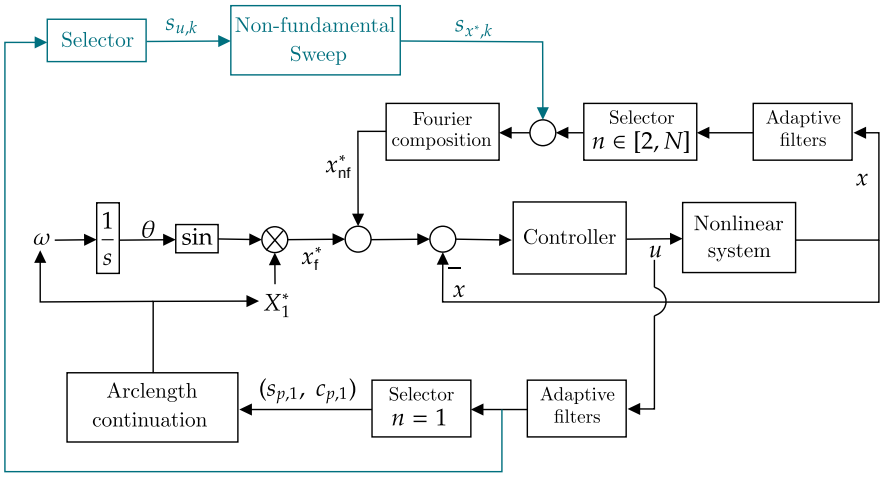

Figure 6.3: Arclength control-based continuation (ACBC) combined with the double sweep strategy (in blue). The non-fundamental sweep is performed on the k-th harmonic.

control law is $\dot{s}_{\dot{x}^*,k} = k_{i,\mathrm{nf}}\, s_{u,k}$ with the control invasiveness as input. The initial value of the controlled Fourier coefficient $s_{\dot{x}^*,k,0}$ is set based on the branch to be identified.

Adaptive filters update the other non-fundamental Fourier coefficients of the reference signal. The integral control action disappears when monoharmonic excitation is achieved and the controlled Fourier coefficient reaches its target, making the experiment non-invasive. An additional tolerance criterion is introduced for the k-th component amplitude of the control action, i.e., $\sqrt{(s_{u,k})^2 + (c_{u,k})^2} < \mathrm{tol}_{\mathrm{nf}}$. The fundamental and non-fundamental sweeps are performed simultaneously, and a solution on the sought FRC is found when both tolerance criteria are satisfied. The continuation procedure for the ACBC method with double sweeps is updated in Algorithm 6.1.

Algorithm 6.1 ACBC method with double sweep strategy.

1: $(\omega_p, \dot{X}^*_{1,p})$, $(\omega_c, \dot{X}^*_{1,c})$ and $s_{\dot{x}^*,k,0}$ defined by user
2: **loop**
3: $\alpha \leftarrow \alpha_0$
4: $s_{\dot{x}^*,k} \leftarrow s_{\dot{x}^*,k,0}$
5: $\beta \leftarrow \mathrm{atan2}(\dot{X}^*_{1,c} - \dot{X}^*_{1,p}, \omega_c - \omega_p)$
6: $(\omega, \dot{X}^*_1) = (\omega_c + \Delta\omega \cos(\beta + \pi - \alpha), \dot{X}^*_{1,c} + \Delta\dot{X}^*_1 \sin(\beta + \pi - \alpha))$
7: Wait duration t_{cooldown} for steady-state
8: **while** $|p - p^*| > \mathrm{tol}_p$ NOR $\sqrt{(s_{u,k})^2 + (c_{u,k})^2} > \mathrm{tol}_{\mathrm{nf}}$ **do**
9: Modify α and $s_{\dot{x}^*,k}$ with PID sweeping strategies while maintaining the equality in step 5 continuously
10: **end while**
11: $(\omega_p, \dot{X}^*_{1,p}) \leftarrow (\omega_c, \dot{X}^*_{1,c})$
12: $(\omega_c, \dot{X}^*_{1,c}) \leftarrow (\omega_1, \dot{X}^*_1)$
13: $s_{\dot{x}^*,k,0} \leftarrow s_{\dot{x}^*,k}$
14: **end loop**

In the ACBC method, the stop criterion prevents overshoot in the integral control sweep strategy (see Chapter 5). The method also converges to a slightly invasive solution for the resonant harmonic near secondary resonance peaks. This invasiveness can be reduced by waiting after triggering the stop criterion.

Combining the original stop criterion with the non-invasiveness criterion guarantees smooth convergence of both integral controls (accepting overshoot). This allows for a larger integral gain during the fundamental sweep, speeding up computation while maintaining non-invasive force.

6.2.1. Non-fundamental sweep illustrations

The illustration of the non-fundamental control law is also presented for an even-superharmonic resonance and a subharmonic resonance. As with the 3 : 1 resonance, the sign of the integral gain $k_{i,\mathrm{nf}}$ and the initial Fourier coefficient guide the identified solution.

Consider the identification of the 2 : 1 resonance with $s_{\dot{x}^*,2}$ as the controlled Fourier coefficient. Figure 6.4 illustrates the 2 : 1 superharmonic resonance and the relationship between $s_{u,2}$ and $s_{\dot{x}^*,2}$ for an ellipse with a null frequency semi-major axis.

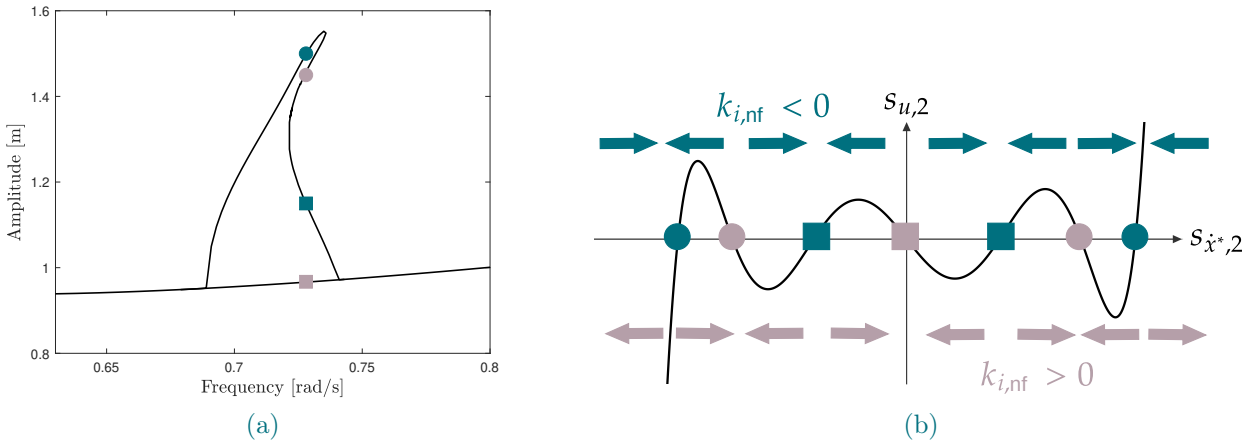

(a) (b)

Figure 6.4: (a) FRC around the 2 : 1 resonance of the Duffing oscillator ($p = 1$ N) obtained with the double sweep strategy. Colored points indicate solutions on distinct branches of the 2 : 1 resonance. (b) Evolution of one of the second harmonic Fourier coefficients of the control action $s_{u,2}$ with respect to the controlled second harmonic Fourier coefficient of reference velocity $s_{\dot{x}^*,2}$.

Even superharmonic resonances emerge from symmetry-breaking bifurcations, creating two symmetric branches wrt. the frequency axis. These branches have solutions with the same maximum absolute amplitude but differ by a phase shift of π. The associated Fourier coefficients have the same magnitude but opposite signs. This explains the seven solutions shown in Figure 6.4b. The solution with $s_{\dot{x},2} = 0$ corresponds to the unstable branch, which lacks even harmonic components.

Figure 6.5 presents the $1:2$ subharmonic resonance and the relationship between $s_{u,1/2}$ and $s_{\dot{x}^*,1/2}$ for an ellipse with a null frequency semi-major axis.

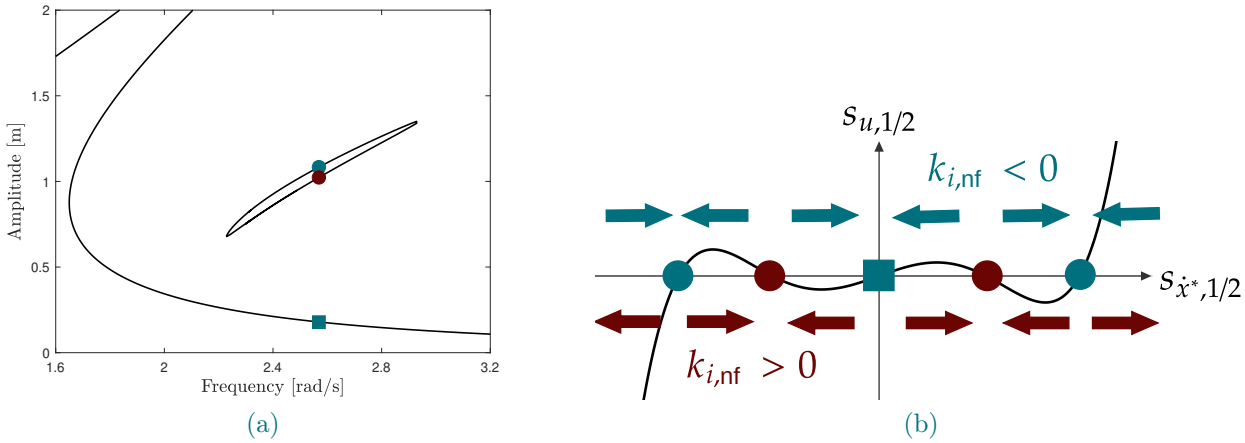

Figure 6.5: (a) FRC around the $1:2$ resonance of the Duffing oscillator ($p = 1$ N) obtained with the double sweep strategy. Colored points indicate solutions on distinct branches of the $1:2$ resonance. (b) Evolution of one of the one-half harmonic Fourier coefficients of the control action $s_{u,1/2}$ with respect to the controlled one-half harmonic Fourier coefficient of reference velocity $s_{\dot{x}^*,1/2}$.

For the subharmonic resonances $1:\nu$, there exist ν potential solutions, each characterized by the same maximum amplitude and a phase lag shifted by $2\pi/\nu$, see Chapter 2. The number of possible Fourier coefficients associated to one FRC solution depends on the subharmonic considered. For the $1:2$ subharmonic, each point on the isolated branch corresponds to two pairs of Fourier coefficients $(s_{\dot{x},1/2}, c_{\dot{x},1/2})$. The solution on the main branch does not involve any contribution from the $1/2$-th harmonic and corresponds to the point $s_{u,1/2} = 0$. Identifying an isolated subharmonic resonance starting from the low main branch is possible. One can start from a Fourier coefficient equal to zero to identify the unstable main branch with a positive integral gain $k_{i,\mathrm{nf}}$.

6.2.2. Identification procedure

In this proof of concept, distinct branches were identified through multiple trial-and-error runs. The continuation was halted at each fold bifurcation to change the sign of the non-fundamental integral gain $k_{i,\mathrm{nf}}$ and the initial value of the controlled non-fundamental Fourier coefficient.

An automatic procedure could be considered. Fold bifurcations interconnect the secondary resonance branches. As one gets closer to the bifurcation, the Fourier coefficients of the two branches converge to the same value. The two branches are identified with an opposite integral gain $k_{i,\mathrm{nf}}$. Switching the sign of the gain $k_{i,\mathrm{nf}}$ would allow to continue the identification on the branch after the fold bifurcation. The sign of the integral gain k_i of the fundamental sweep need also to be changed as the direction of the sweep is changed.

6.3. FRC identification

This section summarizes the identified responses in the numerical Duffing reference case (see Chapter 2).

Figure 6.6 shows the complete nonlinear frequency response curve of the Duffing oscillator under a 1 N harmonic force. The superharmonic and subharmonic resonances are identified using the double sweep strategy, and the fundamental resonance is identified using the ACBC method (see Chapter 5). Higher-order odd superharmonic resonances (9 : 1, 11 : 1, and 13 : 1) do not exhibit a loop atop the resonance and were identified with the ACBC method.

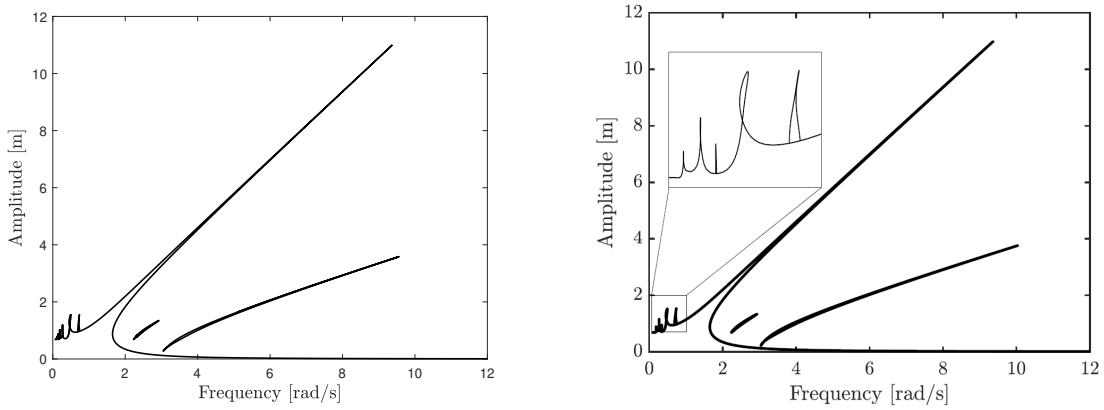

Figure 6.6: FRC of the Duffing oscillator ($p = 1$ N). (a) ACBC method. Secondary resonances are identified with the double-sweep strategy. (b) Harmonic balance continuation [77].

Figure 6.7 provides a detailed view of the frequency range where the superharmonic resonances occur.

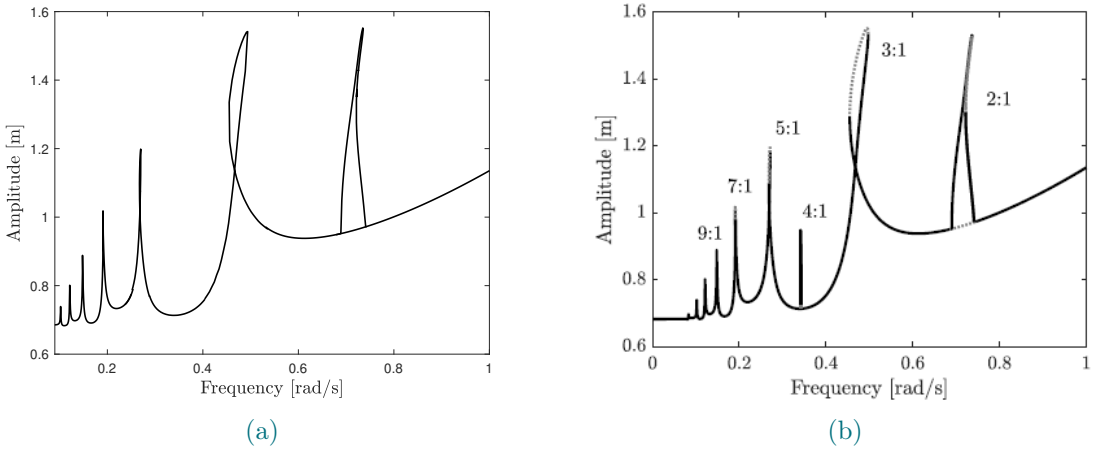

Figure 6.7: FRC around the superharmonics of the Duffing oscillator ($p = 1$ N). (a) ACBC method. Secondary resonances are identified with the double-sweep strategy. (b) HB continuation [77].

The total amplitude and harmonic contribution near the distinct secondary resonance are presented in Appendix B.2, which also summarizes the parameters used. Each integral gain was chosen by trial and error, and there could exist parameters leading to a faster characterization.

At 1N, the $4:1$ superharmonic shows a sharp shape and bifurcates narrowly, complicating its identification. At 3N, the $4:1$ resonance bifurcates over a wider frequency range. The identification of this resonance is presented in Figure 6.8. This confirms the complete identification of even-superharmonic resonance, including symmetry-breaking and fold bifurcations.

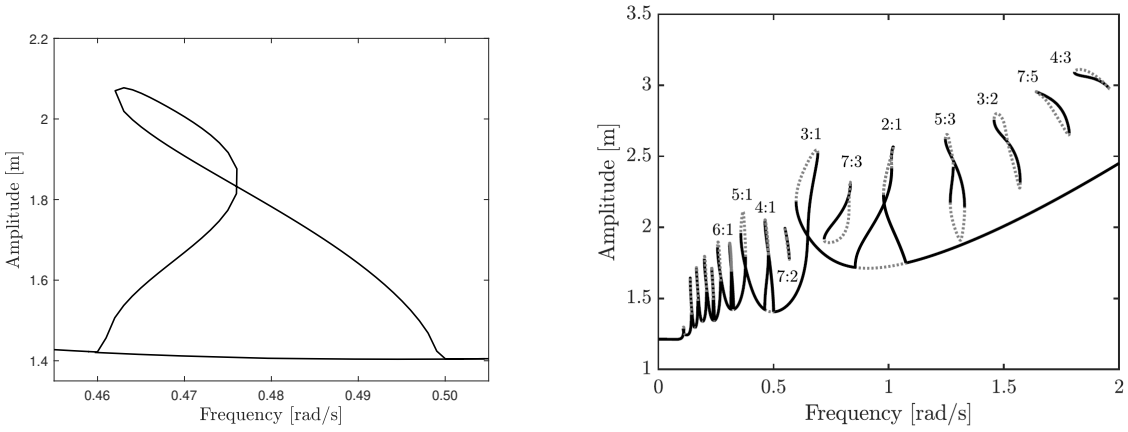

(a) (b)

Figure 6.8: FRC around the $4:1$ superharmonic of the Duffing oscillator ($p = 3$ N). (a) ACBC method with the double-sweep strategy. (b) HB continuation [77].

6.4. Conclusions

This chapter presented an improvement of the ACBC method for identifying any secondary resonance.

In secondary resonance regions, multiple FRC solutions at distinct forcing levels can share the same fundamental amplitude at a given frequency. In the ACBC method, adaptive filters update non-fundamental harmonics to ensure non-invasiveness, but it cannot discriminate between solutions during the sweep.

The double sweep strategy introduces an integral control on the resonant non-fundamental harmonic, allowing discrimination of different responses and tracing a complete FRC around a non-primary resonance. This strategy successfully identified all super- and subharmonic resonances in the numerical Duffing oscillator's frequency response. The double sweep strategy allows the identification of multiple branches at a specific frequency, enabling the choice of which branch to continue after symmetry-breaking bifurcations or detecting isolated responses, such as subharmonic resonances.

This chapter serves as a proof of concept. The identification was performed through multiple runs. A potential automation for a one-run search was proposed. Further studies are needed to

understand the interaction of the two sweeps and to establish practical rules for setting control gains appropriately.

7 | Experimental validation

Understanding nonlinear characteristics from experimental data remains challenging. Methods have been proposed using hammer impacts [5, 18, 65], shaker tables [40], and electrodynamical vibration exciters (shakers) [51, 55, 57]. Shakers are the most commonly used due to their ability to provide repeatable inputs with various signals: sinewaves, random, and transients, in both open-loop and closed-loop setups. Many vibration testing methods assume a sinusoidal excitation.

When testing structures with shakers, the structural response can distort the applied force, compromising the quality of test results. This phenomenon, known as shaker-structure interaction, results in non-fundamental harmonic content in the measured force [17, 52, 74, 75]. Higher harmonics can be generated by the nonlinear structural response or by nonlinearities in the path from the control voltage input to the applied force.

This chapter experimentally applies the original ACBC method and the double-sweep strategy to an electronic circuit implementing a Duffing oscillator. This setup addresses classical experimental issues without involving shaker-structure interactions.

7.1. Electronic Duffing

The electronic Duffing oscillator [60] is an electronic circuit designed to implement a weakly dissipative oscillator with very strong nonlinearity and relatively small resonance frequencies. The Duffing oscillator equations were presented in Equation 2.1. The setup is depicted in Figure 7.1. This circuit features one input and two outputs. The input voltage represents the force applied to the Duffing oscillator, while the output voltages correspond to the displacement and velocity of the oscillator.

The electronic system can be associated with equivalent coefficients similar to those in the Duffing equation [60]. These parameters can be adjusted by turning the knobs of the potentiometers. The parameters are summarized in Table 7.1.

According to [60], the circuit replicates the Duffing oscillator's dynamics but not perfectly due to three main non-idealities. First, voltage offsets at the input and output of integrated circuits disrupt symmetry in the oscillator. Second, imperfect integrators arise from the finite open-loop gain of operational amplifiers and dissipation in capacitors. Finally, imperfect nonlinearity results from small errors introduced by analog multipliers. The electronic system used in the

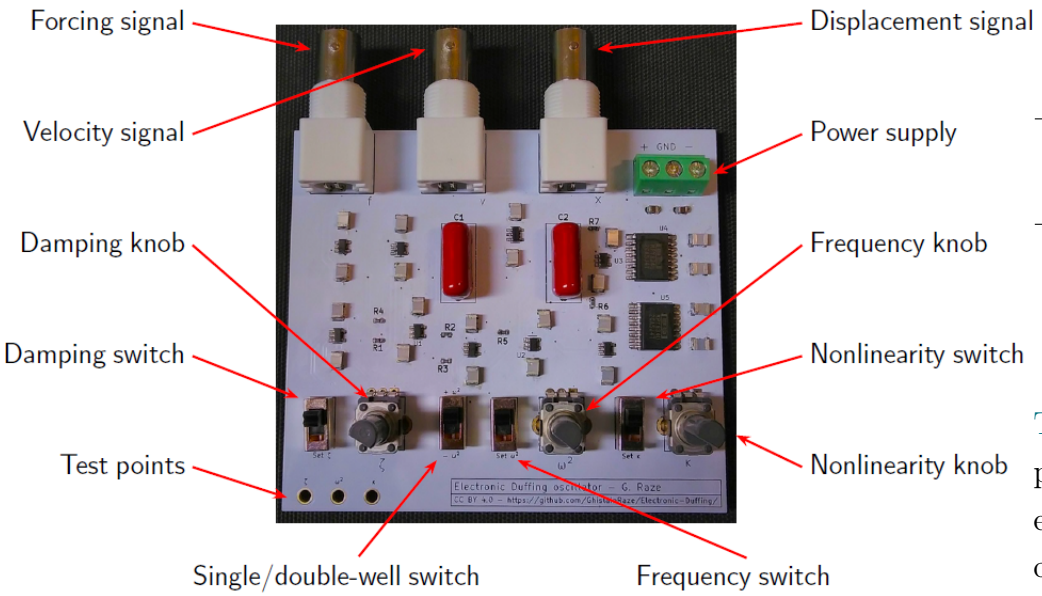

m [s^2]	c [s]
1e-4	4.947e-4

k [-]	k_3 [V^{-2}]
1.68	0.985

Table 7.1: Set of parameters for the electronic Duffing oscillator.

Figure 7.1: Setup of the electronic Duffing system [60].

lab exhibits a response offset of -0.1 V.

The electronic Duffing oscillator is interfaced with a MicroLabBox from dSPACE, where the control algorithm is implemented. The MicroLabBox is programmed with the RTI[1] for Simulink. Only minor modifications are needed, such as adding input and output blocks, and converting continuous-time blocks to their discrete-time counterparts.

7.2. Experimental results

The ACBC method is used to identify the fundamental resonance of the electronic Duffing oscillator at three distinct forcing levels. The double sweep strategy is employed to identify the $3:1$, $2:1$, and $1:3$ secondary resonances at the higher forcing level.

7.2.1. Fundamental resonances

Figure 7.2 presents the identification of the fundamental resonance of the electronic Duffing oscillator for different force levels using the ACBC method. The parameters used for the ACBC method are detailed in Table 7.2. The results obtained with the ACBC method are confirmed with the swept-up and -down sine tests, as illustrated in Figure 7.2b and in Appendix B.3.

As the forcing level increases, the fundamental resonance of the electronic oscillator shifts to higher frequencies, exhibiting behaviors like multistability and amplitude-frequency dependence, similar to hardening Duffing oscillators discussed in Chapter 2. Nonlinear hysteresis is observed when swept sine tests identify different branches in regions with multiple solutions. The jump phenomenon occurs when transitioning from multiple to single solutions. The ACBC

[1]Real-time interface

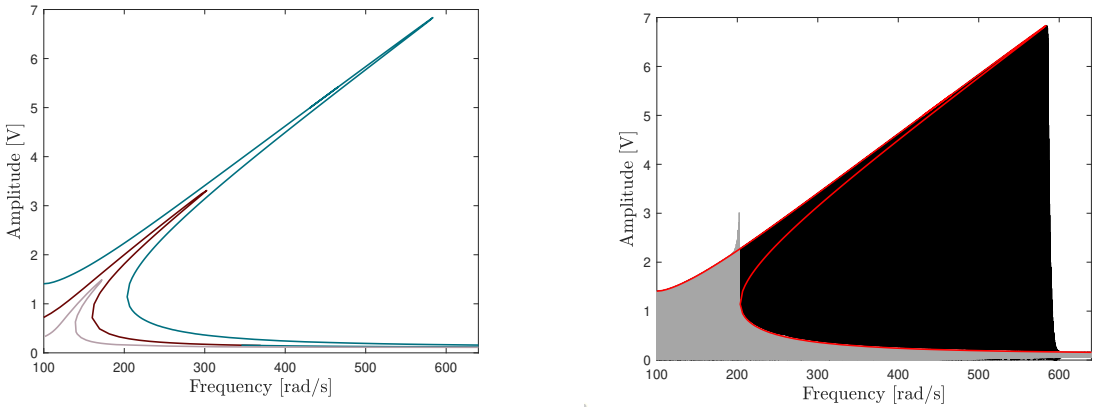

(a) (b)

Figure 7.2: (a) FRC around the fundamental resonance of the electronic Duffing oscillator for distinct forcing levels: $p = 0.125$ V (—), $p = 0.5$ V (—), $p = 2$ V (—). Results are obtained using the ACBC method. (b) Comparison of results obtained with the ACBC method (red) at $p = 2$ V, and with swept-up (black) and swept-down (grey) sine tests.

method matches swept sine results in stable solutions and identifies unstable solutions, which swept sine tests cannot.

p [V]	$\Delta\dot{X}_1^*$ [V/s]	$\Delta\omega$ [rad/s]	k_d [s]	μ [-]	k_i [rad/(V s)]
0.125	0.1	$2\pi \cdot 0.5$	5	$10\,t_s$	1

p [V]	$\Delta\dot{X}_1^*$ [V/s]	$\Delta\omega$ [rad/s]	k_d [s]	μ [-]	k_i [rad/(V s)]
0.5	0.05	$2\pi \cdot 2$	20	$10\,t_s$	0.5

p [V]	$\Delta\dot{X}_1^*$ [V/s]	$\Delta\omega$ [rad/s]	k_d [s]	μ [-]	k_i [rad/(V s)]
2	0.2	$2\pi \cdot 1$	20	$20\,t_s$	5 (start)

Table 7.2: ACBC simulation parameters for the fundamental resonance of the electronic Duffing oscillator.

The integral gain k_i was kept constant for identifying the fundamental resonance of FRC related to $p = 0.125$ and 0.5 V. For $p = 2$ V, it was necessary to reduce the integral gain as resonance approached. These observations align with those from the identification of the numerical Duffing oscillator in the 1 N reference case, as discussed in Chapter 5. Additionally, a larger differential gain k_d was required to enable the turn and stabilize the unstable solutions near resonance at higher forcing levels. The presented cases exhibit significant frequency shifts, which would be impossible to achieve in mechanical systems without causing damage.

7.2.2. Secondary resonances

The larger forcing level is considered for identifying secondary resonances. Table 7.3 summarizes the parameters used for identifying the $3:1$, $2:1$, and $1:3$ secondary resonances.

$\Delta\dot{X}_1^*$ [V/s]	$\Delta\omega$ [rad/s]	k_d [s]	μ [-]	$\lvert k_{i,\mathrm{nf}}\rvert$ [-]	$\lvert k_i\rvert$ [rad/(V s)]
0.01	0.01;0.005	5	$10t_s$	1;0.1	100
$\Delta\dot{X}_1^*$ [V/s]	$\Delta\omega$ [rad/s]	k_d [s]	μ [-]	$\lvert k_{i,\mathrm{nf}}\rvert$ [-]	$\lvert k_i\rvert$ [rad/(V s)]
0.01	0.1;0.01	1	$10\,t_s$	1	100
$\Delta\dot{X}_1^*$ [V/s]	$\Delta\omega$ [rad/s]	k_d [s]	μ [-]	$\lvert k_{i,\mathrm{nf}}\rvert$ [-]	$\lvert k_i\rvert$ [rad/(V s)]
0.01	0.1;0.01	5	$10\,ts$	1	10

Table 7.3: Double sweep strategy simulation parameters for the $3:1$, $2:1$, and $1:3$ resonances of the electronic Duffing oscillator ($p = 2$ V).

Figure 7.3 shows the $3:1$ and $2:1$ superharmonic resonances of the electronic Duffing oscillator at $p = 2$ V. It compares results from two swept sine tests with the ACBC method using the double sweep strategy.

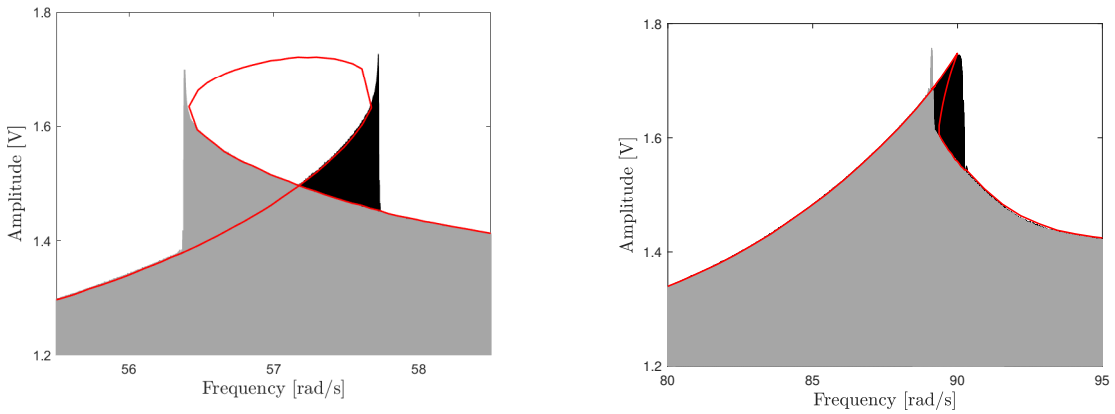

(a) (b)

Figure 7.3: FRC around the (a) $3:1$ and (b) $2:1$ resonances of the electronic Duffing oscillator at $p = 2$ V. The ACBC method results (red) using the double sweep strategy are compared with swept-up (black) and swept-down (grey) sine tests.

The superharmonic resonances appear at values larger than one-third and one-half of the natural frequency (130 rad/s). The high forcing level and cubic stiffness make the system extremely nonlinear.

For the $3:1$ resonance, the swept sine tests do not identify the top of the resonance. The jump phenomenon occurs when transitioning from a multiple-solutions region to a single-solution

region. The FRC identified with the double-sweep strategy matches the swept sine tests in the lower part of the resonance. The original ACBC method cannot turn around fold bifurcations, as explained in Chapter 6. The double-sweep strategy allows the identification of the top of the $3:1$ resonance. Near the fold bifurcation, identification is more complex due to closer Fourier coefficients, suggesting a lower integral gain for the non-fundamental sweep may be needed.

Similarly, for the $2:1$ resonance, the swept sine tests identify parts of the stable branches and jump between them, but the unstable branch is not identified. The double-sweep strategy allows the identification of the complete $2:1$ resonance. Unlike the numerical Duffing oscillator, the electronic Duffing oscillator is not perfectly symmetric, resulting in the $2:1$ resonance not arising from symmetry-breaking bifurcations. The unstable main branch with only odd harmonics is absent (see Chapter 2). This asymmetry in the electronic Duffing oscillator is due to unavoidable offsets.

The order of magnitude of the integral gains k_i and $k_{i,\mathrm{nf}}$ highlights that the fundamental sweep must be faster than the non-fundamental sweep, especially near the resonance of the non-fundamental harmonic. Stabilizing unstable solutions requires a lower differential gain k_d for secondary resonances compared to primary resonances. A less significant frequency shift is observed.

Figure 7.4 shows the $1:3$ subharmonic resonance detected and continued using the ACBC method's double sweep strategy.

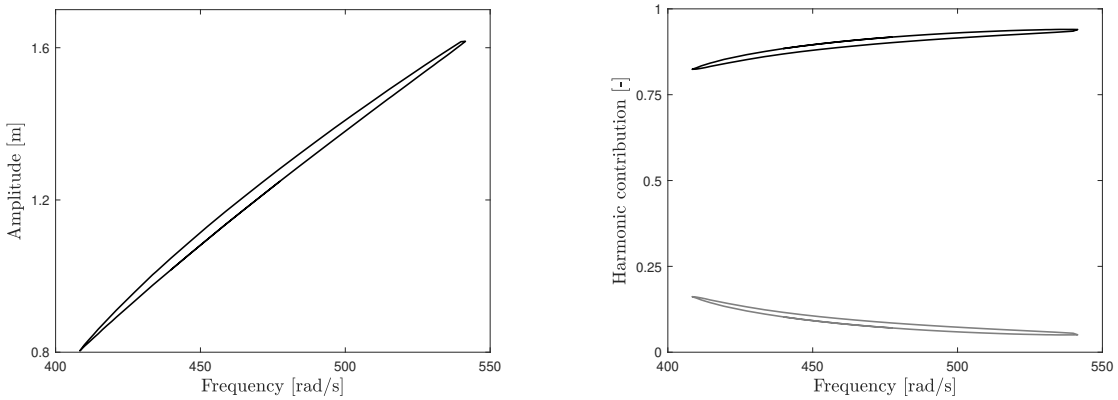

(a) (b)

Figure 7.4: FRC around the $1:3$ resonance of the electronic Duffing oscillator at $p = 2$ V. Results obtained with the double sweep strategy. (a) Total amplitude. (b) Amplitude contribution of the fundamental harmonic (black) and the one-third harmonic (grey).

Isolated responses require specific methods for identification as they do not lie in the direct continuation of the frequency response branch. In the state of the art, techniques such as stochastic interrogation excitation can be used [48]. For subharmonic resonance, a PLL based on

the PRNM principle was used in [83], but it only partially identified the subharmonic resonance. Additionally, isolated frequency response branches can occur near primary resonances due to modal interactions or nonlinear damping. These isolated responses can be detected by tracking the backbone of the fundamental resonance [80]. The original ACBC method has also been applied to experimentally detect and continue such isolated responses [1].

Using the double sweep strategy, the $1:3$ subharmonic resonance detection begins from a point on the main branch at a frequency near $3\omega_0$. The same procedure for detecting an isolated response, as presented in Section 6.2.1 of the previous chapter, was applied here. The isolated subharmonic resonance was detected and fully identified experimentally, a remarkable result. A complete subharmonic resonance had already been identified in [14] using an ad hoc method to detect the isola. The double-sweep strategy offers a more robust detection approach.

7.3. Conclusions

This chapter applied the ACBC method and the double-sweep strategy to an electronic Duffing oscillator, allowing experimental method validation without uncertainties from shaker-structure interactions.

Figure 7.5 summarizes the obtained results. The original ACBC method successfully identi-

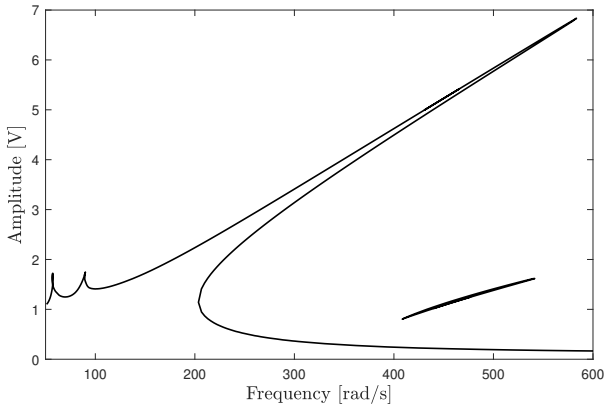

Figure 7.5: FRC of the electronic Duffing oscillator ($p = 2$ V). The fundamental resonance was obtained using the original ACBC method, while secondary resonances were identified with the double-sweep strategy.

fied the fundamental resonance with a significant frequency shift. The double-sweep strategy identified one even and one odd superharmonic resonance. Additionally, a subharmonic was detected from the FRC main branch and fully identified, which is a notable result. While other secondary resonances exist, their identification was not attempted. Future work could focus on this. This chapter demonstrates the double-sweep strategy's application to various secondary resonances of the electronic Duffing oscillator.

The ACBC method, with and without the double sweep strategy, was applied to the electronic Duffing oscillator similarly to the numerical example, with only parameter changes. No new limitations were encountered, demonstrating the methods' robustness. Further work is needed to study the range of parameters for which both versions of the ACBC method are effective.

8 | Adaptive ellipse size

In the ACBC method, the ellipse size remains constant throughout the frequency range. The ellipse size influences both the sweep rate and FRC discretization, necessitating a small ellipse, as detailed in Chapter 5. Three crucial factors define the quality of a solution: computational speed, discretization, and robustness. A constant small step length ensures accurate curvature capture but demands significant computational time. Robustness relates to the number of analysis restarts required.

Figure 8.1a shows the drawback of using a large step length. Adjusting the ellipse size based on the curvature of previous solutions can reduce computational time. Larger sizes are used in straighter sections and smaller ones in curved parts, as shown in Figure 8.1b.

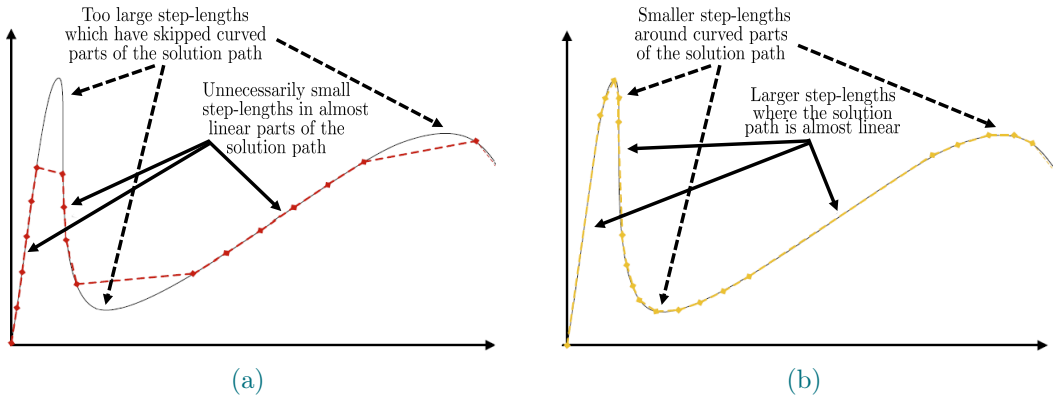

Figure 8.1: (a) Approximate representation (in red) of the exact solution (in black) using a constant step length. (b) Approximate representation (in yellow) of the exact solution (in black) using an adaptive step length. This illustration is sourced from [24].

This chapter introduces an adaptive ellipse size strategy in the ACBC method. The strategy, based on curvature, is first explained and then applied to the reference Duffing oscillator under 0.01 N force.

8.1. Principle of the adaptive strategy

Fayezioghani et al. [24] proposed an adaptation law for quasi-static problems based on local curvature. This curvature is calculated using the cosine distance between a hyper angle δ and an optimal hyper angle δ_{opt}. The hyper angle δ is defined between the line connecting two

solution points (the linearized solution path) and the tangent to the analytical curve at the second point.

In the present work, the analytical solution is unknown. The hyper angle is calculated from the difference between the two previous FRC slope angles β in the sweeping plane (see Figure 8.2a).

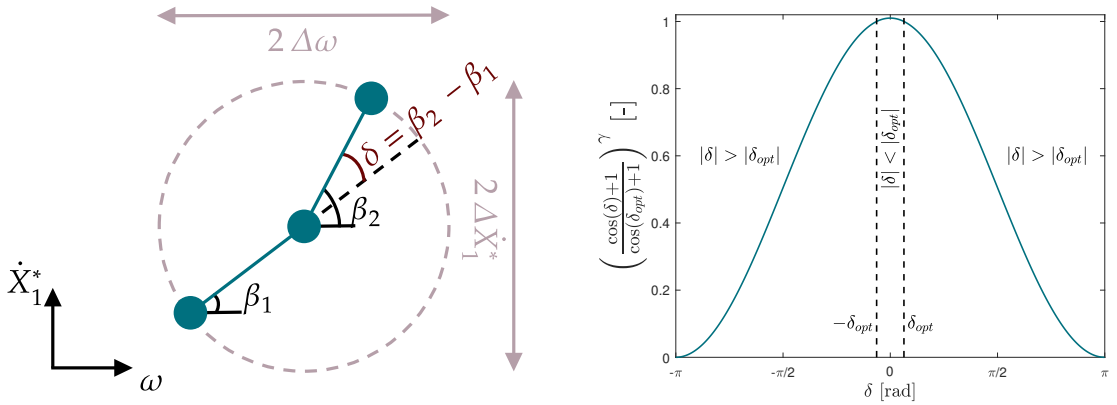

Figure 8.2: (a) Illustration of the hyper angle δ, defined as the angle between the two previous FRC segments. The blue points denote the three most recently determined points on the FRC. β denotes the FRC slope angle. (b) The cosine distance versus the hyper angle δ is drawn for an optimal hyper angle $\delta_{\text{opt}} = 0.2$ and $\gamma = 1$.

The proposed adaptive ellipse size law is based on the cosine distance between the hyper angle δ and an optimal hyper angle δ_{opt}:

$$\Delta\dot{X}^*_{1,n+1} = \left(\frac{\cos(\delta_n)+1}{\cos(\delta_{\text{opt}})+1}\right)^{\gamma} \Delta\dot{X}^*_{1,n}. \tag{8.1}$$

where n indicates the current ellipse, and γ is a magnifying exponent. To simplify, only one of the ellipse's semi-major axes is varied, with the other parameter fixed, assuming constant eccentricity. Circular ellipses are considered, i.e., $\Delta\dot{X}^*_1 = \Delta\omega$.

As shown in Figure 8.2b, the step size increases when the hyper angle is smaller than the optimal angle and decreases when the hyper angle is larger. The adaptive strategy tries to keep the hyper angle δ close to δ_{opt}. The optimal angle δ_{opt} should not be exactly 0, as this would cause the step size to progressively decrease to an infinitesimally small value.

Figure 8.3 illustrates the effect of the exponent γ on the cosine distance.

In Figure 8.2b, the cosine distance remains close to 1 when $|\delta| < |\delta_{\text{opt}}|$. In this range, a larger exponent, denoted γ_{max}, is required to accelerate the increase of the ellipse size. Conversely, for $|\delta| > |\delta_{\text{opt}}|$, the rate of size decrease with $\gamma = 1$ is satisfactory.

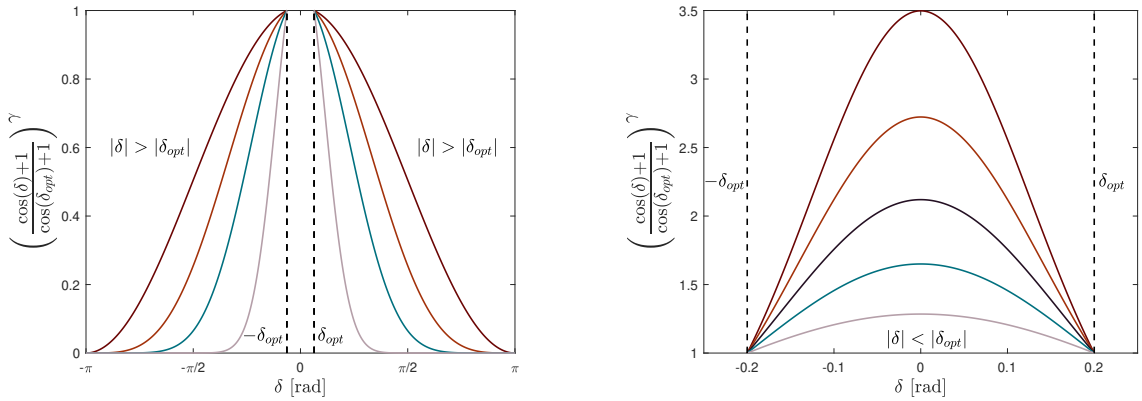

Figure 8.3: The cosine distance versus the hyper angle δ is drawn for an optimal hyper angle $\delta_{\text{opt}} = 0.2$ rad with various γ values: (a) $\gamma = 1$ (—), $\gamma = 2$ (—), $\gamma = 4$ (—), $\gamma = 16$ (—) (b) $\gamma = 25$ (—), $\gamma = 50$ (—), $\gamma = 75$ (—), $\gamma = 100$ (—), $\gamma = 125$ (—).

If the hyper angle deviates significantly from the optimal value, $|\delta| > |\delta_{\text{tol}}|$, a restart is necessary since δ is only known after computing the new point. Restarts often occur in high-curvature regions. The ellipse size is decreased based on the cosine distance and an exponent γ_{restart}. A larger γ_{restart} results in a stronger decrease in ellipse size to restart the computation. This value is set above 1 to avoid frequent consecutive restarts but should not be too large to prevent excessive reduction of the ellipse size. The choice of the tolerance angle δ_{tol} and the optimal angle δ_{opt} is illustrated in the next section. The adaptive ellipse size strategy is detailed in Algorithm 8.1. The ellipse size is adjusted when a FRC solution is found during arclength continuation. The adaptive strategy begins once the first two points have been computed.

Algorithm 8.1 Adaptive ellipse size strategy.

δ_{tol}, δ_{opt}, $\gamma_{\max}$, and γ_{restart} defined by user
$(\omega_p, \dot{X}_p^*)$ and $(\omega_c, \dot{X}_c^*)$ defined by arclength continuation
$\beta_1 \leftarrow \beta_2$
$\beta_2 \leftarrow \text{atan2}(\dot{X}_c^* - \dot{X}_p^*, \omega_c - \omega_p)$
$\delta \leftarrow \beta_2 - \beta_1$
if $|\delta| \leq |\delta_{\text{tol}}|$ **then**
  if $|\delta| \leq |\delta_{\text{opt}}|$ **then**
    $\gamma \leftarrow \gamma_{\max}$
  else
    $\gamma \leftarrow 1$
  end if
else
  $\gamma \leftarrow \gamma_{\text{restart}}$
end if
$\Delta\dot{X}_1^* \leftarrow \left(\dfrac{\cos(\delta)+1}{\cos(\delta_{\text{opt}})+1}\right)^{\gamma} \Delta\dot{X}_1^*$

8.2. Application of the adaptive strategy

This section illustrates and discusses the results of the adaptive strategy based on the parameters used. Table 8.1 summarizes these parameters.

$\Delta\dot{X}^*_{1,\text{start}}$ [m/s]	$\Delta\dot{X}^*_{1,\text{max}}$ [m/s]	$\Delta\dot{X}^*_{1,\text{min}}$ [m/s]	γ_{restart} [-]
0.025	0.2	0.005	4

k_i [rad/(s N)]	δ_{opt} [rad]	δ_{tol} [rad]	α_0 [rad]
0.25	0.1; 0.15; 0.2	0.2; 0.4	π

Table 8.1: Simulation parameters for the adaptive step strategy applied to the fundamental resonance of the numerical Duffing oscillator ($p = 0.01$ N). A circular ellipse is considered $\Delta\omega = \Delta\dot{X}^*_1$.

The integral gain is kept constant. Both the integral gain and ellipse size influence the sweep rate, as detailed in Chapter 5. To maintain an adequate sweep rate, the integral gain must be small enough for the various ellipse sizes. Ideally, the integral gain should be adjusted simultaneously with the ellipse size.

Setting the upper limit of the ellipse size $\Delta\dot{X}^*_{1,\text{max}}$ too high can cause the continuation to miss the resonance peak. To avoid this, the upper limit should be predetermined based on the bandwidth of the linear system's resonance. A phase criterion could also detect if the size was too large, as the phase lag shifts by π after the resonance.

Three examples are considered to compare the results based on the tolerance angle δ_{tol}, optimal angle δ_{opt}, and exponent γ_{max}.

Figure 8.4 shows the cosine distance for various parameter pairs $(\gamma_{\text{max}}, \delta_{\text{opt}})$. The exponent γ_{max} adjusts based on the optimal hyper angle δ_{opt} to ensure a consistent maximum value increase when $\delta = 0$. This allows for the comparison of results with different optimal angles. These pairs of values are used in subsequent analyses.

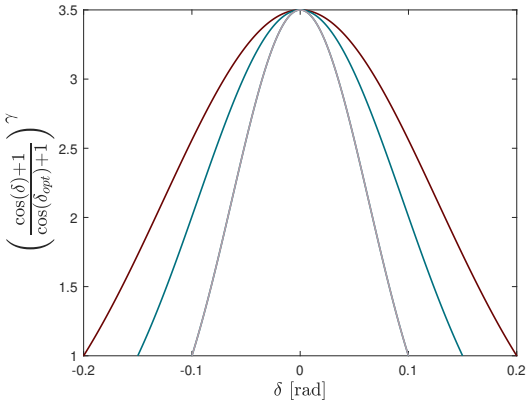

Figure 8.4: The cosine distance versus the hyper angle δ for different pairs of parameters: $\delta_{\text{opt}} = 0.2$ and $\gamma = 125$ (—), $\delta_{\text{opt}} = 0.15$ and $\gamma = 222$ (—), $\delta_{\text{opt}} = 0.1$ and $\gamma = 501$ (—).

Figure 8.5 illustrates the adaptive step strategy for various tolerance angles δ_{tol}. The acceptable angle interval is $[-\delta_{\text{tol}}; \delta_{\text{tol}}]$ and the optimal angle set to $\delta_{\text{opt}} = \delta_{\text{tol}}/2$. The ellipse is equally increased or decreased within the acceptable angle interval. The continuation process starts at

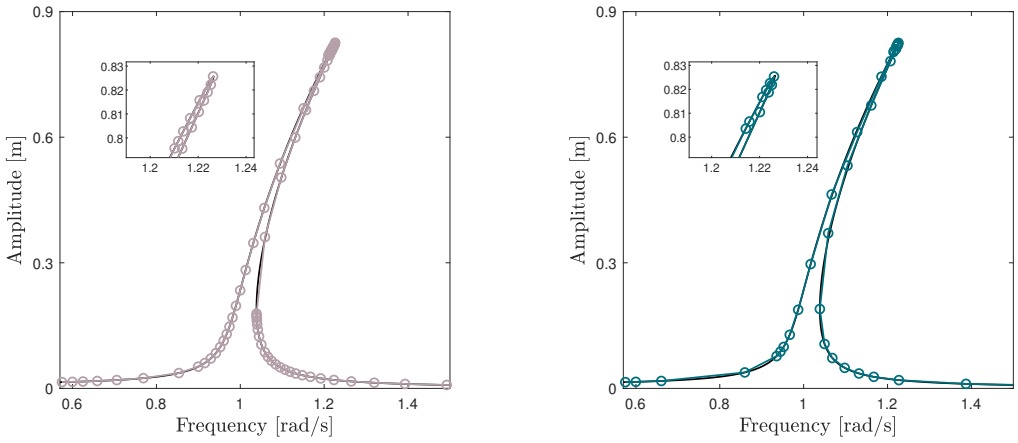

Figure 8.5: FRC around the fundamental resonance of the Duffing oscillator ($p = 0.01$ N) using the adaptive step size strategy with $\delta_{\text{opt}} = \delta_{\text{tol}}/2$, varying the tolerance angle: (a) $\delta_{\text{tol}} = 0.2$ rad, (b) $\delta_{\text{tol}} = 0.4$ rad.

low frequencies. The adaptive strategy begins once the first two FRC points are identified.

For larger δ_{tol} and δ_{opt}, larger steps occur in curved regions, either at the bottom or top of the resonance, as the tolerance criterion accepts larger angles. The ellipse increase is faster in straight regions, e.g. at the start of the frequency range. Although the maximal value is the same in Figure 8.4, the ellipse increase at any specific angle is larger with a larger optimal angle. The adaptive strategy aims to keep the hyper angle close to its optimal value, resulting in smaller steps for the smaller optimal angle case. Imposing a lower tolerance angle makes the strategy more prone to restarts.

The objective is to achieve a result similar to $\delta_{\text{tol}} = 0.4$ rad using $\delta_{\text{tol}} = 0.2$ rad by adjusting δ_{opt}. Figure 8.6 shows the adaptive step strategy for δ_{opt} at different proportions of the acceptable angle interval.

Increasing the proportion of the optimal angle relative to the tolerance angle has consequences. The portion leading to an ellipse size increase becomes larger. For the same hyper angle, the ellipse size increase is greater with a larger optimal angle (see Figure 8.4). More straight segments are observed with a larger optimal angle. Comparing Figures 8.5b and 8.6b, similar results are seen for the straight regions. The curved regions at the bottom of the resonance are more refined with the lower tolerance angle. This is not observed on top of the resonance, but this probably depends on the history of the ellipse increase. In Figure 8.6b, a large segment is observed until the peak of the resonance. In contrast, in Figure 8.5b, a large segment lands before the peak, causing restarts before turning around the resonance.

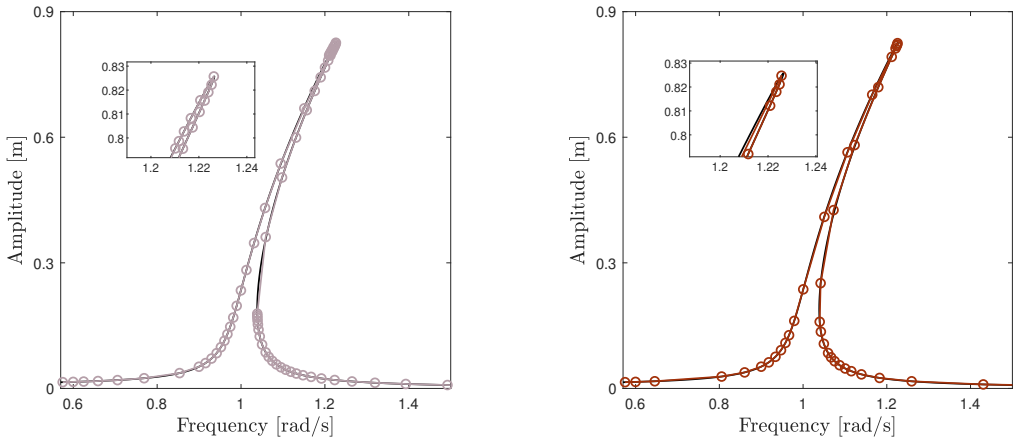

(a) (b)

Figure 8.6: FRC around the fundamental resonance of the Duffing oscillator ($p = 0.01$ N) using the adaptive step size strategy with $\delta_{\text{tol}} = 0.2$, varying the optimal angle: (a) $\delta_{\text{opt}} = \delta_{\text{tol}}/2$, (b) $\delta_{\text{opt}} = 3\,\delta_{\text{tol}}/4$.

Figure 8.7 presents the adaptive step strategy for distinct exponents γ_{max} of the cosine distance.

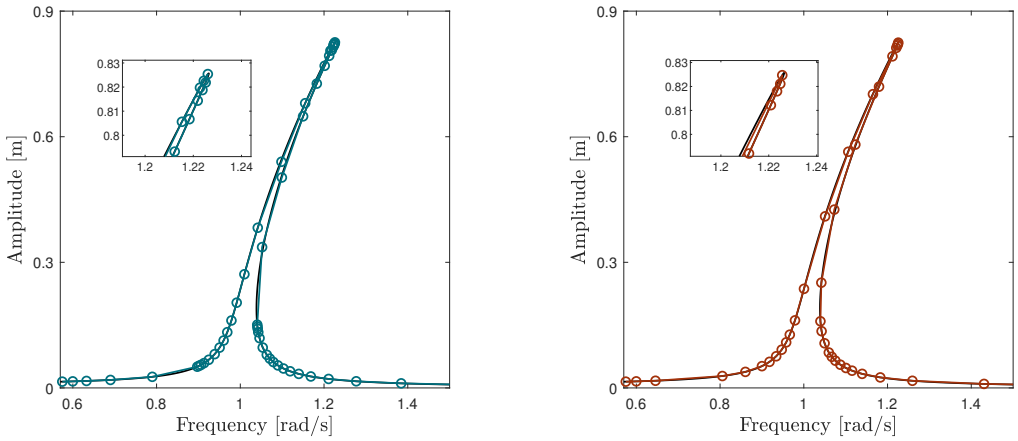

(a) (b)

Figure 8.7: FRC around the fundamental resonance of the Duffing oscillator ($p = 0.01$ N) using the adaptive step size strategy with $\delta_{\text{tol}} = 0.2$ and $\delta_{\text{opt}} = 3\,\delta_{\text{tol}}/4$, varying the exponent γ_{max}: (a) $\gamma_{\text{max}} = 99$, (b) $\gamma_{\text{max}} = 222$. The maximum cosine distance for (a) is 1.75 and for (b) 3.5.

The exponent γ_{max} controls the rate of ellipse size increase (see Figure 8.3b). With a lower exponent, the ellipse size increases more gradually with more steps. At the end of the resonance, distinct ellipse reduction behaviors are observed. With $\gamma_{\text{max}} = 222$, the ellipse size reduces slowly, while with $\gamma_{\text{max}} = 99$, the reduction is abrupt due to a restart. This behavior is hard to predict as it depends on the history of ellipse adjustment, which itself depends on the starting point and the rate of ellipse increase or decrease.

8.3. Conclusions

The chapter introduced an adaptive ellipse size strategy that adjusts the size of the ellipse based on curvature: larger sizes are used in straighter sections and smaller sizes in curved sections. This approach aims to balance discretization accuracy and computational speed.

To simplify, the integral gain was set to a constant value. This is not optimal as the ellipse size changes significantly. A further analysis of the integral gain could help identify a condition related to the ellipse size, ensuring a sufficiently slow sweep.

A comparison was presented in a specific case to illustrate the influence of the parameters to be tuned, though it is not exhaustive. From these discussions, it was observed that the tolerance angle affects the number of restarts and the ellipse size in curved regions. The position of the optimal angle within the acceptable angle interval drives the rate at which the ellipse size is adjusted. The exponent $\gamma_{\max}$ determines how quickly the ellipse size increases. Resonance turn is well-discretized in all the cases.

The adaptive strategy is effective when parameters are well-tuned. However, many parameters need tuning, and this process is complex, often requiring multiple identification attempts to find the optimal set. Work still needs to be performed to strengthen the robustness of the adaptive strategy.

9 | Conclusions and future developments

Experimental modal analysis predicts responses to periodic excitation in linear systems but struggles with real-world nonlinearities. Diverse phenomena can appear, including multiple stable and unstable solutions resulting from bifurcations, and attached or detached secondary resonances. Traditional EMA methods, like swept or stepped sines, identify only one stable solution in regions with multiple solutions, leading to jump phenomena. Control-based nonlinear vibration testing addresses these issues with closed-loop experiments to stabilize all responses, providing a more systematic and reliable approach. This research aimed to advance the ACBC methodology proposed for online, derivative-less control-based nonlinear vibration testing. This method is designed to experimentally identify frequency responses of nonlinear systems subjected to harmonic forcing, without relying on predefined mathematical models.

This master's thesis addressed two research questions:

a) Is the ACBC algorithm capable of identifying the complete frequency response of a numerical/electronic Duffing oscillator, including secondary resonances with complex topology?

b) How can the step size selection in the ACBC algorithm be automated to ensure accurate frequency response capture?

To adequately address these research questions, some background was necessary. Chapter 2 illustrated the complex and rich dynamics of the harmonically forced Duffing oscillator. The system was nondimensionalized, making the results applicable to any Duffing system. Chapter 3 explained control theory and the effects of PID tuning. Chapter 4 highlighted the advantages of the ACBC method over traditional CBC.

The first question encompassed nearly the entire work. Chapters 5 and 6 focused on the numerical Duffing oscillator, while Chapter 7 considered the electronic Duffing oscillator. In Chapter 5, the ACBC algorithm identified the fundamental resonance using constant parameters and the PID sweep strategy. The fundamental resonance shifts significantly to higher frequencies for lightly damped nonlinear systems under high forcing, complicating identification with constant parameters. The superharmonic resonances were only partially identified, while subharmonic resonances were not identified at all.

In secondary resonance regions, a key assumption of the ACBC method no longer holds, as multiple FRC solutions at different forcing levels can share the same fundamental amplitude at a specific frequency. To address this, Chapter 6 introduced the double sweep strategy, which distinguishes different intersecting solutions by sweeping the non-fundamental resonating harmonic using integral control. The fundamental and non-fundamental sweeps are performed simultaneously, with the fundamental sweep assumed to be faster. By adjusting the sign of the non-fundamental integral gain and the initialization of the controlled non-fundamental harmonic, the double sweep strategy can converge to distinct solutions. This method successfully identified complete superharmonic resonances and isolated subharmonic resonances, achieving the detection of isolated responses.

Chapter 7 applied both methods to the electronic Duffing oscillator [60], avoiding experimental uncertainties from shaker-structure interactions. The ACBC method identified the fundamental resonance at three distinct forcing levels. The double sweep strategy identified one of each type of secondary resonance, including odd- and even-superharmonic and subharmonic resonances. No additional limitations were introduced in either method compared to the numerical Duffing oscillator.

The second question was investigated in Chapter 8 using an adaptive ellipse size strategy based on the local curvature of the FRC. Further research is needed to refine this strategy, as several parameters require tuning and their relationships must be studied. When well-tuned, the adaptive strategy performed effectively in the low-forcing case considered.

The main contribution of this thesis is the introduction of the double-sweep strategy, a pioneering experimental method for detecting isolated responses, including subharmonic resonances. This represents the first robust method for such experimental detection. Furthermore, the double-sweep strategy enables the continuation of both superharmonic and subharmonic resonances. The performance and innovative features of the double-sweep strategy will be showcased in an upcoming journal publication.

9.1. Further improvements and perspectives

The Duffing oscillator was used as the primary example of a nonlinear oscillator throughout this thesis. While it effectively illustrates many aspects of nonlinear oscillations, exploring other systems with more complex nonlinearities, such as piecewise linear or polynomial stiffness, Coulomb friction, or nonlinear damping is essential.

Exploring nonlinear systems with higher-dimensional structures is a crucial direction for future research. An initial step in this direction is demonstrated using a numerical system with two clamped masses and a cubic spring [76]. This setup reveals a $3:1$ modal interaction between the second mode's $3:1$ resonance and the first mode's fundamental resonance. At low forcing

levels, an isolated response emerges near the fundamental resonance of the first mode, merging with this resonance as the forcing increases. The double sweep method detected and continued the isolated response by controlling the third harmonic response (see Figure 9.1).

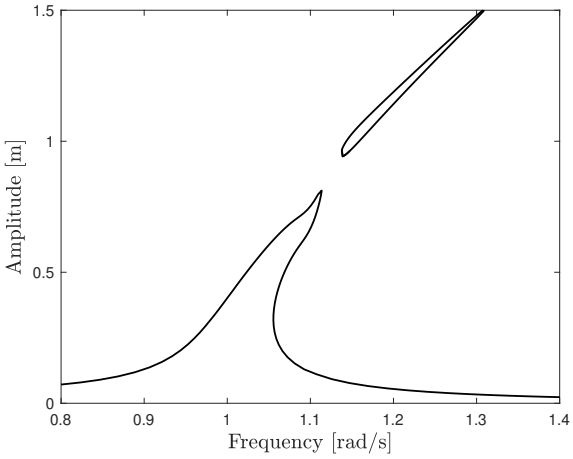

Figure 9.1: FRC of the first mode displacement for a two-degree-of-freedom system under a 0.05 N harmonic force, illustrating the isolated response generated by 3 : 1 modal interactions. Fundamental resonance and isola were identified using the double-sweep strategy. The dynamics of the considered 2DOF system are detailed in [76].

The maturity of control-based methods for industrial applications requires automatic adaptation of parameters to ensure effectiveness across various systems. Several parameters require tuning in the ACBC method. An adaptive strategy was proposed for ellipse size, which is effective for well-tuned parameters but introduces four new parameters. Further research is needed to identify practical rules for setting these parameters based on the desired performance. The adaptive step strategy uses various ellipse sizes, and maintaining a constant integral gain is not optimal. Establishing a relationship between ellipse size and integral gain for an appropriate sweep rate is necessary, and it is also beneficial for the constant step size strategy.

Throughout the ellipse sweep, the controller applies a varying forcing amplitude to the structure. In practical experiments, this amplitude might become excessively large, going beyond shaker limitations or leading to structural breakdown. It is worth noting that using an ellipse with a different eccentricity would not necessarily alleviate this issue if the ellipse's semi-major axes remain parallel to the Cartesian frame. An alternative eccentricity could be beneficial if the ellipse is oriented parallel to the FRC, as this adjustment would enable greater spacing between steps while minimizing overlap with higher forcing FRCs. Other derivative-free approaches, alternative to the ellipse sweep, could also be investigated. For example, the piecewise-linear continuation method [6–9] was recently used experimentally [33].

The control-based experiment stabilizes the sought periodic orbits of the uncontrolled system when the control gain is sufficiently high. In this work, the differential gain was set by trial and error due to the absence of a robust tuning method. Excessively high differential gain can destabilize the system. Future research could explore adaptive controllers that automatically adjust the gain during experiments [47].

Further investigation of the double-sweep strategy is needed. Examining the interaction between the two sweeps could provide practical guidelines to ensure the algorithm operates cor-

rectly in any situation. Currently, the strategy involves stopping at fold bifurcations and switching the integral gain sign, but an automatic procedure could be implemented. Finally, rigorous proof is necessary to ensure the algorithm can reliably find a solution that meets both tolerance criteria.

A | Matlab/Simulink diagrams

A.1. ACBC method

Understanding the Simulink diagrams is facilitated by referencing Algorithm 4.1 or Figure 4.7.

In Figure A.1, the arclength continuation process uses a PID sweep strategy, defined by $\dot{\alpha} = k_i(p - p^*)$. Once the tolerance criterion $|p - p^*| < \text{tol}_p$ is satisfied, the cooldown phase dampens transients by disconnecting the arc angle α from the PID control. Transitions between search and cooldown phases are managed using switches. The sweep angle in the diagram is calculated as $\beta + \pi - \alpha - \alpha_0$. The variable *curr* contains $(\omega_c, \dot{X}^*_{1,c})$, while *prev* contains $(\omega_p, \dot{X}^*_{1,p})$.

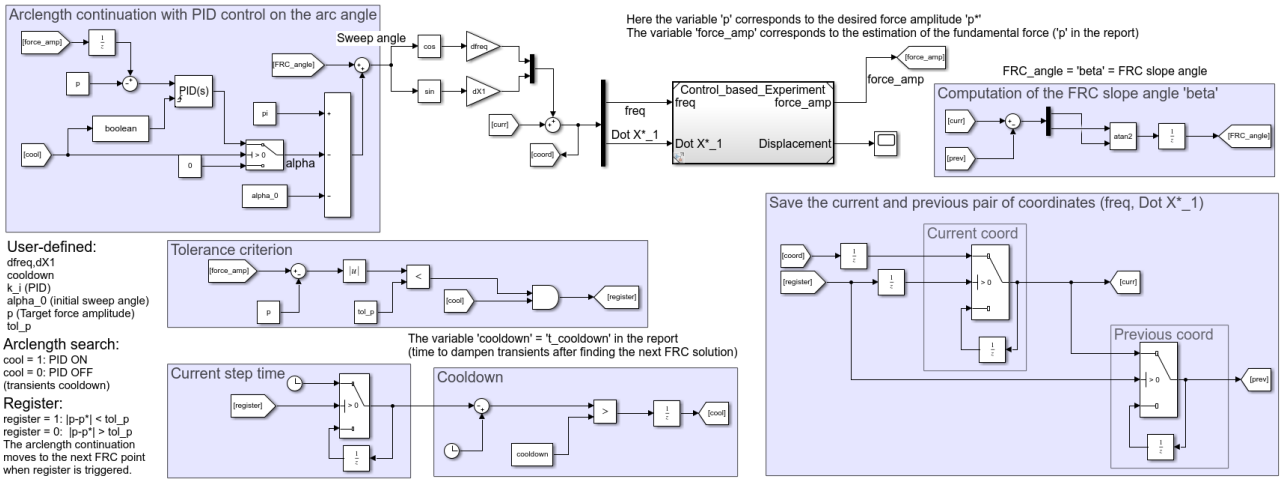

Figure A.1: Simulink diagram for the arclength continuation.

In Figure A.2, the control-based experimental model uses a derivative controller on the displacement x. It utilizes velocity signals directly, multiplying $(\dot{x}^* - \dot{x})$ by the derivative gain k_d to avoid computing derivatives. The inputs to the control-based experiment are the excitation frequency ω and the fundamental amplitude $\dot{X}^*_1$ of the reference signal $\dot{x}^*_\text{f}$. The outputs generated are the displacement x and the fundamental amplitude of the force p. Additionally, non-fundamental harmonics of the system velocity $\dot{x}_\text{nf}$ are matched to those of the reference signal $\dot{x}^*_\text{nf}$ online using adaptive filters. Although the nonlinear system used here is the Duffing oscillator, this method can be applied to any system.

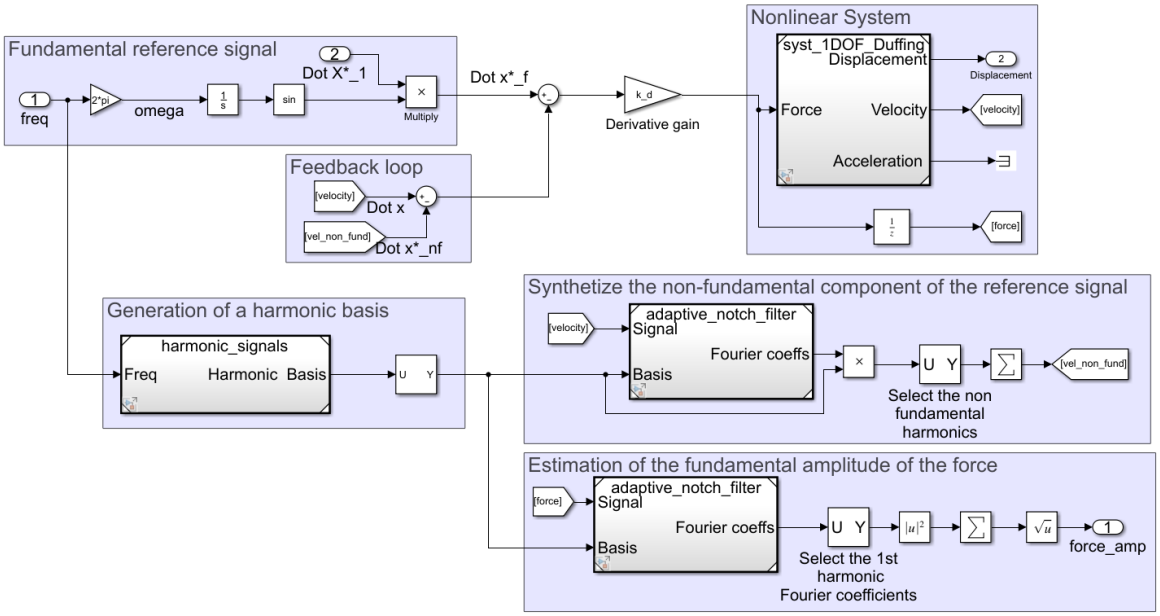

Figure A.2: Simulink diagram for the control-based experiment.

In Figure A.3, adaptive filters are used for online estimation of the Fourier coefficients [3], [79].

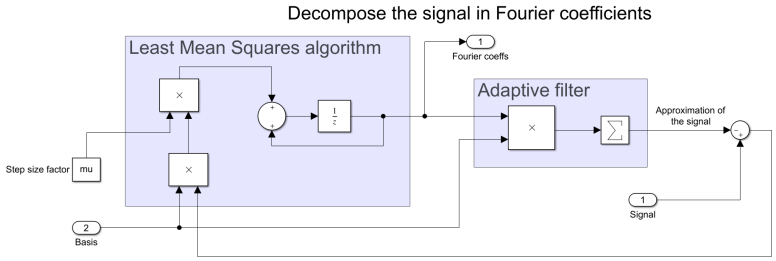

Figure A.3: Simulink diagram for the adaptive filters.

A.2. ACBC method with the double-sweep strategy

Understanding the Simulink block diagram for the double sweep is easier with Figure 6.3.

In Figures A.4 and A.5, the modified parts of the Simulink model compared to the original ACBC method are highlighted in magenta blocks. Assume that the k-th harmonic is controlled. The non-fundamental force tolerance checks if the amplitude of the k-th component of the force, $force\_amp2 = \sqrt{(s_{u,k})^2 + (c_{u,k})^2}$, is below the tolerance $\mathrm{tol}_{\mathrm{nf}}$. The non-fundamental sweep control law is $\dot{s}_{\dot{x}^*,k} = k_{i,\mathrm{nf}}\, s_{u,k}$. The controlled non-fundamental Fourier coefficient is $s\_x\_k = s_{\dot{x}^*,k}$. The corresponding Fourier coefficient of the force is $s\_u\_k = s_{u,k}$.

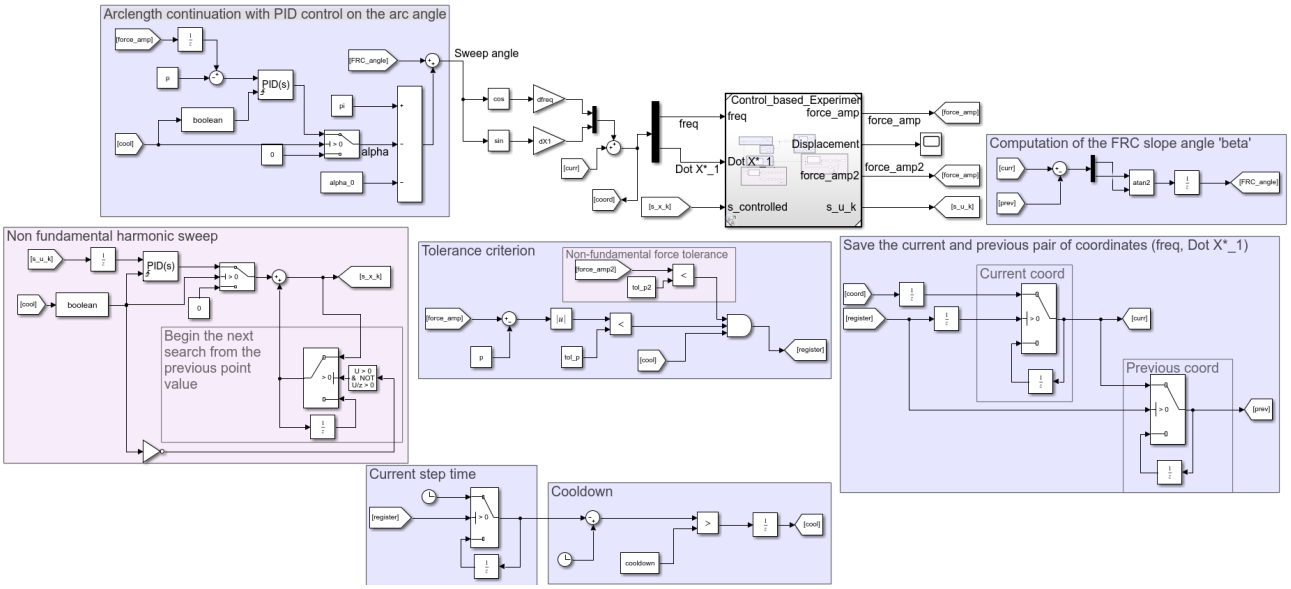

Figure A.4: Simulink diagram for the double sweep strategy.

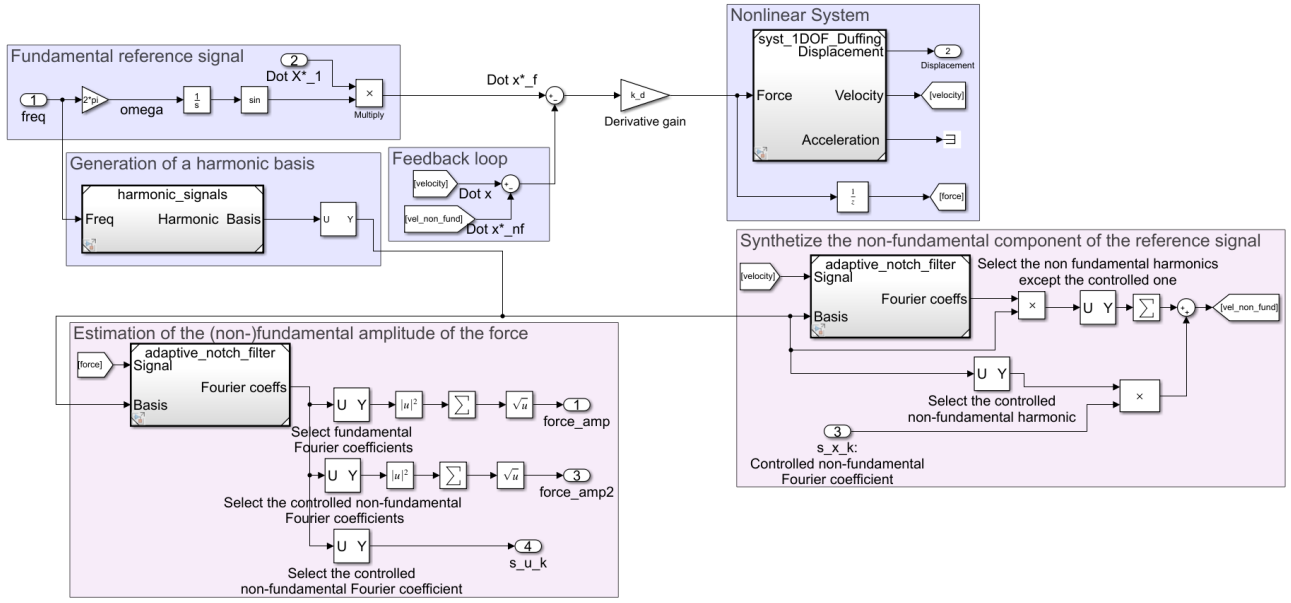

Figure A.5: Simulink diagram for the control-based experiment using the double sweep strategy.

B | Detailed results

B.1. Discrimination between intersecting FRCs solutions

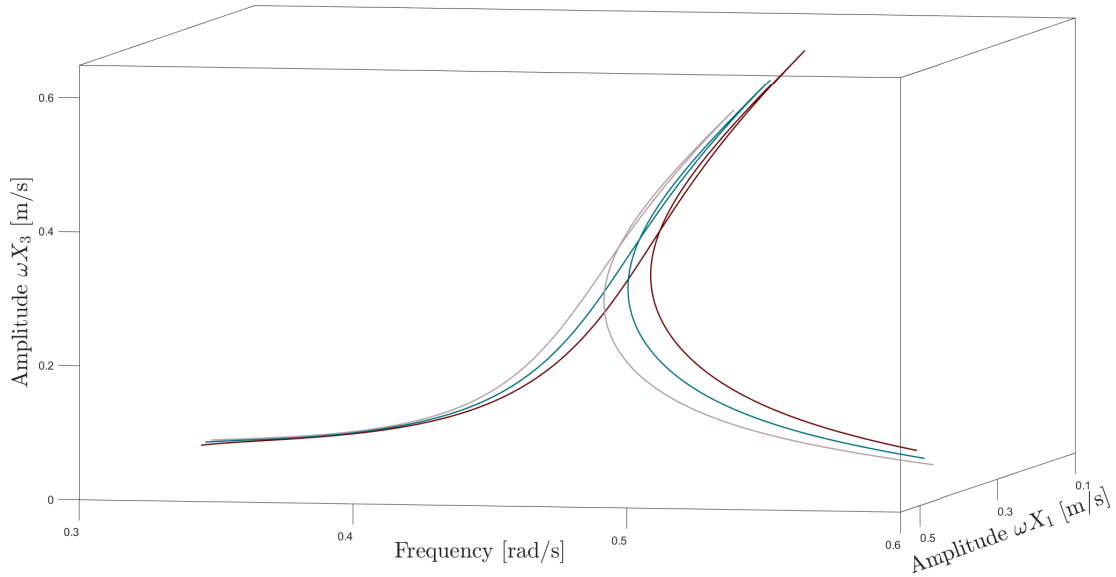

Figure B.1: The 3D plot shows that the third harmonic amplitude allows the discrimination between intersecting FRC solutions in the sweeping plane (ω, ωX_1).

B.2. Secondary resonances of the numerical Duffing oscillator

This section presents the total amplitude and harmonic contribution near the secondary resonances. These results are obtained using the ACBC method with the double-sweep strategy.

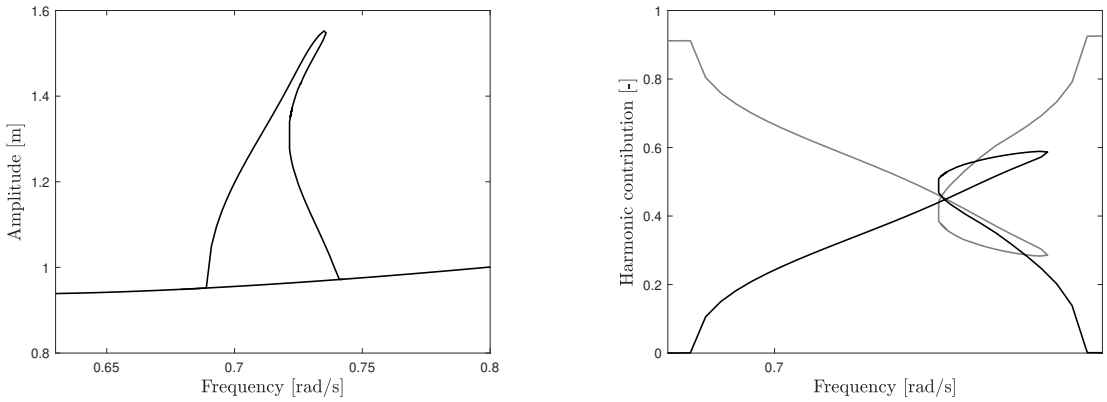

(a) (b)

Figure B.2: FRC around the $2:1$ superharmonic of the Duffing oscillator ($p = 1$ N). (a) Total amplitude. (b) Amplitude contribution of the second harmonic (black) and first harmonic (grey).

$\Delta\dot{X}_1^*$ [m/s]	$\Delta\omega$ [rad/s]	k_d [kg/s]	μ [-]	$k_{i,\mathrm{nf}}$ [-]	k_i [rad/(s N)]
0.1	0.002	0.1	$0.1\,t_s$	0.1 / -0.05	0.5

Table B.1: Double sweep strategy simulation parameters for the $2:1$ resonance of the Duffing oscillator ($p = 1$ N).

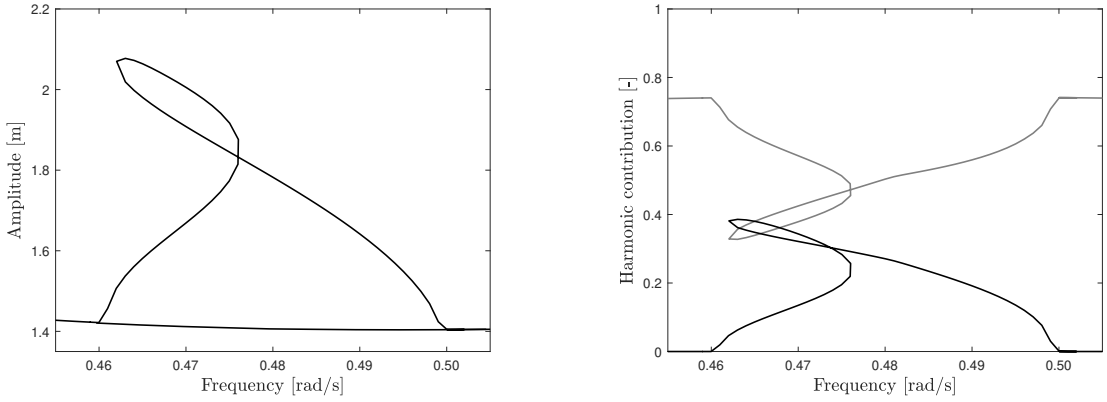

(a) (b)

Figure B.3: FRC around the $2:1$ superharmonic of the Duffing oscillator ($p = 3$ N). (a) Total amplitude. (b) Amplitude contribution of the fourth harmonic (black) and first harmonic (grey).

$\Delta\dot{X}_1^*$ [m/s]	$\Delta\omega$ [rad/s]	k_d [kg/s]	μ [-]	$k_{i,\mathrm{nf}}$ [-]	k_i [rad/(s N)]
0.1	0.001	0.25	$0.1\,t_s$	± 0.1	0.5

Table B.2: Double sweep strategy simulation parameters for the $4:1$ resonance of the Duffing oscillator ($p = 3$ N).

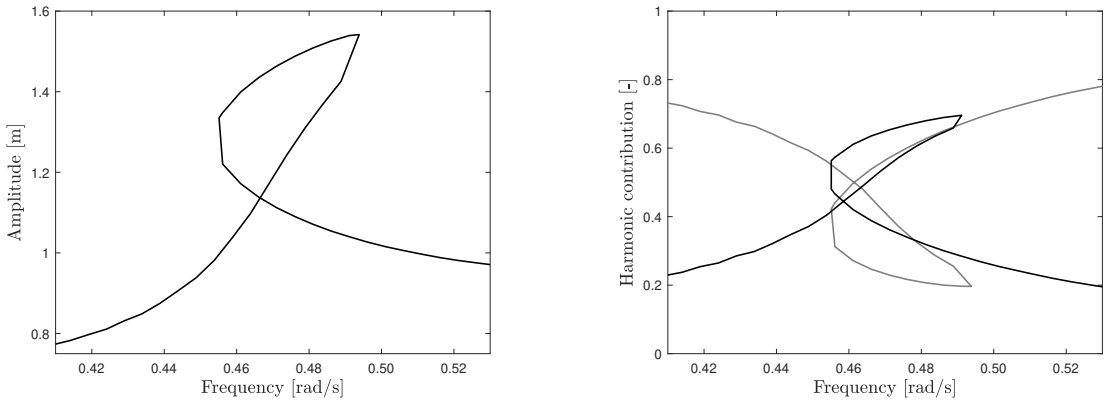

(a) (b)

Figure B.4: FRC around the $3:1$ superharmonic of the Duffing oscillator ($p = 1$ N). (a) Total amplitude. (b) Amplitude contribution of the third harmonic (black) and first harmonic (grey).

$\Delta\dot{X}_1^*$ [m/s]	$\Delta\omega$ [rad/s]	k_d [kg/s]	μ [-]	$k_{i,\mathrm{nf}}$ [-]	k_i [rad/(s N)]
0.5	0.005	0.5	$0.1t_s$	± 0.05	0.5

Table B.3: Double sweep strategy simulation parameters for the $3:1$ resonance of the Duffing oscillator ($p = 1$ N).

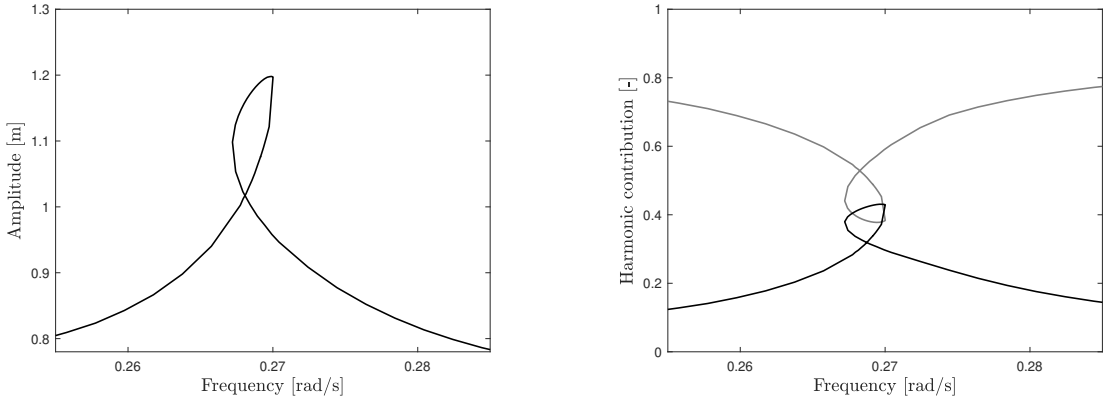

(a) (b)

Figure B.5: FRC around the $5:1$ superharmonic of the Duffing oscillator ($p = 1$ N). (a) Total amplitude. (b) Amplitude contribution of the fifth harmonic (black) and first harmonic (grey).

$\Delta\dot{X}_1^*$ [m/s]	$\Delta\omega$ [rad/s]	k_d [kg/s]	μ [-]	$k_{i,\mathrm{nf}}$ [-]	k_i [rad/(s N)]
0.02	0.001	0.5	$0.1\,t_s$	$\pm$ 0.1	0.5

Table B.4: Double sweep strategy simulation parameters for the 5 : 1 resonance of the Duffing oscillator ($p = 1$ N).

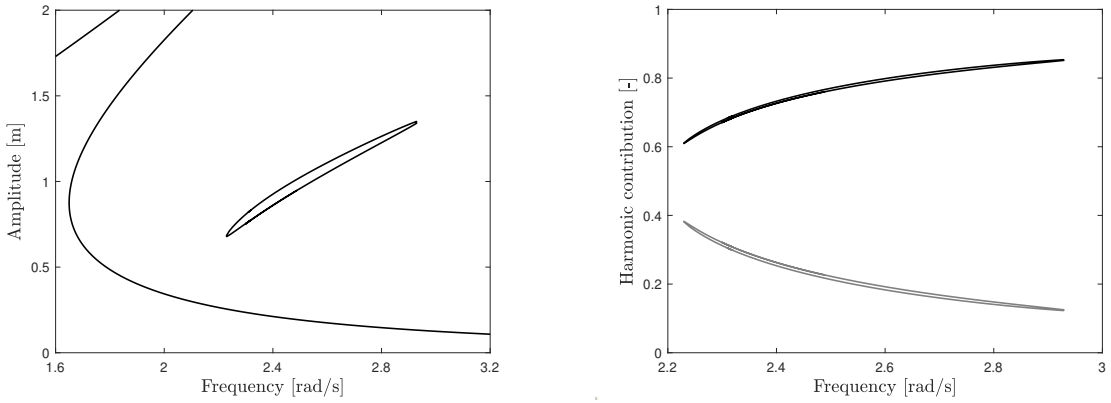

(a) (b)

Figure B.6: FRC around the 1 : 2 subharmonic of the Duffing oscillator ($p = 1$ N). (a) Total amplitude. (b) Amplitude contribution of the one-half harmonic (black) and first harmonic (grey).

$\Delta\dot{X}_1^*$ [m/s]	$\Delta\omega$ [rad/s]	k_d [kg/s]	μ [-]	$k_{i,\mathrm{nf}}$ [-]	k_i [rad/(s N)]
0.01	0.01	1	$1\,t_s$	$\pm$ 0.1	0.5

Table B.5: Double sweep strategy simulation parameters for the 1 : 2 resonance of the Duffing oscillator ($p = 1$ N).

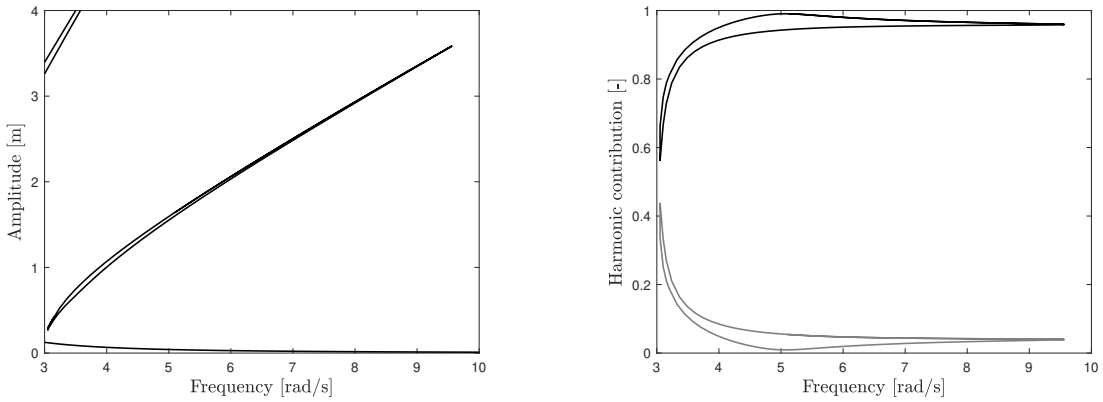

(a) (b)

Figure B.7: FRC around the $1:3$ subharmonic of the Duffing oscillator ($p = 1$ N). (a) Total amplitude. (b) Amplitude contribution of the one-third harmonic (black) and first harmonic (grey).

$\Delta\dot{X}_1^*$ [m/s]	$\Delta\omega$ [rad/s]	k_d [kg/s]	μ [-]	$k_{i,\mathrm{nf}}$ [-]	k_i [rad/(s N)]
0.1	0.125	1	$0.5\,ts$	$\pm$ 0.1	0.1

Table B.6: Double sweep strategy simulation parameters for the $1:3$ resonance of the Duffing oscillator ($p = 1$ N).

B.3. More results for the electronic Duffing oscillator

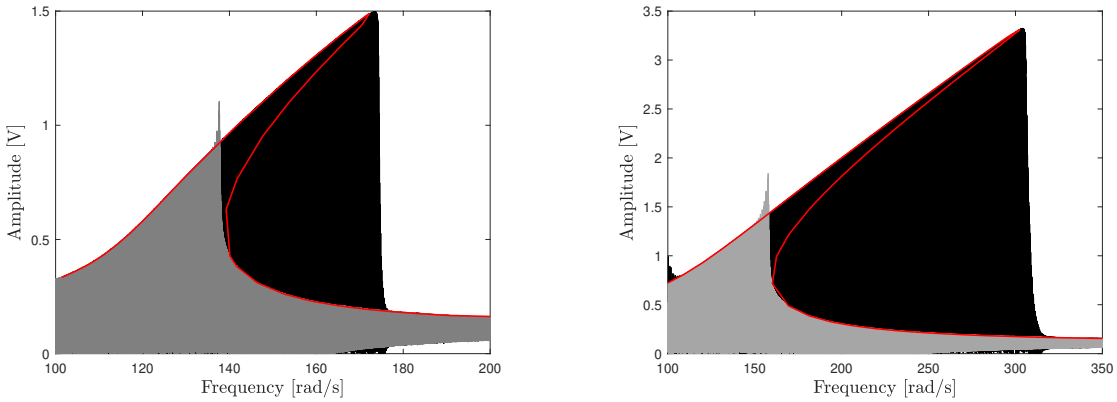

(a) (b)

Figure B.8: Comparison of results obtained with the ACBC method (red) and with sine sweep up (black) and down (grey). FRC around the fundamental resonance of the electronic Duffing oscillator at distinct forcing levels. (a) $p = 0.125$ V. (b) $p = 0.5$ V.

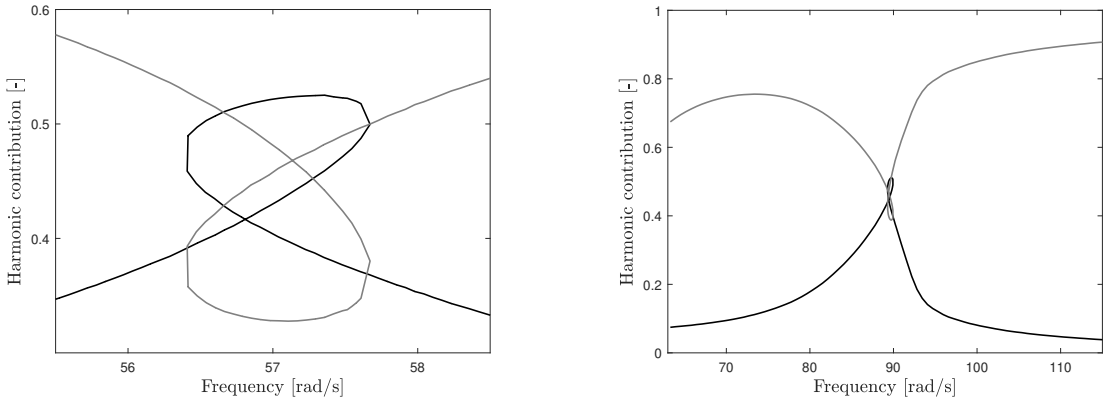

Figure B.9: Harmonic contribution around the (a) $3:1$ and (b) $2:1$ resonance of the electronic Duffing oscillator at $p = 2$ V, with the fundamental harmonic in grey and the resonant non-fundamental harmonic in black.

Bibliography

[1] G. Abeloos. *Control-based methods for the identification of nonlinear structures*. PhD thesis, University of Liège, 2022. URL https://orbi.uliege.be/handle/2268/295414.

[2] G. Abeloos and G. Kerschen. Derivative-less arclength control-based continuation for the experimental identification of nonlinear frequency responses. In *IMAC Conference*, 2023.

[3] G. Abeloos, L. Renson, C. Colette, and G. Kerschen. Stepped and swept control-based continuation using adaptive filtering. *Nonlinear Dynamics*, 104:3793–3808, 2021. URL https://doi.org/10.1007/s11071-021-06506-z.

[4] G. Abeloos, F. Müller, E. Ferhatoglu, M. Scheel, C. Collette, G. Kerschen, M. Brake, P. Tiso, L. Renson, and M. Krack. A consistency analysis of phase-locked-loop testing and control-based continuation for a geometrically nonlinear frictional system. *Mechanical Systems and Signal Processing*, 170:108820, 2022. ISSN 0888-3270. URL https://doi.org/10.1016/j.ymssp.2022.108820.

[5] M. S. Allen and R. L. Mayes. Estimating the degree of nonlinearity in transient responses with zeroed early-time fast fourier transforms. *Mechanical Systems and Signal Processing*, 24(7):2049–2064, 2010. ISSN 0888-3270. URL https://doi.org/10.1016/j.ymssp.2010.02.012. Special Issue: ISMA 2010.

[6] E. Allgower and K. Georg. Simplicial and continuation methods for approximating fixed points and solutions to systems of equations. *SIAM Journal on Numerical Analysis*, 22 (1):28–85, 1980. URL https://doi.org/10.1137/1022003.

[7] E. Allgower and P. Schmidt. An algorithm for piecewise-linear approximation of an implicitly defined manifold. *Siam Journal on Numerical Analysis*, 22:322–346, 1985. URL https://doi.org/10.1137/0722020.

[8] E. L. Allgower and K. Georg. Introduction to numerical continuation methods. *SIAM Classics in Applied Mathematics*, 45, 2003. URL https://doi.org/10.1016/j.ymssp.2017.04.011.

[9] E. L. Allgower and S. Gnutzmann. An algorithm for piecewise linear approximation of implicitly defined two-dimensional surfaces. *SIAM Journal on Numerical Analysis*, 24(2): 452–469, 1987. URL https://doi.org/10.1137/0724033.

[10] D. A. W. Barton. Control-based continuation: Bifurcation and stability analysis for phys-

ical experiments. *Mechanical Systems and Signal Processing*, 84:54–64, 2017. ISSN 0888-3270. URL https://doi.org/10.1016/j.ymssp.2015.12.039. Recent advances in nonlinear system identification.

[11] D. A. W. Barton and J. Sieber. Systematic experimental exploration of bifurcations with noninvasive control. *Phys. Rev. E*, 87:052916, 2013. URL https://doi.org/10.1103/PhysRevE.87.052916.

[12] D. A. W. Barton, B. P. Mann, and S. G. Burrow. Control-based continuation for investigating nonlinear experiments. *JVC/Journal of Vibration and Control*, 18(4):509–520, 2012. URL https://doi.org/10.1177/1077546310384004.

[13] E. Bureau, F. Schilder, I. Ferreira Santos, J. Juel Thomsen, and J. Starke. Experimental bifurcation analysis of an impact oscillator—tuning a non-invasive control scheme. *Journal of Sound and Vibration*, 332(22):5883–5897, 2013. URL https://doi.org/10.1016/j.jsv.2013.05.033.

[14] E. Bureau, F. Schilder, I. Ferreira Santos, J. Juel Thomsen, and J. Starke. Experimental bifurcation analysis of an impact oscillator—tuning a non-invasive control scheme. *Journal of Sound and Vibration*, 332(22):5883–5897, 2013. ISSN 0022-460X. URL https://doi.org/10.1016/j.jsv.2013.05.033.

[15] E. Bureau, F. Schilder, M. Elmegård, I. F. Santos, J. J. Thomsen, and J. Starke. Experimental bifurcation analysis of an impact oscillator—determining stability. *Journal of Sound and Vibration*, 333(21):5464–5474, 2014. ISSN 0022-460X. URL https://doi.org/10.1016/j.jsv.2014.05.032.

[16] H. G. Cenedese M. How do conservative backbone curves perturb into forced responses? a melnikov function analysis. *Proc. R. Soc. A 476: 20190494.*, 2020. URL http://dx.doi.org/10.1098/rspa.2019.0494.

[17] L. de Oliveira, P. Varoto, and M. Peres. Shaker structure interaction: Overview and updated results. *18th International Congress on Sound and Vibration 2011, ICSV 2011*, 3:2516–2523, 01 2011.

[18] B. J. Deaner, M. S. Allen, M. J. Starr, and D. J. Segalman. *Investigation of Modal Iwan Models for Structures with Bolted Joints*, pages 9–25. Springer New York, New York, NY, 2014.

[19] V. Denis, M. Jossic, C. Giraud-Audine, B. Chomette, A. Renault, and O. Thomas. Identification of nonlinear modes using phase-locked-loop experimental continuation and normal form. *Mechanical Systems and Signal Processing*, 106:430–452, 2018. ISSN 0888-3270. URL https://doi.org/10.1016/j.ymssp.2018.01.014.

[20] T. Detroux, L. Renson, L. Masset, and G. Kerschen. The harmonic balance method for bifurcation analysis of large-scale nonlinear mechanical systems. *Computer Methods*

in Applied Mechanics and Engineering, 296:18–38, 2015. ISSN 0045-7825. URL https://doi.org/10.1016/j.cma.2015.07.017.

[21] A. Dhooge, W. Govaerts, and K. Y. Matcont: a matlab package for numerical bifurcation analysis of odes. *ACM Trans. Math. Softw.*, 29:141–164, 2003. URL https://doi.org/10.1145/980175.980184.

[22] E. Doedel and J. Kernevez. Software for continuation problems in ordinary differential equations with applications. *Applied Mathematics, California Institute of Technology*, 1986.

[23] D. J. Ewins. *Modal Testing: Theory, Practice and Application.* Research Studies Press, Hertfordshire, U.K., 2nd edition, 2000.

[24] A. Fayezioghani, B. Vandoren, and L. Sluys. Performance-based step-length adaptation laws for path-following methods. *Computers Structures*, 223:106100, 2019. ISSN 0045-7949. URL https://doi.org/10.1016/j.compstruc.2019.07.009.

[25] B. Fraeijs de Veubeke. *Influence of internal damping on aircraft resonance.* Agard Manual of aeroelasticity. AGARD/OTAN, 1959.

[26] G. F. Franklin, J. D. Powell, and A. Emami-Naeini. *Feedback Control of Dynamic Systems.* Pearson, New York, NY, eighth edition. edition, 2020. ISBN 9781292274522.

[27] Z.-F. Fu and J. He. *Modal Analysis.* Elsevier Science, San Diego, 1st edition, 2001. URL https://doi.org/10.1016/B978-0-7506-5079-3.X5000-1.

[28] M. V. Gaëtan Abeloos and G. Kerschen. Experimental characterization of superharmonic resonances using phase-lock loop and control-based continuation. In *Nonlinear Structures & Systems*, volume 1, pages 131–133, 2022.

[29] B. Gomes, I. de Cesare, A. Guarino, M. di Bernardo, L. Renson, and L. Marucci. Exploring the dynamics of nonlinear biochemical systems using control-based continuation. *bioRxiv*, page 695866, 2019. URL https://doi.org/10.1101/695866.

[30] J. Guckenheimer and P. Holmes. *Averaging and Perturbation from a Geometric Viewpoint*, pages 166–226. Springer New York, New York, NY, 1983. ISBN 978-1-4612-1140-2. URL https://doi.org/10.1007/978-1-4612-1140-2_4.

[31] M. Géradin and D. Rixen. *Theory and Application to Structural Dynamics. 3rd.* John Wiley Sons, New York, 2015.

[32] S. Haykin. *Adaptive Filter Theory.* Prentice Hall, New Jersey, 3rd edition, 1996.

[33] M. Henderson and R. Melville. Piecewise linear continuation: Derivative-free manifold generation, 11 2023.

[34] G. W. Hill. On the part of the motion of the lunar perigee which is a function of the

mean motions of the sun and moon. *Acta Mathematica*, 8(none):1 – 36, 1900. URL 10.1007/BF02417081.

[35] P. Hippold, S. Maren, L. Renson, and M. Krack. Robust and fast backbone tracking via phase-locked loops. 2024. URL https://doi.org/10.48550/arXiv.2403.06639.

[36] D. Inmann. *Engineering Vibrations*. Pearson, 2014.

[37] H. B. Keller. *Numerical Solution of Bifurcation and Nonlinear Eigenvalue Problems*, pages 359–384. Academic Press, New York, 1977. URL https://doi.org/10.4236/jamp.2023.118146.

[38] G. Kerschen. Nonlinear vibrations of aerospace structures (aero0035-1). *Uliège*, 2023-2024. URL http://www.s3l.be/en/education.

[39] G. Kerschen, K. Worden, A. F. Vakakis, and J.-C. Golinval. Past, present and future of nonlinear system identification in structural dynamics. *Mechanical Systems and Signal Processing*, 20(3):505–592, 2006. ISSN 0888-3270. URL https://doi.org/10.1016/j.ymssp.2005.04.008.

[40] G. Kerschen, L. Soula, J. B. Vergniaud, and A. Newerla. *Assessment of Nonlinear System Identification Methods using the SmallSat Spacecraft Structure*, pages 203–219. Springer New York, New York, NY, 2011.

[41] M. Kharazan, S. Irani, M. A. Noorian, and M. R. Salimi. Nonlinear vibration analysis of a cantilever beam with multiple breathing edge cracks. *International Journal of Non-Linear Mechanics*, 136:103774, 2021. ISSN 0020-7462. URL https://doi.org/10.1016/j.ijnonlinmec.2021.103774.

[42] G. Kleyman, M. Paehr, and S. Tatzko. Application of control-based-continuation for characterization of dynamic systems with stiffness and friction nonlinearities. *Mechanics Research Communications*, 106:103520, 2020. ISSN 0093-6413. URL https://doi.org/10.1016/j.mechrescom.2020.103520.

[43] I. Kovacic and M. J. Brennan. *The Duffing Equation: Nonlinear Oscillators and Their Behaviour*. John Wiley Sons, Ltd, 2011. URL https://doi.org/10.1002/9780470977859.ch1.

[44] M. Krack and J. Gross. *Harmonic Balance for Nonlinear Vibration Problems*. Springer Cham, 2019. URL https://doi.org/10.1007/978-3-030-14023-6.

[45] B. Krauskopf, J. Galan-Vioque, and H. M. Osinga. *Numerical Continuation Methods for Dynamical Systems: Path following and boundary value problems*. Understanding Complex Systems. Canopus Publishing Limited, Dordrecht, 1. aufl. edition, 2007. ISBN 9781402063558.

[46] X. Kuang, H. Guo, J. Xu, and T. Zhou. Research on a six-phase permanent magnet

synchronous motor system at dual-redundant and fault tolerant modes in aviation application. *Chinese Journal of Aeronautics*, 30(4):1548–1560, 2017. ISSN 1000-9361. URL https://doi.org/10.1016/j.cja.2017.05.001.

[47] Y. Li and H. Dankowicz. Adaptive control designs for control-based continuation of periodic orbits in a class of uncertain linear systems. *Nonlinear Dynamics*, 103:1–17, 2021. doi: https://doi.org/10.1007/s11071-021-06216-6.

[48] R. W. L.N. Virgin, J.J. Waite. Co-existing responses in a harmonically-excited nonlinear structural system. In *Proceedings of the IMAC conference*, 2014.

[49] S. Mojrzisch, J. Wallaschek, and J. Bremer. An experimental method for the phase controlled frequency response measurement of nonlinear vibration systems. *Proceedings in Applied Mathematics and Mechanics*, 12:253–254, 2012. URL https://doi.org/10.1002/pamm.201210117.

[50] A. Nayfeh and D. Mook. *Nonlinear Oscillations*. Wiley-Intersciences, 1979.

[51] B. R. Pacini, R. L. Mayes, B. C. Owens, and R. A. Schultz. *Nonlinear Finite Element Model Updating, Part I: Experimental Techniques and Nonlinear Modal Model Parameter Extraction*, pages 263–274. Springer International Publishing, Cham, 2017.

[52] B. R. Pacini, R. J. Kuether, and D. R. Roettgen. Shaker-structure interaction modeling and analysis for nonlinear force appropriation testing. *Mechanical Systems and Signal Processing*, 162:108000, 2022. ISSN 0888-3270. URL https://doi.org/10.1016/j.ymssp.2021.108000.

[53] U. Parlitz and W. Lauterborn. Superstructure in the bifurcation set of the duffing equation x + dx + x + x3 = f cos(t). *Physics Letters A*, 107(8):351–355, 1985. ISSN 0375-9601. URL https://doi.org/10.1016/0375-9601(85)90687-5.

[54] M. Peeters, R. Viguié, G. Sérandour, G. Kerschen, and J.-C. Golinval. Nonlinear normal modes, part ii: Toward a practical computation using numerical continuation techniques. *Mechanical Systems and Signal Processing*, 23(1):195–216, 2009. ISSN 0888-3270. URL https://doi.org/10.1016/j.ymssp.2008.04.003. Special Issue: Non-linear Structural Dynamics.

[55] M. Peeters, G. Kerschen, and J. Golinval. Modal testing of nonlinear vibrating structures based on nonlinear normal modes: Experimental demonstration. *Mechanical Systems and Signal Processing*, 25(4):1227–1247, 2011. ISSN 0888-3270. URL https://doi.org/10.1016/j.ymssp.2010.11.006.

[56] S. Peter and R. I. Leine. Excitation power quantities in phase resonance testing of nonlinear systems with phase-locked-loop excitation. *Mechanical Systems and Signal Processing*, 96:139–158, 2017. ISSN 0888-3270. URL https://doi.org/10.1016/j.ymssp.2017.04.011.

[57] S. Peter and R. I. Leine. Excitation power quantities in phase resonance testing of nonlinear

systems with phase-locked-loop excitation. *Mechanical Systems and Signal Processing*, 96: 139–158, 2017. ISSN 0888-3270. URL https://doi.org/10.1016/j.ymssp.2017.04.011.

[58] S. Peter, F. Schreyer, P. Reuss, and L. Gaul. Consideration of local stiffening and clearance nonlinearities in coupled systems using a generalized harmonic balance method. *Proceedings of ISMA 2014 - International Conference on Noise and Vibration Engineering and USD 2014 - International Conference on Uncertainty in Structural Dynamics*, pages 3097–3110, 2014.

[59] R. Pintelon and J. Schoukens. *System Identification: A Frequency Domain Approach.* John Wiley Sons, 2nd edition, 2012.

[60] G. Raze. An electronic Duffing oscillator, 2024. URL https://github.com/GhislainRaze/Electronic-Duffing.

[61] L. Renson, A. Gonzalez-Buelga, D. Barton, and S. Neild. Robust identification of backbone curves using control-based continuation. *Journal of Sound and Vibration*, 367:145–158, 2016. ISSN 0022-460X. URL https://doi.org/10.1016/j.jsv.2015.12.035.

[62] L. Renson, D. A. W. Barton, and S. A. Neild. Experimental tracking of limit-point bifurcations and backbone curves using control-based continuation. *International Journal of Bifurcation and Chaos*, 27(01):1730002, 2017. URL https://doi.org/10.1142/S0218127417300026.

[63] L. Renson, A. Shaw, D. Barton, and S. Neild. Application of control-based continuation to a nonlinear structure with harmonically coupled modes. *Mechanical Systems and Signal Processing*, 120:449–464, 2019. ISSN 0888-3270. URL https://doi.org/10.1016/j.ymssp.2018.10.008.

[64] L. Renson, J. Sieber, D. Barton, A. Shaw, and S. Neild. Numerical continuation in nonlinear experiments using local gaussian process regression. *Nonlinear Dynamics*, 98:2811–2826, 2019. URL https://doi.org/10.1007/s11071-019-05118-y.

[65] D. R. Roettgen and M. S. Allen. Nonlinear characterization of a bolted, industrial structure using a modal framework. *Mechanical Systems and Signal Processing*, 84:152–170, 2017. ISSN 0888-3270. URL https://doi.org/10.1016/j.ymssp.2015.11.010. Recent advances in nonlinear system identification.

[66] M. Scheel, T. Weigele, and M. Krack. Challenging an experimental nonlinear modal analysis method with a new strongly friction-damped structure. *Journal of Sound and Vibration*, 485:115580, 2020. ISSN 0022-460X. URL https://doi.org/10.1016/j.jsv.2020.115580.

[67] R. Seydel. *A Continuation Algorithm with Step Control*, pages 480–494. Birkhäuser, Basel, 1984. URL https://doi.org/10.1007/978-3-0348-6256-1_33.

[68] R. Seydel. *Practical Bifurcation and Stability Analysis*, volume 5 of *Interdisciplinary*

Applied Mathematics. Springer Nature, New York, NY, 3rd ed. edition, 2009. ISBN 1441917403.

[69] L.-L. Show, J.-C. Juang, C.-T. Lin, and Y.-W. Jan. Spacecraft robust attitude tracking design: Pid control approach. In *Proceedings of the 2002 American Control Conference (IEEE Cat. No.CH37301)*, volume 2, pages 1360–1365 vol.2, 2002. URL https://doi.org/10.1109/ACC.2002.1023210.

[70] J. Sieber and B. Krauskopf. Control-based continuation of periodic orbits with a time-delayed difference scheme. *International Journal of Bifurcation and Chaos*, 17(08):2579–2593, 2007. URL https://doi.org/10.1142/S0218127407018646.

[71] J. Sieber, B. Krauskopf, D. Wagg, S. Neild, and A. Gonzalez-Buelga. Control-Based Continuation of Unstable Periodic Orbits. *Journal of Computational and Nonlinear Dynamics*, 6(1), 2010. URL https://doi.org/10.1115/1.4002101.

[72] I. J. Sokolov and V. I. Babitsky. Phase control of self-sustained vibration. *Journal of Sound and Vibration*, 248:725–744, 2001. URL https://doi.org/10.1006/jsvi.2001.3810.

[73] J. Stoker. Nonlinear vibrations in mechanical and electrical systems. *Interscience Publishers*, 1995.

[74] G. Tomlinson. Force distortion in resonance testing of structures with electro-dynamic vibration exciters. *Journal of Sound and Vibration*, 63(3):337–350, 1979. ISSN 0022-460X. URL https://doi.org/10.1016/0022-460X(79)90678-3.

[75] P. Varoto and L. de Oliveira. On the interaction between the vibration exciter and the structure under test in vibration testing. In *International Modal Analysis Conference - IMAC*. SEM, 2001.

[76] M. Volvert. *Resonant phase lags of nonlinear mechanical systems.* PhD thesis, University of Liège, 2024. URL https://orbi.uliege.be/handle/2268/311417.

[77] M. Volvert and G. Kerschen. Phase resonance nonlinear modes of mechanical systems. *Journal of Sound and Vibration*, 511:116355, 2021. ISSN 0022-460X. URL http://dx.doi.org/10.1016/j.jsv.2021.116355.

[78] G. Von Groll and D. Ewins. The harmonic balance method with arc-length continuation in rotor/stator contact problems. *Journal of Sound and Vibration*, 241(2):223–233, 2001. URL https://doi.org/10.1006/jsvi.2000.3298.

[79] B. Widrow, C. S. Williams, J. R. Glover, J. M. McCool, R. H. Hearn, J. R. Zeidler, J. Kaunitz, E. Dong, and R. C. Goodlin. Adaptive noise cancelling: Principles and applications. *Proceedings of the IEEE*, 63:1692–1716, 1975.

[80] L. Woiwode and M. Krack. Experimentally uncovering isolas via backbone tracking. *Jour-*

nal of Structural Dynamics, 2024. URL https://api.semanticscholar.org/CorpusID:267450947.

[81] J. Yoon and B. Kim. Stability and bifurcation analysis of super- and sub-harmonic responses in a torsional system with piecewise-type nonlinearities. *Scientific Reports*, 11: 2045–2322, 2021. URL https://doi.org/10.1038/s41598-021-03088-z.

[82] Z. Zhang, J. Liu, N. Zhang, X. Cao, Y. Yuan, M. Sultan, and S. Attia. Dynamic discharging performance of a latent heat thermal energy storage system based on a pid controller. *Journal of Energy Storage*, 71:107911, 2023. ISSN 2352-152X. URL https://doi.org/10.1016/j.est.2023.107911.

[83] T. Zhou and G. Kerschen. Identification of secondary resonances of nonlinear systems using phase-locked loop testing. *Journal of Sound and Vibration*, 2024. URL https://doi.org/10.48550/arXiv.2401.01151.

[84] Y. Zhou, J. Wu, H. Li, and Y. Li. Analysis of nonlinear characteristics for forced oscillation affected by quadratic nonlinearity. *IEEE Transactions on Power Systems*, 37(1):804–807, 2022. URL 10.1109/TPWRS.2021.3120589.

[85] K. J. Åström, P. Albertos, and J. Quevedo. Pid control. *Control engineering practice*, 9 (11):1159–1161, 2001. ISSN 0967-0661.